Improvements in Electron Cryo-Tomography Towards Understanding Virus Surfing



Vojtěch Pražák

Wolfson College

University of Oxford

A thesis submitted for the degree of

DOCTOR OF PHILOSOPHY

Under the supervision of Prof. Kay Grünewald

Trinity 2019

Acknowledgements

One of the main breakthroughs I made in the course of my DPhil was the realisation that science, for better or worse, is not the knowledge uncovered through research, but the people that work towards it. Through serendipity I chose the research group of Kay Grunewald who supported my pursuit of more or less random ideas, for which I thank him. In addition, I had the help and support of many incredibly kind and knowledgeable people, but would like to thank primarily Susan Black, Lindsay Baker, Christiane Riedel, Daven Vasishtan, Benjamin Vollmer and Rainer Kaufmann for their help and stimulating discussions.

A part of this thesis, for which I am a primary author, was published in a peer-reviewed journal together with contributions of my colleagues:

Moser, F.*, Prazak, V.*, V. Mordhorst, D. M. Andrade, L. A. Baker, C. Hagen, K. Grunewald and R. Kaufmann (2019). "Cryo-SOFI enabling low-dose super-resolution correlative light and electron cryo-microscopy." Proc Natl Acad Sci U S A 116(11): 4804-4809

* Authors contributed equally

“It fits so much better without the map.”

– Overheard during a discussion about electron microscopy density fitting.

Improvements in Electron Cryo-Tomography
Towards Understanding Virus Surfing

Vojtěch Pražák

Wolfson College, University of Oxford

Doctor of Philosophy, Trinity 2019

Abstract

Electron cryo-tomography (cET), in combination with sub-volume averaging (SVA), is a powerful technique for determining the structure of complex biological specimens that are not amenable to more traditional structure determination methods. In Chapter 1, SVA was used to achieve a sub-nanometre resolution structure of Herpes simplex virus 1 glycoprotein B in its pre-fusion conformation. Nevertheless, several challenges still undermine the routine use of cET for structural cell biology. Imaging with an electron beam damages specimens, leading to localised warping of tomograms and reduced resolution of SVA maps if not compensated for. Using densities of biological structures within tomograms as fiducial markers is one solution to this problem. A software implementation of this concept, termed 'Flexo' and its application is demonstrated in Chapter 2. While this improves tomogram quality, other issues persist. The lack of a specific labelling technique for cET often limits the use of SVA to large and recognisable structures; correlation with super-resolution cryo-fluorescence microscopy (cryo-FM) is a promising solution. The primary drawback of this technique has been devitrification induced by the high laser intensities typically required. Chapter 3 describes Cryo-SOFI as a general solution to this problem, enabling substantial resolution improvement in cryo-FM, and allowing cET to be performed in a correlative fashion. Chapter 4, explores

the avenues of combining live-cell FM imaging with cET to study the transport of virus particles along cellular protrusions, called virus surfing. Events of surfing and static viruses can look alike in cET snapshots, making it necessary to link these high-resolution observations with their dynamic history. This led to the development of techniques towards live-CLEM: correlative live-cell light and electron microscopy, which also revealed that cells undergo major structural changes during the preparation for cryogenic preservation. Overall, the work presented in this thesis presents a number of promising solutions to overcome some major obstacles for cET to fulfil its full potential for *in situ* structural cell biology.

Contents

List of Abbreviations 1
0 Introduction 4
0.1 Structural biology of complex systems 4
0.2 Cryo-EM 5
0.3 Tomography captures specimens as 3D volumes. Almost. 6
0.4 Sub-volume averaging, a quickly evolving technique 8
0.5 On integration and correlation 12
0.6 Overall goals 13
Chapter 1 Determining the molecular structure of HSV-1 glycoprotein B 14
1.1 Introduction 14
Membrane fusion 14
Viral membrane fusion 14
HSV-1 fusion machinery 15
Post-fusion gB structure 16
Sub-volume averaging of gB: A collaborative endeavour 20
1.2 Results 21
1.3 Discussion 25
Initial map validation 26
The transmembrane vacuum 27
The N-terminus remains unclear 28
The fusion loop downfall 29
Mechanism of H516P pre-fusion stabilisation 30
Future directions 35
1.4 Materials and methods 36
Specimen preparation 36
Electron Microscopy Data Acquisition 36
Data Processing and tomogram reconstruction 37
Sub-volume averaging 38
Chapter 2 Fixing tomograms with Flexo 45
2.1 Introduction 45
EM imaging is extremely damaging to the specimen 45
Local and global distortions attenuate high-resolution information 46
Compensating for specimen damage is difficult in 3D 46

Flexo: a simple implementation of an existing concept 48
2.2 Results and discussion 50
Description of Flexo architecture and workflow 50
Tomogram reference 52
Alignment is performed in 2D 53
Application to specific examples 54
Future development 61
2.3 Materials and methods 63
Data acquisition 63
Software packages and libraries 64
Chapter 3 Cryo-SOFI: A general solution to cryogenic super-resolution imaging 66
3.1 Introduction 66
Fluorescence imaging 66
Bridging the resolution gap 68
Light microscopy at cryogenic temperatures: technical challenges 69
Fluorescence at cryogenic temperatures 70
Low-intensity super-resolution imaging 71
Cryo-SOFI, a collaborative effort 72
3.2 Results 73
3.3 Discussion 79
High-resolution comes at the cost of vitrification 79
Cryo-SOFI, a general solution to cryogenic super-resolution FM 80
Hardware improvements are needed for routine cryo-CLEM 82
3.4 Materials and methods 85
Cell Culture 85
Specimen preparation 85
Electron Microscopy Data Acquisition and data processing 86
Cryo-SOFI setup, data acquisition and processing 87
Chapter 4 How (not) to Catch a Surfing Virus 90
4.1 Introduction 90
Virus surfing precedes entry 90
Uptake of non-viral particles 93
Actin retrograde flow 94
Studying dynamic virus-host interactions by cET 95
4.2 Results and discussion 98
Overview of experimental systems 98

MLV surfing on XCmCAT cells 99
MLV-YFPenv does not bind to a large proportion of XC cells 103
Adenovirus surfing precedes endocytosis 105
Virus binding events observed by cET are structurally heterogeneous 107
Live-CLEM, because history matters 110
Designing live-CLEM hardware 111
Physical and chemical properties of support film change cell behaviour 116
From ECM proteins to covalent functionalisation 117
Blotting causes extensive structural changes of cellular specimens 120
Implications of blotting-induced damage on EM of cellular specimens 122
Plunge-freezing results in areas of local vitrification 122
Future directions 124
4.3 Materials and methods 125
Generation of XC cell lines stably expressing fluorescent mCAT-1 or CAR 125
Preparation of MLV virus stocks 126
Virus surfing experiments 127
Specimen preparation for optimisation of cell adhesion 127
Specimen preparation for EM 128
5 Discussion 130
References 140
Appendix I 155

List of Abbreviations

ARF	actin retrograde flow
BV	Benjamin Vollmer
CAR	Coxsackie adenovirus receptor
CCD	Charged coupled device
cET	electron cryo-tomography or electron cryo-tomograms
CLEM	correlative light and electron microscopy
CR	Christiane Riedel
Cryo-CLEM	Cryogenic correlative light and electron microscopy
Cryo-EM	Cryogenic electron microscopy
Cryo-FM	Cryogenic fluorescence microscopy (imaging)
Cryo-LM	Cryogenic light microscopy
Cryo-SOFI	cryogenic super-resolution optical fluctuation imaging
CTF	contrast transfer function
DV	Daven Vasishtan
ECM	extracellular matrix
EM	electron microscopy, used exclusively for transmission electron microscopy
EMDB	electron microscopy database
Env	Envelope glycoprotein
FIB	focussed ion beam
FM	fluorescence microscopy (imaging)
FSC	Fourier-shell correlation

gB	HSV-1 glycoprotein B
Grids	interchangeable with EM grids
HSV-1	herpes simplex virus 1
HW	Harald Woodrich
Live-CLEM	live correlative light and electron microscopy
LM	Light microscopy
mCAT-1	mouse cationic amino acid transporter 1, the receptor for MLV Env
MD	molecular dynamics simulation
MLV	murine leukemia virus
NA	numerical aperture
PH	Plekstrin homology
PSF	point spread function
RT	room temperature
SIM	Structured illumination microscopy
SMLM	single molecule localisation microscopy
SNR	signal to noise ratio
SOFI	super-resolution optical fluctuation imaging
STED	stimulated emission depletion microscopy
SU	Surface
SVA	sub-volume averaging
TEM	transmission electron microscopy
TM	Transmembrane
VP	Vojtěch Pražák

VSV	vesicular stomatitis virus
WM	Walther Mothes
WT	Wild-type
YFP	Yellow fluorescent protein

0 Introduction

0.1 Structural biology of complex systems

The structure and function of individual biological macromolecules underlie the complex systems to which they belong, from molecular assemblies to cells and whole organisms. Structural biology is the study of how structure relates to function; the main focus is usually the causal relationship between the atomic structure and chemical function. A famous example is the discovery of the DNA double-helical structure in 1953, which was critical for the understanding of DNA replication and genetic inheritance (Watson and Crick, 1953). However, as the natural philosopher P. W. Anderson said (Anderson, 1972):

> "The ability to reduce everything to simple fundamental laws does not imply the ability to start from those laws and reconstruct the universe. The constructionist hypothesis breaks down when confronted with the twin difficulties of scale and complexity. At each level of complexity entirely new properties appear. Psychology is not applied biology, nor is biology applied chemistry. We can now see that the whole becomes not merely more, but very different from the sum of its parts."

The approach to the work in this thesis is to use both holistic and reductionist structural biology to understand complex biological systems. The primary technique used throughout is transmission electron microscopy (TEM or just EM) due to its potential to image specimens at a wide range of resolutions and scales of complexity. EM has been long used to study complex biological specimens, such as the organisation of cells within tissues or the architecture of organelles within cells. Biological structures, in what is referred to as "classical EM", are observed indirectly after chemical fixation and heavy metal staining, which distorts their structure. Sectioning is almost invariably required

as transmission electron micrographs are projections of the whole specimen density and electrons interact strongly with matter, which means that only thin specimens (below ~ 500 nm) can be imaged.

0.2 Cryo-EM

More recent developments, in particular cryogenic fixation, have enabled direct observation of biological complexes in their native environment, giving rise to cryo-EM (Dubochet and McDowall, 1981, Dubochet and Lepault, 1984). Cryogenic fixation arrests molecules in a "frozen-hydrated" state by rapid cooling, which prevents ice crystal formation that would otherwise disrupt their structure and interactions with other molecules. The main limitation of cryo-EM is that biological molecules are extremely susceptible to radiation damage caused by the electron beam. As a result, there is a limit to the number of electrons (electron fluence) that can be used to image any one molecule before it is destroyed. This limits the signal to noise ratio (SNR) of raw cryo-EM micrographs. Reconstruction methods in structural biology circumvent this limitation by computationally averaging data from many thousands of identical structures, after determining their relative orientations, to increase the SNR and allow high-resolution details to be resolved (Frank *et al.*, 1981). Using this approach, single particle cryo-EM now routinely achieves high-resolution 3D maps from projection images of biochemically pure proteins or symmetrical virus particles suspended in a thin film of vitrified buffer: More than 3000 EM maps with resolution higher than 4 Å have been deposited in the EMDB since 2014 (EMDB Statistics, 2019, October 7). However,

biological molecules rarely act in isolation and there remains a need to study molecules with high-resolution in the context of their native environment.

0.3 Tomography captures specimens as 3D volumes. Almost.

Unperturbed biological systems, such as the cytoplasm of whole cells, are exceedingly crowded environments. Micrographs of even the thinnest cellular protrusions are projections of many overlapping proteins, which means that averaging is challenging. Electron cryo-tomography (cET) can be used in order to reconstruct a 3D volume of the specimen. This is achieved by physically tilting the specimen and acquiring micrographs (tilts) at many angular increments. Fiducial markers (objects of known shape visible in all tilts, typically gold nanoparticles) can then be used to align tilts relative to each other, allowing them to be back-projected into a tomogram. The slab-like geometry of the vast majority of specimens causes their apparent thickness to increase with $1/cos$ of the tilt angle. This limits the maximum tilt angle at which tilts can be acquired resulting in a "missing wedge" of information and the corresponding anisotropic resolution of electron tomograms. As a consequence of radiation susceptibility common to all biological specimens, together with the lack of a reliable labelling techniques, only very large biological structures such as ribosomes or large protein can be discerned. Nevertheless, cET has been successfully used for structure determination inside unperturbed vitrified cells (Ortiz *et al.*, 2010, Bykov *et al.*, 2017), since individual particles (sub-volumes) extracted from tomograms can be averaged by sub-volume averaging (SVA) in a similar manner to projection images (Figure 0.1).

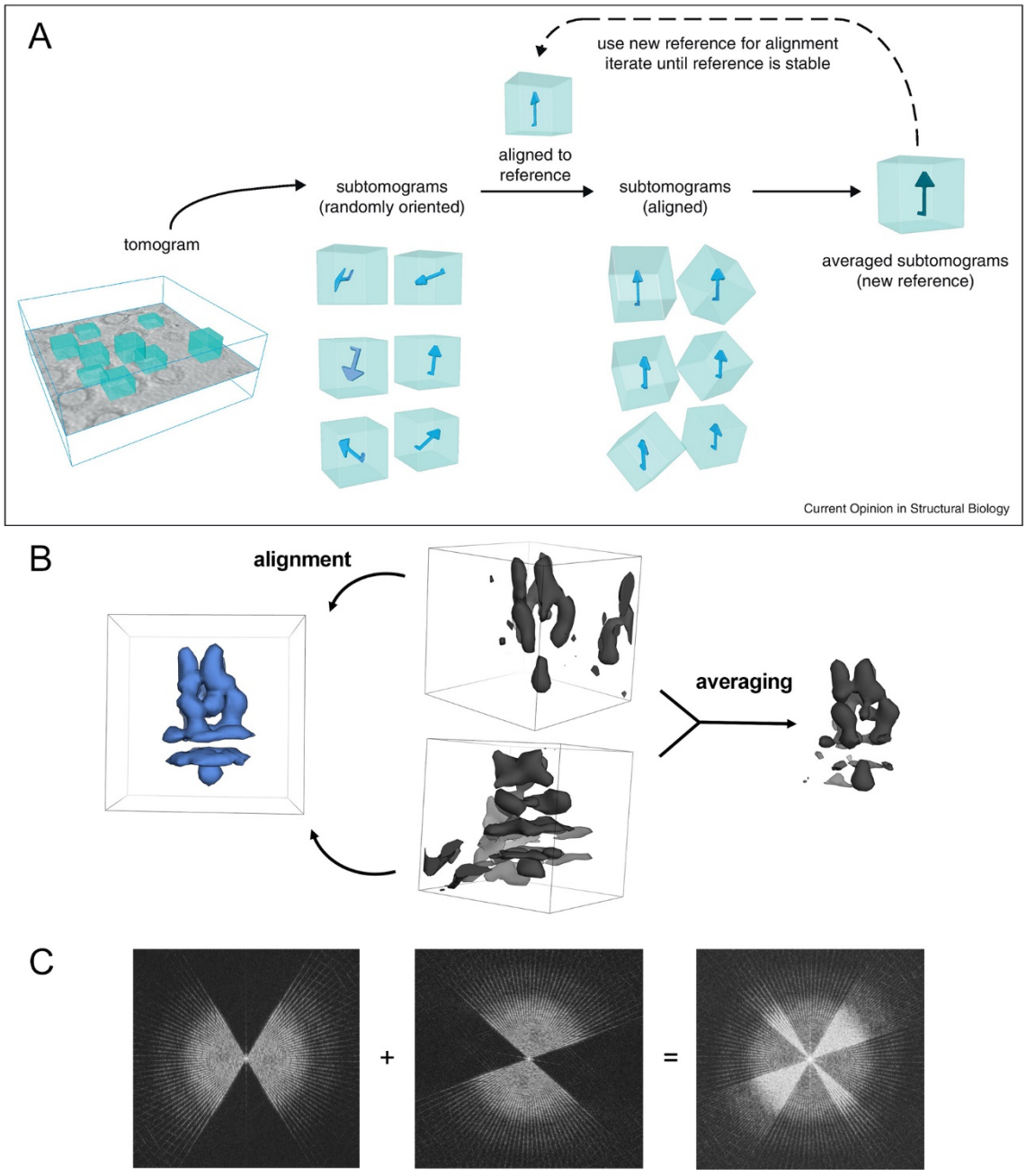


Figure 0.1 Sub-volume Alignment. (**A**) Structures within a tomographic volume are computationally extracted within smaller volume subsets (commonly referred to as sub-volumes or sub-tomograms) and aligned to a reference volume. Aligned sub-volumes are averaged together and used as a new reference for subsequent iterations of alignment. Reproduced with permission from Briggs (2013). Individual particle sub-volumes are distorted due to the missing wedge of information, depicted as real space volumes (**B**) or sections of tomogram power spectra oriented along the tilt axis (**C**). Averaging of particles with different orientation (left and middle boxes) fills in the missing information in Fourier-space leading to reduction of real-space artefacts.

0.4 Sub-volume averaging, a quickly evolving technique

The basic principle of SVA is to extract sub-volumes (often referred to as particles) from a tomographic volume and average them with different sub-volumes of the same molecular species. The resultant average volume has a higher signal-to-noise ratio (SNR) which makes it possible to resolve high-resolution structural features. This can be explained with a set of two equations. First, an image or a 3D volume can be thought of as a combination of signal and Gaussian noise:

$$m = s + n, \qquad (1)$$

where *m*, *s* and *n* are the values of image, signal and noise in Fourier-space (Heymann, 2019). The reduction of the noise component can be expressed as equation (2):

$$\sigma^{(N)^2} = \sigma^2 + \frac{1}{N}\sigma_n^2, \qquad (2)$$

where $\sigma^{(N)^2}$, σ^2 , σ_n^2 is the variance of the average image, signal and noise, here expressed for 2D images (Frank *et al.*, 1981).

In practice, it is necessary to first identify and then align individual sub-volumes of the same structural species. Inaccuracies in alignment or structural differences result in blurring and loss of SNR. The low SNR of electron cryo-tomograms (cET) is the main limitation for high-resolution determination, but the poor separation of densities caused by the missing wedge is an additional complication for feature alignment. As a result, very few high-resolution SVA structures have been published thus far. Notable examples such as that of human immunodeficiency virus 1 capsid or coat protein complex II (Schur *et al.*, 2016, Hutchings *et al.*, 2018) are an indication that SVA is capable of reaching high-resolution, and that a high degree of order and symmetry is

likely the most important determinant of achievable resolution. Nevertheless, there has been a steady overall trend towards higher resolution that highlights advances in EM hardware and data processing. The introduction of "direct electron detectors" allowed collection of micrographs with higher SNR due to a boost in their detective quantum efficiencies. A higher level of electron microscope automation has also increased the number of tilt series that could be reliably acquired.

On the software side, the main focus has been on correcting for the contrast transfer function (CTF correction). The CTF is the Fourier-space equivalent of point spread function, which models how information is transferred by the microscope to the data and can be approximated by equation (3),

$$r_{obs}{}^2(g) = r^2(S)CTF^2(g)Env^2(S) + n^2(g), \qquad (3)$$

where $r^2(S)$ is the radially averaged Fourier intensity, $Env^2(S)$ an overall envelope factor (the decay of high-resolution frequencies) and $n^2(S)$ the noise component (Glaeser, 2007). The dependency of CTF on the optical parameters and the specimen is modelled by equations (4), (5) and (6),

$$CTF(\lambda, g, \Delta f, C_s) = -w_1 sin\chi(\lambda, g, \Delta f, C_s) - w_2 cos\chi(\lambda, g, \Delta f, C_s) \qquad (4)$$

$$\chi(\lambda, g, \Delta f, C_s) = \pi\lambda\, g^2\Delta f - \frac{1}{2}\lambda^2 g^2 C_s, \qquad (5)$$

where λ is the electron wavelength, g the spatial frequency, Δf the defocus and C_s the microscope spherical aberration (Figure 0.2, A). w_1 and w_2 denote the relative contributions of phase and amplitude contrast A (Mindell and Grigorieff, 2003):

$$w_1 = \sqrt{1 - A^2} \qquad (6)$$

$$w_2 = A \qquad (7)$$

The effect of CTF on electron micrographs can be observed directly as concentric rings (Thon rings) in the image power spectra; this is used for defocus estimation (Figure 0.2, B). The majority of contrast in cryo-EM is generated by imaging at under-focused conditions. Defocus causes the CTF to oscillate between positive and negative values, meaning that some features have negative contrast. Moreover, all contrast is lost at spatial frequencies where CTF = 0. The oscillation between positive and negative contrast are commonly corrected by phase-flipping:

$$f_p(g) = sign\big(CTF(S)\big)f(g), \qquad (8)$$

where f is the Fourier transform of an image (Penczek, 2010). This requires accurate determination of image defocus. This is further complicated in tomographic data: Tilting induces a defocus gradient and the apparent thickness of specimens increases with tilt angle ($1/\cos\alpha$); this dampens high-frequency Thon rings which are required for accurate defocus fitting. Typical cET specimens are between 100 – 300 nm thick which means that the Z-axis position (the "depth") of particles dispersed throughout introduces a significant error in CTF correction (Figure 0.2, C) (Turonova *et al.*, 2017).

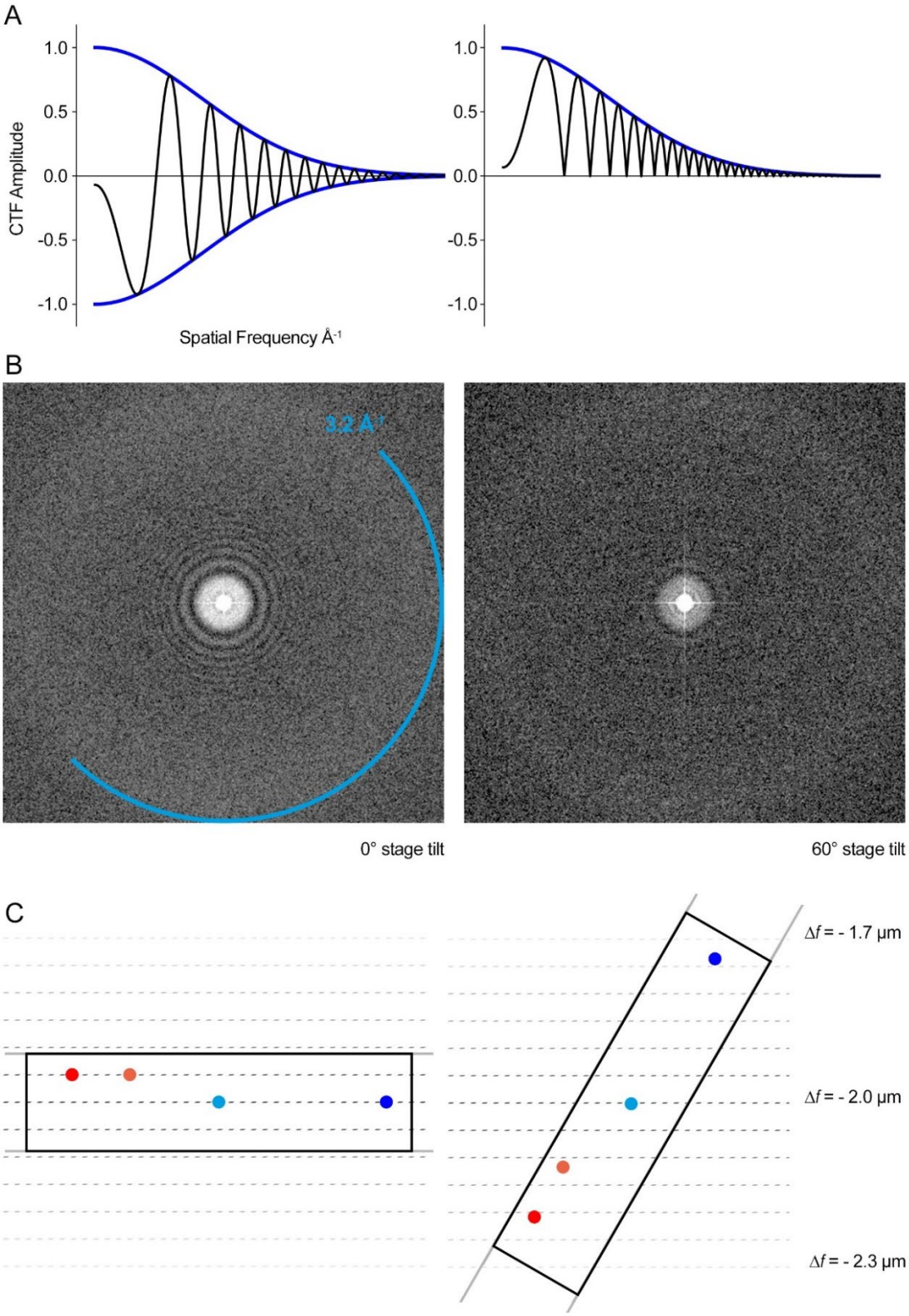


Figure 0.2 Contrast Transfer in Electron Tomography. (**A**, left) CTF (black line) plotted in 1D according to equations (4) to (7). (**A**, right) Phase-flipping inverts negative contrast in micrographs. This is essential in order to recover structural information beyond the first CTF zero crossing. The exponential decay of high-frequency intensities (blue line) is commonly referred to as experimental B-factor can be modelled as Gaussian function with width B, $\exp(-Bg^2)$. Applying a negative B-factor can be used to compensate for the relatively low intensities at high frequencies which is known as map sharpening. (**B**) "Typical" power spectra of micrographs acquired at 0° and 60° stage tilt. (**C**) Individual particles within a specimen can have significantly different defocus depending on their Z-axis position and the angle of stage tilt.

0.5 On integration and correlation

Structural biology methods generally have a niche application but benefit strongly from integration with others. While the resolution of 3D maps obtained through SVA is generally limited to resolutions worse than 1 nm, they can be fitted with pseudo-atomic models generated by other structural techniques, typically X-ray crystallography. X-ray crystallography generates atomic models. When several of these are fitted into a low-resolution EM map the composite model can be described as a pseudoatomic model. The integration of high-resolution X-ray data and the native molecular context of SVA can reveal valuable information about the formation of higher-order structures of molecular complexes or protein conformational states that only exist in complex environments. This has been particularly useful to probe, among others, membrane fusion proteins of enveloped viruses. These proteins are embedded in the membranous virus envelope and mediate its fusion with the target cell membrane. This process is essential to establish an infection. Determining the structure of membrane fusion proteins by X-ray crystallography typically requires removal of their transmembrane domain and the information about their higher-order arrangement is lost in the process. Sub-nanometre SVA maps of intact fusion proteins on whole virions have been fitted with X-ray crystal structures in order to better understand the steps necessary for membrane fusion to occur and how it can be prevented (Förster *et al.*, 2005, Zanetti *et al.*, 2006, Li *et al.*, 2016).

In the opposite direction of the resolution scale is correlative light and (cryo) electron microscopy (CLEM). It combines the specific labelling potential of fluorescence microscopy (FM) with the high resolving power of EM. This approach has been used for

direct acquisition of rare biological events such as adenovirus particles escaping from endosomes and to investigate the higher order structure of focal adhesions (Patla *et al.*, 2010, Schellenberger *et al.*, 2014).

0.6 Overall goals

One of the main goals of the work presented in this thesis was to work with and improve current methods related to cET in order to study the structure and dynamic behaviour of virus particles interacting with host cells. Specifically, to observe virus particles as they are transported along the cell membrane in a process called virus surfing. EM captures a snapshot of biological specimens in time, regardless of whether they were preserved by chemical or cryogenic fixation. A single snapshot in time does not allow the discrimination of virus particles engaged in surfing from those that are static. While it is easy to obtain dynamic information in FM, there is currently no way of relating this to specimens observed in EM. This is primarily due to the relatively long process required for specimen preparation and practical handling before it can be vitrified. A substantial reduction in the length of preparation would make it possible to link individual virus particles with their dynamics observed previously in FM and therefore to distinguish different types of binding. This would be followed up by SVA in order to gain insight into the underlying molecular components. A multitude of methods were explored on the path towards these goals and it became clear that improvements in methodology could be one of the ways of achieving them. The extent of the author's involvement in developing, and attempts at improving cET (and related) methodology is presented in this thesis.

Chapter 1 Determining the molecular structure of HSV-1 glycoprotein B

1.1 Introduction

Membrane fusion

Membrane fusion is a fundamental process in biology that can occur between cells, intracellular organelles and during viral entry. Despite the variety in underlying purpose, the mechanism by which proximal membranes are fused is believed to follow a common fusion-through-hemifusion pathway. Briefly, a hemifusion stalk is generated by the mixing of the outer leaflets of the bilayers in two proximal membranes. This transient state can dissociate or proceed to the formation of fusion pores (Figure 1.1) (Chernomordik and Kozlov, 2008).

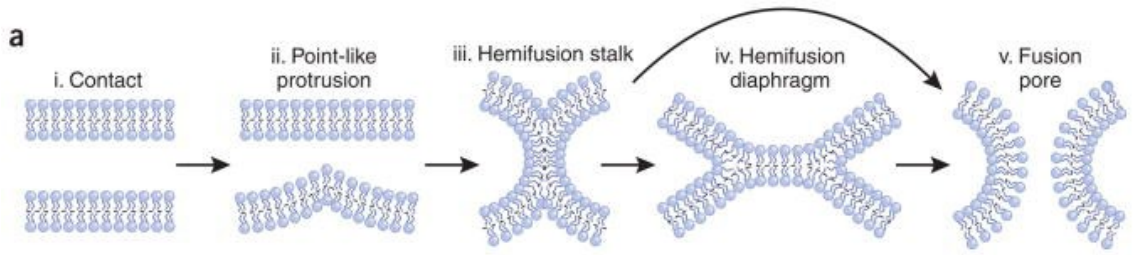


Figure 1.1 Fusion of membrane bilayers proceeds through a hemifusion intermediate. Adapted with permission from Chernomordik and Kozlov (2008).

Viral membrane fusion

To establish an infection, enveloped viruses must first fuse their membrane with either the plasma or endocytic vesicle membrane of the host to gain entry into the cytoplasm.

This is achieved by the action of viral fusion proteins that catalyse membrane fusion through a series of conformational changes: In general, a short hydrophobic motif commonly referred to as fusion loop is inserted into the host cell membrane followed by a conformational change that induces membrane curvature. This brings the two membranes into proximity which allows hemifusion and ultimately fusion to occur. Existing viral fusion proteins are segregated in to three structural classes (Harrison, 2008). Class I fusion proteins typified by human immunodeficiency virus envelope glycoprotein (Env) or influenza hemagglutinin, class II fusion proteins such as the Rift Valley fever virus gN/gC and class III fusion proteins such vesicular stomatitis virus (VSV) glycoprotein G or herpes simplex virus 1 (HSV-1) glycoprotein B (gB). This study focuses on gB, the class III fusogen of HSV-1.

HSV-1 fusion machinery

Many enveloped viruses achieve receptor binding and membrane fusion using a single multifunctional viral envelope glycoprotein. In contrast, the envelope of herpesviruses contains a large number of different surface glycoproteins. It is believed that four are required for HSV entry into the host cell: glycoproteins B (gB), H (gH) and L (gL) and a less conserved glycoprotein D (gD) (Connolly *et al.*, 2011).

While gB can interact with heparan sulfate of cell surface proteoglycans, this interaction alone is insufficient for triggering fusion (Laquerre *et al.*, 1998). Specific virus-host interaction is mediated by gD binding to herpes virus entry mediator (HVEM) and nectin-1 (Krummenacher *et al.*, 2004). The role of the gH/gL is less well defined as conflicting reports about their ability to mediate hemifusion exist (Duus *et al.*, 1995,

Suenaga *et al.*, 2010). The structure of the gH/gL ectodomain determined by X-ray crystallography revealed that the heterodimer shares no structural homology with any known fusion protein. It is, therefore, assumed that they act in a regulatory capacity through their interactions with gB, despite no evidence of direct binding (Chowdary *et al.*, 2010, Matsuura *et al.*, 2010). Once triggered, membrane fusion is carried out by gB; however, the nature of its activation is not known. The post-fusion conformation of gB from HSV-1 (Heldwein *et al.*, 2006), Epstein-Barr virus (Backovic *et al.*, 2009), pseudorabies virus (Vallbracht *et al.*, 2018) and human cytomegalovirus (Burke and Heldwein, 2015, Chandramouli *et al.*, 2015) have been determined by X-ray crystallography. These structures typically contain only the protein ectodomain with the notable exception of a full-length post-fusion crystal structure of HSV-1 gB (Cooper *et al.*, 2018), which includes the transmembrane and C-terminal domains. These structures indicate a high degree of structural homology exists between the post-fusion conformations across the herpesvirus family.

Post-fusion gB structure

Viral membrane fusion proteins undergo remarkable conformational rearrangements to promote fusion of the viral and host membranes. Therefore, at a minimum, these proteins exist in a pre-fusion state in the viral membrane, an intermediate state to initiate host membrane binding, and a post-fusion state. Post-fusion HSV-1 gB is a trimer of 904 amino acid protomers; approximately 700 N-terminal residues form a 16 nm long ectodomain which is connected to a short C-terminal intraluminal domain via a single transmembrane helix (Figure 1.2, A). The ternary structure of gB can be separated into

five domains, which facilitates description of this highly intertwined structure. Domains I and II have a fold similar to classical pleckstrin homology (PH) domains, domain I contains the fusion loops (around positions 177 and 269) which are embedded in the membrane in the post-fusion conformation. Domain III consists of a long alpha-helical coiled coil and it forms the main trimer interaction interface. Domain IV, positioned at the membrane-distal "top" of the protein, has no structural homology to other known domains and domain V is a long extended linker leading to a membrane-proximal amphipathic helix and the transmembrane domain. The protein N-termini contain a classical signal sequence for type I transmembrane proteins that is cleaved in virions; the remaining residues 31-111 are predicted to be disordered and are not resolved in any crystal structure (Figure 1.3, A).

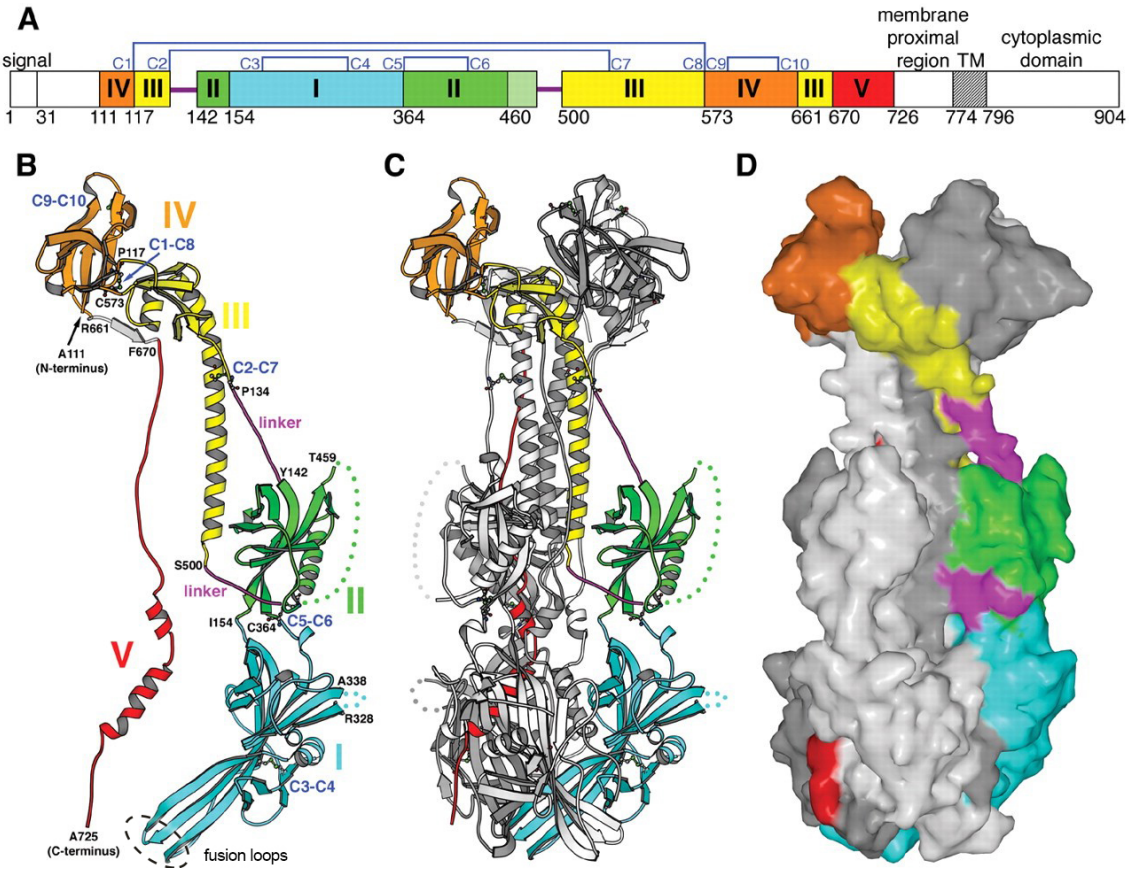


Figure 1.2 Domain architecture of post-fusion conformation of HSV-1 gB. (**A**) Regions of the primary structure contributing to individual domains are highlighted in cyan (domain I), green (II), yellow (III), orange (IV) and red (V). There are a large number of stabilising disulphide bonds in this protein, which

are indicated by lines connecting cysteine residues numbered in order (C1-C10). Ribbon representations of a gB ectodomain protomer (**B**) and trimer (**C**). Approximate position of fusion loops is indicated with a dashed line. Linkers not resolved in 2GUM are indicated with dotted lines. (**D**) Surface representation showing the relative positions of gB domains. Modified with permission from Heldwein *et al.* (2006).

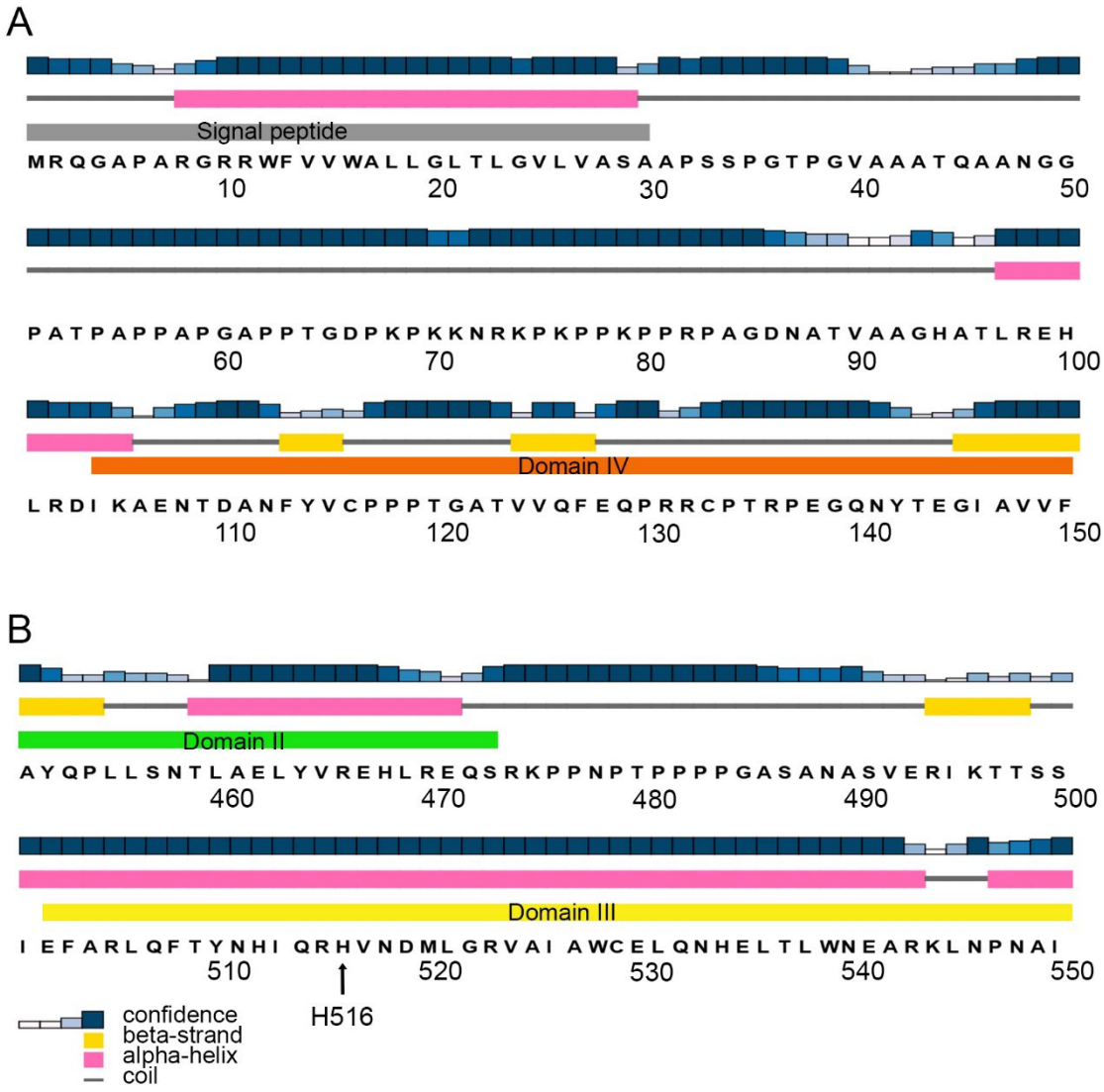


Figure 1.3 Secondary structure prediction of gB N-terminus and domain II-III interface. (**A**) The protein N-terminus consists of a signal peptide that is cleaved in the mature virion and a disordered region consisting primarily of small, hydrophobic and basic residues. (**B**) The linker between domains II and III is a proline-rich domain predicted to be involved in transient protein-protein interaction. Secondary structure prediction was performed using PSIPRED (Jones *et al.*, 1999, Buchan and Jones, 2019)

In all cases, the production and crystallisation of HSV-1 gB resulted in the post-fusion conformation. Two distinct conformational states could be observed in electron cryo-tomograms of native membrane vesicles produced by over-expression of wild type gB (Figure 1.4): A long form corresponding to the post-fusion structure and a shorter

more condensed conformation (Zeev-Ben-Mordehai *et al.*, 2016). The authors used SVA to determine 3D maps of these conformations; the 3D reconstruction of the short form was resolved to 23 Å and the long form to 31 Å. The long form likely corresponds to the post-fusion conformation as the SVA map was visibly similar to, and was fitted with, a crystal structure of the gB ectodomain. The SVA map for the short-form was fitted with crystal structures of domains I and II using a hierarchical rigid domain fitting approach in an attempt to model the pre-fusion conformation of gB. This indicated that the fusion loops of domain I are located on the membrane-distal tips of the protein. However, an unambiguous fit could not be obtained due to the limited resolution of the SVA data.

In an attempt to gain a clearer picture of the domain architecture of the pre-fusion gB, effort was directed at methods for stabilisation of the full-length protein in the pre-fusion conformation. Expression of gB with a single point mutation (H516P) resulted in native membrane vesicles with a substantially reduced population of the long form (less than 1%, Benjamin Vollmer, manuscript in preparation). A similar approach to that used by Zeev-Ben-Mordenhai *et al*., (2016), was utilised for the gB H516P protein in order to gain better insight into the pre-fusion conformation and thus the membrane fusion mechanism of this protein. This chapter describes the SVA averaging of this mutant that lead to a revised model of the pre-fusion conformation.

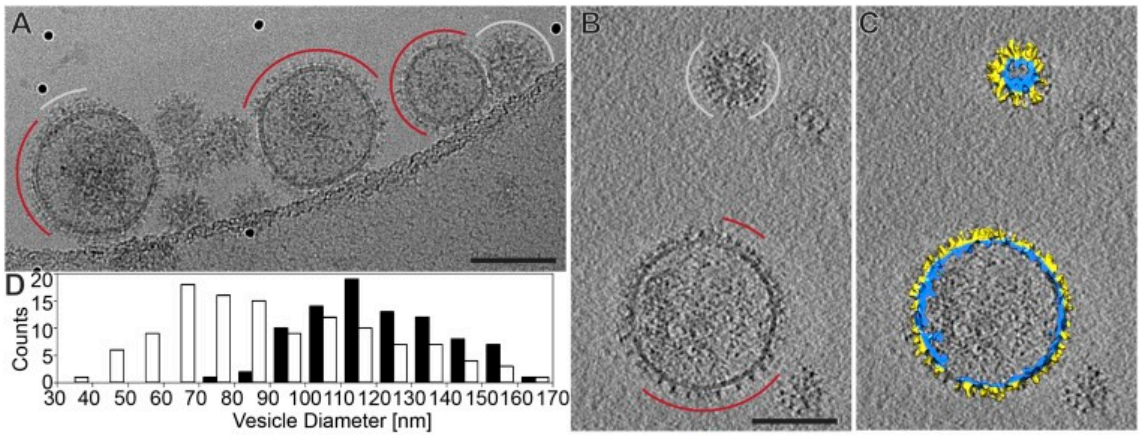


Figure 1.4 Two conformational states of HSV-1 gB observed by cET. (**A**) A projection image, (**B**) a tomogram slice indicating the presence of long (white line) and short (red line) forms of gB. (**C**) Tomogram section shown in (**B**) was segmented to indicate the membrane (blue) and protein (yellow) contribution to observed density. (**D**) The long form (white bars) was observed primarily on smaller vesicles (higher curvature), whereas the short form (black bars) for was more frequently observed on larger vesicles. Reproduced with permission from Zeev-Ben-Mordehai *et al*., (2016).

Sub-volume averaging of gB: A collaborative endeavour

The data presented in this chapter are a result of a long-term effort of a number of members of the Grünewald lab to understand the fusion machinery of HSV-1 with the main focus on gB. Tzvia Zeev-Ben-Mordehai established an efficient method to produce gB vesicles embedded in native plasma membrane vesicles, which was further optimised by Benjamin Vollmer (BV). Stabilisation of the short form (putative pre-fusion conformation) of gB by a single point mutation (H516P) was a result of an extensive structural characterisation effort by BV, who also prepared all specimens used in this study. Daven Vasishtan (DV) wrote and maintained a number of custom computational scripts that were essential for all structures presented. The author of this thesis (VP) wrote scripts based on DV code. BV and VP acquired and reconstructed tomographic data. BV, DV and VP picked particles; DV and VP were primarily involved in fitting of molecular models with helpful discussion from Kay Grünewald, Maya Topf and BV.

1.2 Results

To determine optimal acquisition parameters for high-resolution structure determination, tilt series of HSV1 gB H516P vesicles were collected with a number of different parameters (Table 1). The main controlled variable was the total electron fluence (often referred to as electron dose) and the corresponding electron fluence per tilt. Increasing the electron fluence should boost low resolution information of tomograms which, in turn, should improve SVA alignment at the cost of more pronounced specimen warping. Surprisingly, tomograms with higher total dose did not have substantially more pronounced warping artefacts. On the contrary, the general trend was that tomograms with a higher total dose were clearer and it was possible to identify and pick particles with more confidence. There was substantial variability in the thickness of specimens used for data collection ranging from ~ 31 nm to ~ 200 nm. Vesicles in thinner specimens were noticeably flattened, which often resulted in gB spikes being concentrated towards their sides. Several vesicles contained filamentous actin which was used to confirm the hand of SVA maps.

Two independent SVA maps were initially generated from tomograms grouped by total electron dose. The higher dose tomograms were collected on Titan Krios and are referred to as "Krios data" for simplicity; the lower dose "Polara data" was collected on Tecnai F30 "Polara". Both data sets resulted in ~ 13 Å resolution maps and the decision was made to combine these data for the purpose of increasing resolution. The combined data yielded an 11 Å resolution map. Further improvement in resolution was achieved by manually removing particles with incorrect geometry, i.e. particles that did not have their Y-axes (3-fold symmetry axes) oriented orthogonal or oriented

perpendicular to the vesicle tangential plane, or particles that were too far from the membrane bilayer. This increased the map resolution to 9 Å which was sufficient for rigid body fitting of individual domains of the post-fusion conformation gB crystal structure (Figures 1.5 – 1.7). An initial assumption was made that gB domain IV would remain in the same ternary complex observed in the post-fusion structure. This enabled the molecular model of domain IV to be fitted into the pre-fusion map with a high degree of confidence (Figure 1.6, A). The orientation of domain IV indicated that the domain III coiled coil would point away from the membrane. There were three central tubular densities above domain IV, but these could not be fitted with the domain III coiled coil as an intact unit (Figure 1.7, B). Domain III was instead split into individual alpha-helices, which were fitted into the central tubular densities. Domains II and III are separated by a ~ 3 nm long linker (9 amino acids, C133-T142) which imposed a connectivity constraint on the possible localisation of domain II, and in turn domain I. It was not possible to fit domains I and II oriented with fusion loops pointing up (assuming domain II remained intact), as this would require a minimum linker length of at least 5 nm. Domains I and II were therefore fitted with fusion loops pointing towards the membrane, which put the linker end residues 133 and 142 in close proximity. Assigning domains I-IV populated the majority of the SVA map, except for the very membrane-distal top of the map and membrane proximal densities, which were suggested to contain parts of the N-terminus and domain IV residues, respectively (Fig 1.7, C). A tentative flexible fit was assigned to domain V, which might be used for and refined by targeted mutagenesis experiments. Finally, this molecular model was refined in a molecular dynamic (MD) simulation with the SVA map as a restraint in order to relax bonds stretched during reorganisation of the post-fusion structure.

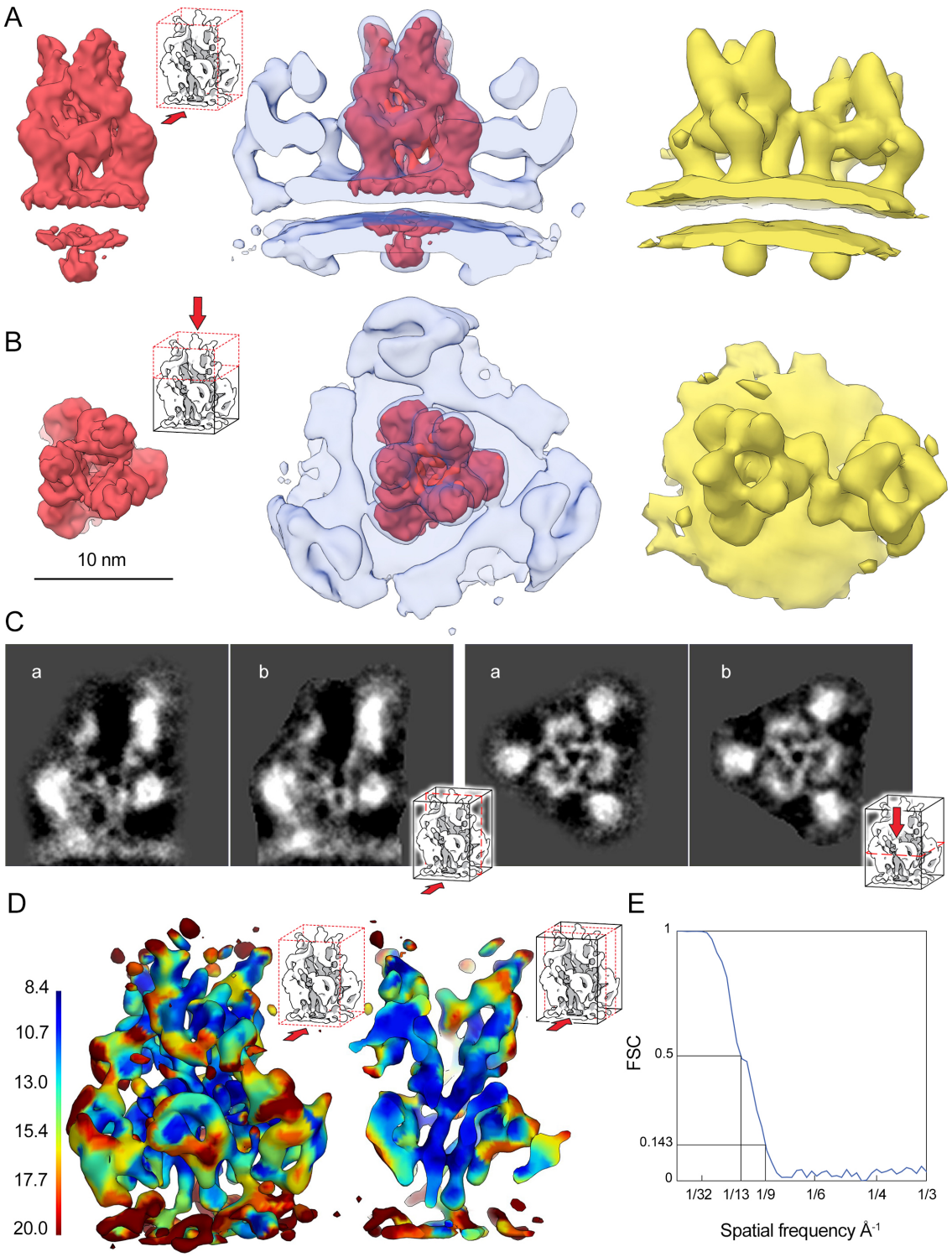


Figure 1.5 SVA maps of the gB short form. To the left are side (**A**) and top (**B**) views of a gB SVA in the short form. Middle shows the same map surface rendered at lower contours to indicate the contribution of densities from neighbouring gB trimers. To the right is an average of the trimer-trimer interaction at an undetermined resolution (visually similar to single gB SVA map at 10-20 Å). This average was obtained by applying a mask around the central and one neighbouring timer, and allowing a 270° rotation search around the central particle Y axis. (**C**) Slices through SVA half-maps used for resolution estimation. (**D**) Local resolution map generated by MonoRes (Vilas *et al.*, 2018) (**E**) Fourier-shell correlation between half-maps shown in (**C**).

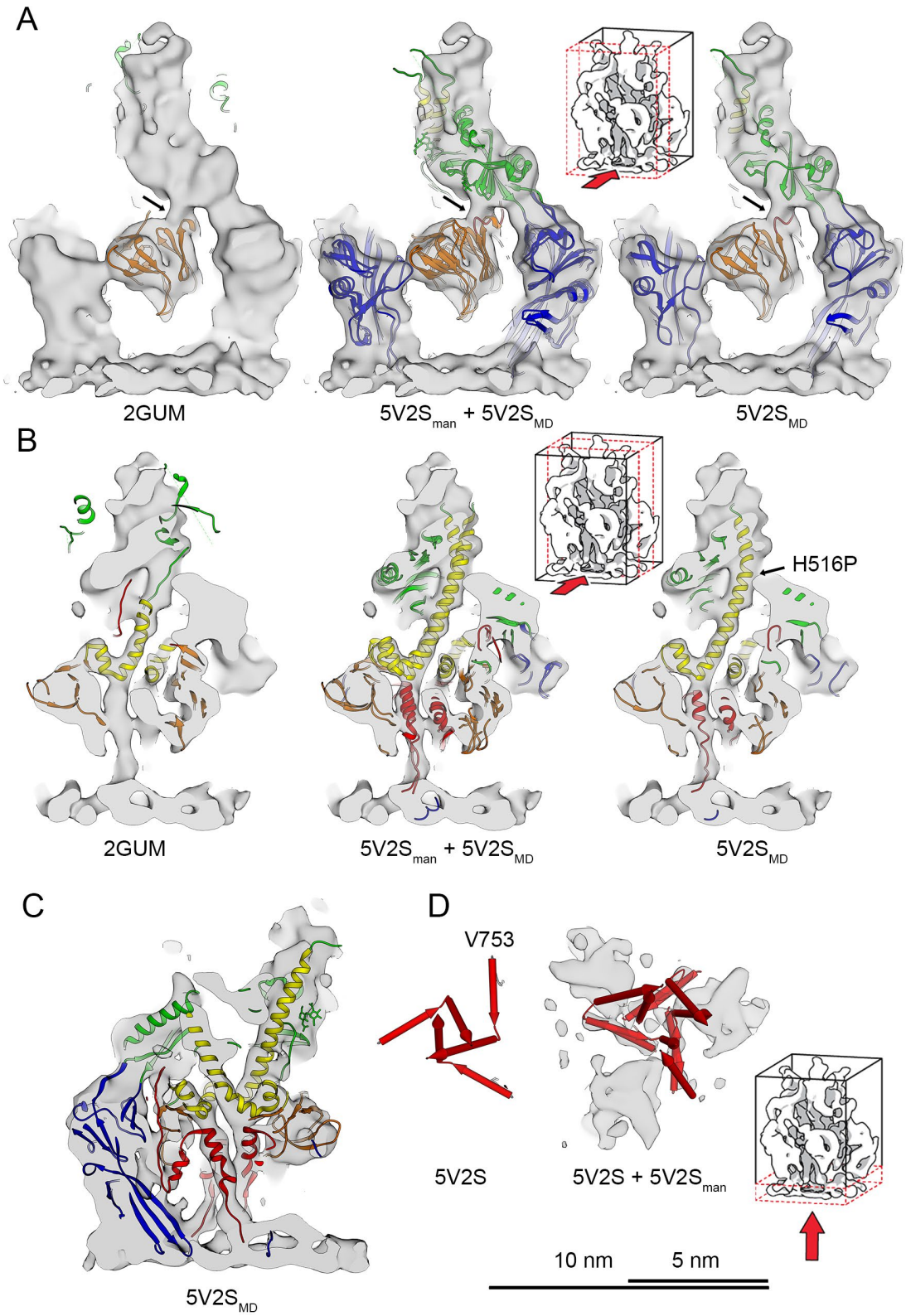


Figure 1.6 Agreement of pre-fusion gB model and map. (**A**), (**B**) SVA map of the ectodomain fitted with 2GUM (Heldwein *et al.*, 2006) (left), pre-fusion model before (middle) and after MD (right). (**C**) A slice through the map indicating a tentative assignment of domain IV. (**D**) Comparison between the domain IV membrane proximal and transmembrane helices in 5V2S (Cooper *et al.*, 2018) (left) and their possible location in in the pre-fusion map. Due to the absence of transmembrane densities the membrane proximal helices were fitted in two opposing orientations. A bridging density between volumes assigned to domain IV and II is highlighted with a black arrow in (**A**). Please refer to figure 1.7 and section 1.3 Discussion for details.

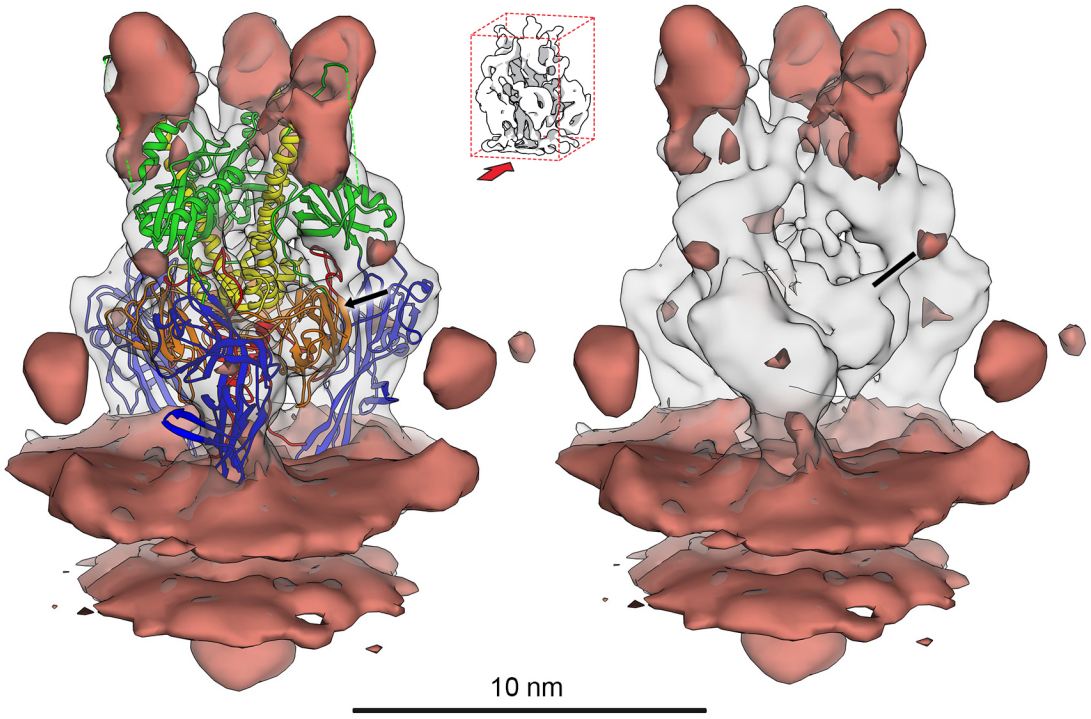


Figure 1.7 Difference map between experimental SVA map and simulated density of the pre-fusion model. A pseudoatomic model of the pre-fusion conformation of gB was generated and subtracted from the experimental map in Chimera. The resulting volume difference (salmon) contains primarily densities corresponding to the membrane bilayer, neighbouring gB trimers and the poorly resolved membrane-distal tips. The original SVA map is shown in grey. Black arrow indicates position of residue 106 of the N-terminal domain (colour coded as domain IV, orange) where ~ 1.5 nm long helix is predicted to form based on the primary structure of gB. MD resulted in folding of residues 103-109 along the outside of domain IV. The predicted helix could feasibly occupy a bridging density between domains IV and II, which was highlighted with a 1.5 nm bar on the right side model.

1.3 Discussion

Presented above is a SVA map of HSV-1 gB in a putative pre-fusion conformation determined in conditions approaching those of native virus particles. The average resolution of 9 Å determined by gold-standard Fourier-shell correlation (FSC) permitted rigid body fitting of domains I to IV of post-fusion gB with a high degree of confidence (Figure 1.6). The result is an unambiguous model of pre-fusion gB domain architecture, presenting a rigid framework for rational design of targeted structural studies, and for validation of molecular models obtained through more reductionist approaches.

Initial map validation

Initial model validation was performed by plotting positions of yellow fluorescent protein (YFP, Figure 1.8) insertions on the proposed pre-fusion model (Gallagher *et al.*, 2014). Functional insertion mutants at positions 304, 361, 470 and 476 were all positioned on the outside of the protein with sufficient space to fit 3-times 5 nm beta-barrels. Interestingly, expressed but non-functional mutants (241, 664) were at the interface between domains I and IV, indicating that interaction, or the angle between these domains is important for regulation of the pre- to post-fusion transition.

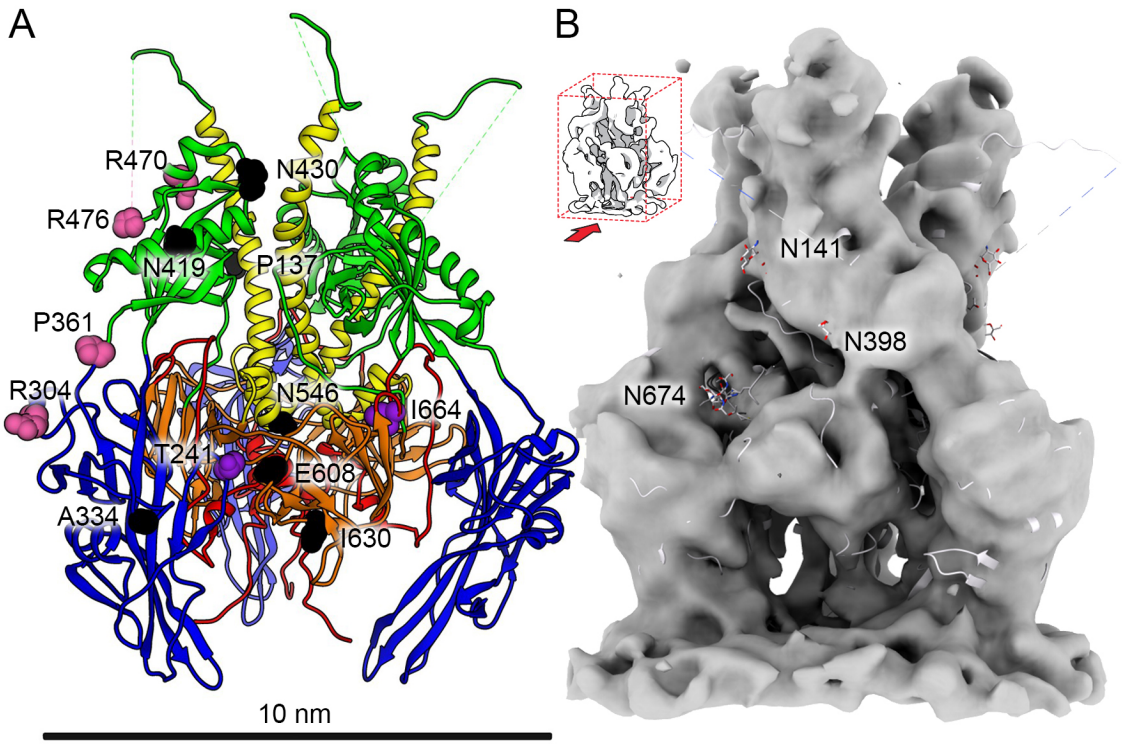


Figure 1.8 Initial validation of the pre-fusion gB model. (**A**) Positions of YFP insertion mutants (Gallagher *et al.*, 2014) are indicated with residues corresponding to the beginning of the inserted protein. Residues in pink show insertions that were functional, purple indicates expressed but non-functional and black indicates insertions that were not expressed. (**B**) Position of three glycosylation sites resolved in 5V2S in the pre-fusion model fitted in SVA map are indicated. The predicted glycosylation site N489 is located in domain II-III linker (indicated with blue and white dashed line) that is not resolved in 5V2S (Cooper *et al.*, 2018).

There was a good overall fit of the pre-fusion model inside the SVA map. The only part of the model protruding substantially outside of the SVA map was a beta-hairpin composed of residues 210-223 of domain I (Figure 1.2). This hairpin is involved in an intramolecular interaction with parts of neighbouring domains I and IV in the post-fusion crystal structure. It is conceivable that this hairpin could rotate in order to widen the adjacent 3-strand beta-sheet, which would place it inside the SVA map density.

The best resolved parts of the presented map were a set of central tubular densities running parallel to the 3-fold symmetry axis (Figure 1.6, B). The membrane distal parts were occupied by domain III, and the remainder was very likely to contain a part of domain V. Unfortunately, domain V architecture in the post-fusion conformation is composed primarily of long segments lacking secondary structure, with the exception of 2 short alpha helices. Residues 660-688 were tentatively fitted running anti-clockwise along the boundary between domains I, II, III and IV (Figure 1.6, B, C) and then towards the membrane, accounting for volumes not occupied by domain I after rigid body fitting (Figure 1.6, C). This oriented the glycosylation site T676 to face solvent; the two short alpha helices of domain V, starting at positions 690 and 701, were conveniently positioned to fill in the missing parts of the tubular densities mentioned previously (Figure 1.6, B). The remaining residues 724-752 are not resolved in crystal structures but it is plausible that they play a role in shielding the domain I fusion loops from forming an irreversible interaction with lipids of the viral envelope.

The transmembrane vacuum

The lack of density for the transmembrane helices was puzzling, considering that there has to be a connection between the ectodomain and the C-terminal globular domain

observed in the SVA map. However, this phenomenon is common in SVA maps of structures in, or close to the plasma membrane such as enveloped viruses or membrane vesicles; it is a residual CTF artefact of the strong bilayer density (Kudryashev *et al.*, 2016, Riedel *et al.*, 2017). This, in principle, could be reduced by amplitude correction through Wiener filtering, but this is challenging to do in SVA and was not performed with these data. It was therefore difficult to judge whether the transmembrane helices were missing due to disorder, multiple conformations, or a CTF artefact. Nevertheless, the approximate position of the transmembrane helices could be inferred, albeit with low confidence, from the putative orientation of membrane proximal amphipathic helices (Figure 1.6, D). These were fitted in tubular densities (with local resolution ~ 10-12 Å, Figure 1.5, D) running parallel to the membrane in two opposing orientations. Both cases would disrupt the transmembrane helix-helix interaction observed in 5V2S and the C-terminal globular domain (Cooper *et al.*, 2018). The intraluminal globular density, which was the likely location of the C-termini, was poorly resolved and was not fitted with any residues. The lack of resolution relative to the rest of the map might further support the existence of multiple conformational states in this region, but additional evidence is required to validate this hypothesis.

The N-terminus remains unclear

Another part of the gB primary structure not assigned in the presented model were the N-terminal residues 31-103. Much of this sequence was predicted with high confidence to be disordered, and available crystal structures end with residue 103 as a part of domain IV, pointing away from the protein (Figures 1.2, B and 1.3, A). This outward

facing orientation was preserved in the pre-fusion model and there is no further density in domain IV to accommodate more residues. There was a small solvent-facing pocket of unassigned density in domain II (Figure 1.7) formed mostly by hydrophobic residues V407, I449, T402 and M366. This pocket was occupied by a domain III loop in the post-fusion conformation; it could induce binding of a short segment of the N-terminus. N-terminal residues 97-106 were predicted to form a short helix, which was not present in X-ray structure models. It is possible that this ~ 1.5 nm long helix is formed in the pre-fusion conformation and points towards the hydrophobic pocket through a "bridge" between domains IV and II (Figures 1.6, A, 1.7). This bridge was populated with part of the domain V flexible loop in the current model. There is currently no evidence to suggest either assignment is correct. The largest unassigned volumes in the presented map are the membrane-distal tips, which were poorly resolved and expanded rapidly at lower contour levels. The large volume of low, poorly resolved density was consistent with partially ordered, or transiently interacting polypeptide chains. A small part of this region was expected to contain residues 477-490 which link domains II and III, and were not resolved in crystal structures. Antibodies that bind to N-terminal residues have been reportedly detected in human sera (Wittekindt *et al.*, 2000), which support its exposed, membrane-distal position.

The fusion loop downfall

Using a substantially lower resolution map, Zeev-Ben-Mordehai and colleagues (2016) speculated that domain I was oriented with fusion loops pointing upwards, away from the viral membrane. The opposing assignment of domain I in this study, with the fusion

loops directed downwards towards the viral membrane, raised the question of how the fusion loop-membrane interaction can be weak enough to be dissociated prior to host-membrane binding, yet strong enough to catalyse fusion. A plausible explanation is that the amphipathic stretch of residues 725-752, that are not resolved in crystal structures, may shield the fusion loops from irreversible membrane binding. Alternatively, gB clustering (Figure 1.9), or interaction with gD or gH/L could lead to (partial) lipid exclusion in a manner similar to influenza hemagglutinin (Bentz, 2000). The preference of the gB pre-fusion conformation in larger vesicles (Figure 1.4) might indicate that it is possible to trigger the transition to the post-fusion form by inducing membrane curvature. It is intriguing to speculate on the potential role of gB clustering for membrane fusion (Figure 1.9, E) as it was possible to see clusters of post-fusion gB with higher-than-surrounding membrane curvature on WT virions (Maurer *et al.*, 2013). Regardless, any model of membrane fusion mechanism through gB must account for the puzzling existence of fusion loops in the viral membrane.

Mechanism of H516P pre-fusion stabilisation

The SVA map resolution of gB H516P was substantially higher than that of previously published data (Zeev-Ben-Mordehai *et al.*, 2016). This is almost certainly due to higher number of sub-volumes included in the final average in the present study (1,900 vs. 49,000). Native membrane vesicles contained roughly equal proportions of both short and long forms of wild-type gB (putative pre- and post-fusion conformations, respectively), making it challenging to obtain a homogeneous population of either. The apparent ability of gB to spontaneously switch from pre- to post-fusion conformation

suggests that the pre-fusion state can access a large number of conformational states that collectively look like the short form due to the low SNR of cET data. As a result, the highest resolution average of WT gB was achieved with a small fraction of the total number of particles (Daven Vasishtan, personal communication). On the other hand, vesicles obtained by expression of gB H516P contained almost exclusively the short form, which allowed more particles to be picked with higher confidence. This would imply that the higher resolution of the gB H516P SVA map also reflected an overall reduction of variability of the mutant pre-fusion conformation.

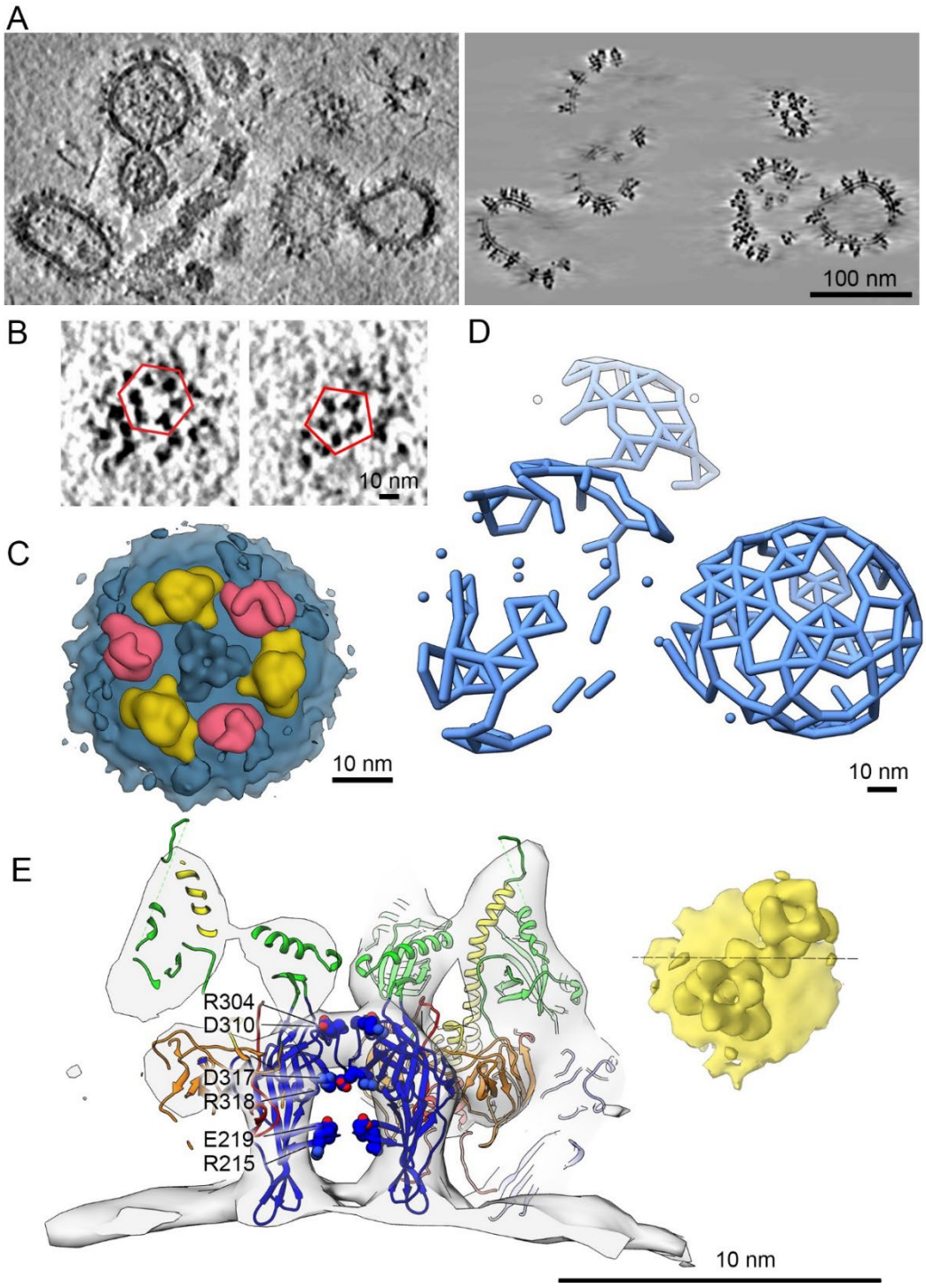


Figure 1.9 Pre-fusion gB forms flexible homotypic interactions. (**A**) A slice through tomogram (left) and a volume generated by backplotting SVA map into positions refined by SVA (right). Both volumes were filtered with the same parameters and have equivalent missing wedges. (**B**) Tomogram slices indicating the presence of different arrangement of gB trimers on the surface of vesicles. (**C**) Top view of a SVA volume generated by aligning particles without using a mask. The volume was segmented in Chimera to indicate the position of 1° (yellow) and 2° neighbours. (**D**) 3D model indicating the connectivity between gB trimers. Positions of particles (blue spheres) in tomogram shown in (**A**) shorter than 14 nm were linked by sticks. (**E**) Molecular model of trimer-trimer interaction. Two pre-fusion models were fitted in SVA map of gB-neighbour interaction shown in yellow in Figure 1.8. The volume was sliced in the position indicated by a dashed line (left). There were six pairs of acidic and basic residues between the two models that were in sufficient proximity to form salt bridges.

Proline is a strong alpha-helix breaker, which suggested that the transition to post-fusion conformation proceeds through the straightening of domain III helices as a pre-requisite to formation of the central coiled coil. Domain III residues N-terminal of H516P were in close proximity to domain II which highlighted the potential role of this region for regulation of transition to the post-fusion conformation. Unfortunately, the resolution in this region was not sufficient to model any conformational changes relative to the post-fusion structure. The pre-fusion model therefore consists of a rigid fit of 5V2S domain III, which was then refined by a molecular dynamics simulation. This resulted in a slight bending of the domain III helix closer towards domain II, however, it is unclear if this is relevant.

The nature of the post-fusion structure of domain II introduced further uncertainty for modelling the pre-fusion structure of domain III. A short domain II helix composed of residues 465-474 was assigned in 5V2S (and others) but it was missing in 2GUM (Fig. 1.10, A and B). Analysis of the differences in crystal packing between these two structures indicated that the 465-474 helix was stabilised by interaction with a large hydrophobic pocket around V574 and V613 of domain IV (Fig 1.10, D). Furthermore, its interaction with the rest of domain II was mediated predominantly by hydrophilic residues, which would make it unstable in solution (Fig 1.10, C). It is tempting to suggest that in the absence of the crystal packing interaction, this short helix would instead interact with domain III residues 491-501 that are predicted to form a short beta-strand. The remaining unassigned residues are rich in proline and could conceivably mediate a transient interaction with the unstructured N-terminus.

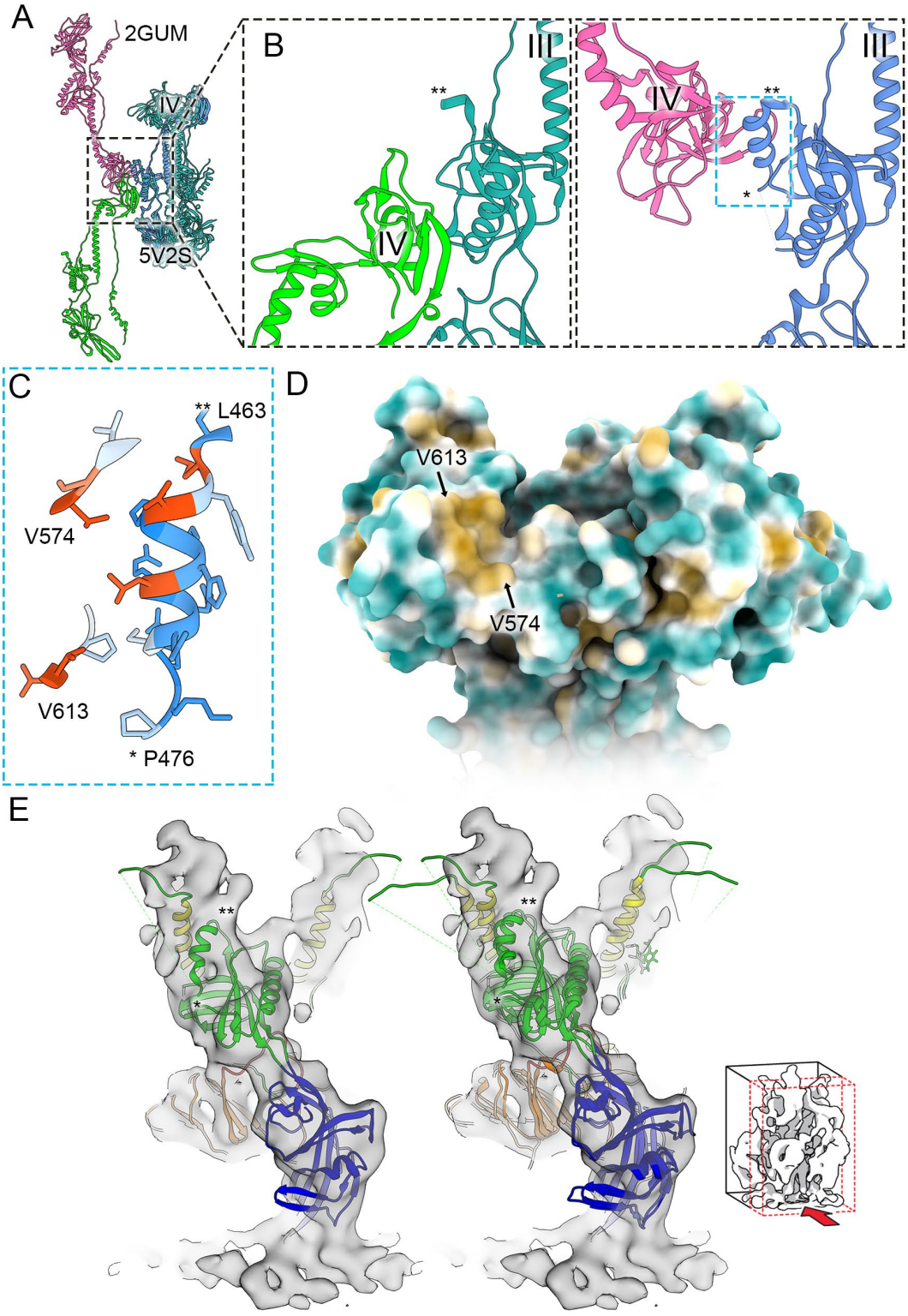


Figure 1.10 Reorganisation of domain II helix 463-476. (**A**), (**B**) Comparison of crystal packing in 2GUM and 5V2S. The orientation of the 463-476 helix is indicated with asterisks. (**C**), (**D**) Stick representation of residues coloured by hydrophobicity: red (orange), white, and blue colour represents hydrophobic, neutral, and hydrophobic residues, respectively. (**C**) Zoomed-in region highlighted with cyan dashed lines in (B). Shown are residues of the 463-476 alpha helix and domain IV residues contributing to the crystal contact between neighbouring gB trimers. This indicates that the domain II-IV interaction interface is mediated primarily by hydrophobic contacts. (**E**) Shows the position of domain II helix 463-476 in the pre-fusion model after MD (left). The overlap between the manually fitted and MD-refined model is shown to the right.

Future directions

Determination of the putative gB pre-fusion conformation is a starting point for designing targeted structural and functional experiments. A necessary first step will be the validation of this model by mutagenesis experiments. A set of well-designed cysteine mutants should lock the protein in a pre-fusion conformation, which might make it amenable to high-resolution structure determination by X-ray crystallography or single particle cryo-EM. An atomic model based on a high-resolution structure would be a step forward towards determining the molecular mechanism of gB membrane fusion. However, this mechanism has not been determined for the VSV G protein, despite the availability of X-ray crystal structures of both the pre- and post-fusion conformations. Determining the molecular mechanism will likely require structural information about one or more structural intermediates that occur during membrane fusion.

More enticingly, the trigger for this rearrangement remains unknown. Despite the structural insights into the pre-fusion structure outlined here, there are no suggestions towards its identity. The identification of this trigger would help resolve the more puzzling aspects of the mechanics of gB-mediated membrane fusion, particularly with regard to fusion loop sequestration and deployment, and the role of the other glycoproteins, particularly gH/L, in membrane fusion.

As this fusion event is the last prelude to cell entry, it is an attractive target towards drug towards prophylactic treatment or vaccine development. Stabilising the pre-fusion conformation has the potential of rendering virus particles incapable of entering cells.

Cell entry is the ideal stage of interrupting the virus live-cycle, especially for viruses that integrate into the host genome, such as HSV-1.

1.4 Materials and methods

Specimen preparation

This section was contributed by BV. Vesicles were prepared as described previously (Zeev-Ben-Mordehai *et al.*, 2014). In Brief, BHK-21 cells were grown in GMEM supplemented with 20 mM Hepes pH 7.4, 2% (v/v) TPB and 2% (v/v) FBS. At 70-80% confluency, cells were transiently transfected with modified versions of the plasmid for gB (pEP98 originally received form G. Cohen (University of Pennsylvania, Philadelphia, Pennsylvania, USA). Cells were grown for an additional 48 h with a media exchange to serum free GMEM after 24h. Vesicles were harvested from the supernatant by differential centrifugation and resuspended in 20 mM Hepes pH 8, 150 mM NaCl.

Cryo-EM grids were prepared by applying 3.5 µL resuspended vesicles onto Quantifoil R2/1 (Quantifoil). After adding 1.3 µL 10 nm colloidal gold fiducials (Aurion), grids were manually blotted and plunge frozen in a mix of liquid ethane/propane and kept at liquid nitrogen before imaging.

Electron Microscopy Data Acquisition

Tomograms were collected on Tecnai F30 “Polara” (referred to as Polara, FEI/Thermo) or Titan Krios (FEI/Thermo) at 300 kV with a post-column QUANTUM energy filter

(Gatan) operated in Zero-Loss mode using 20 eV energy slit and K2 Summit direct electron detector operating in counting mode (Gatan). Please see Table 1 for data acquisition parameters. A 70 µm C2 aperture was in place during all data acquisition. Tilt series on Polara were collected bi-directionally from 20° to -58° and 23° to 59° and with 6 frames per micrograph; tilt series on Krios used a dose-symmetric scheme from 0° to +/- 60° (Hagen *et al.*, 2017) in 3° increments and without frame fractionation.

	Pixel size (Å)	Defocus range (µm)	fluence per tilt ($e^-Å^{-2}$)	Total fluence ($e^-Å^{-2}$)	Acquisition scheme	N tomo-grams	Mean thickness (nm)
Krios data	1.6 (0.9**)	2.3 – 4.9	3.5	143.5	Dose-symmetric	46	~ 60
Polara data	1.35	1.6 – 3.5	2.3/5.5*	94.3/ 225.5	Bidirectional	53	~ 150

Table 1 Data acquisition parameters. * 8 tomograms were collected with 5.5 $e^-Å^{-2}$ per tilt. ** Krios data was collected at 0.9 Å pixel size at super-resolution mode, and Fourier cropped to 1.8 Å. Pixel size was then set to 1.6 Å after size comparison with averages from Polara data.

Data Processing and tomogram reconstruction

Frames of collected tilt series were aligned using Unblur (Grant and Grigorieff, 2015) or SerialEM plugin (Mastronarde, 2003). Defocus estimation was performed using IMOD *ctfplotter* (Kremer *et al.*, 1996), phase-flipping was performed in NovaCTF (Turonova *et al.*, 2017) and dose-weighting by IMOD *mtffilter*. Tomograms were aligned using IMOD Etomo (Kremer *et al.*, 1996) and subsequently using NovaCTF, which was parallelised by a bespoke Python script (Joblib), with the exception of 8 tomograms that were reconstructed using Etomo's local-alignment. Two sets of tomograms were reconstructed: a set with all available tilts (all-tilt tomograms) and a second set using tilt series that had tilts collected above 20° and below -20° replaced by blank images filled with the tilt series mean intensity (low-tilt tomograms). This resulted in two sets of

tomograms with identical geometries, but different number of tilts included. Tomograms were binned 2, 4 or 6 times using IMOD *binvol* and filtered for visual inspection and manual picking using *bfilter* (Heymann and Belnap, 2007).

Sub-volume averaging

Particle picking and initial position refinement

Particles were picked manually using 3dmod (IMOD); 18,279 particles were picked in Polara tomograms and 37,897 were picked in Krios tomograms. SVA was performed using PEET (Nicastro *et al.*, 2006, Heumann *et al.*, 2011). A set of bespoke Python scripts based on TEMPy (Farabella *et al.*, 2015) called "PEET extensions" (pex) were written by Daven Vasishtan for particle processing outside PEET. Script names are given in italics. The main steps of SVA and the corresponding FSC plots are depicted in Figure 1.11 and Figure 1.12 respectively. Initial references were generated by averaging of manually picked particle positions oriented to align their Y-axes (*pex_make_model_using_centers*); particle rotational angles were then refined with all-tilt tomograms. Aligned sub-volumes were cleaned by distance to nearest neighbour, normalised cross-correlation coefficient (*pex_remove_duplicates*), or by classification (*pca* and *clusterPCA*, PEET) (Heumann *et al.*, 2011) at multiple successive stages. After reaching a high-quality average (judged subjectively by e.g. SNR and absence of masking artefacts) the particle orientations were scrambled by random rotation around the Y axis (maximum 360°) followed by a random rotation (maximum 15°) around a randomly selected axis (*pex_randomise_particles*). Two particle subsets for unbiased FSC

determination (those with odd or even particle ordinals) were created by *pex_split_for_fsc*.

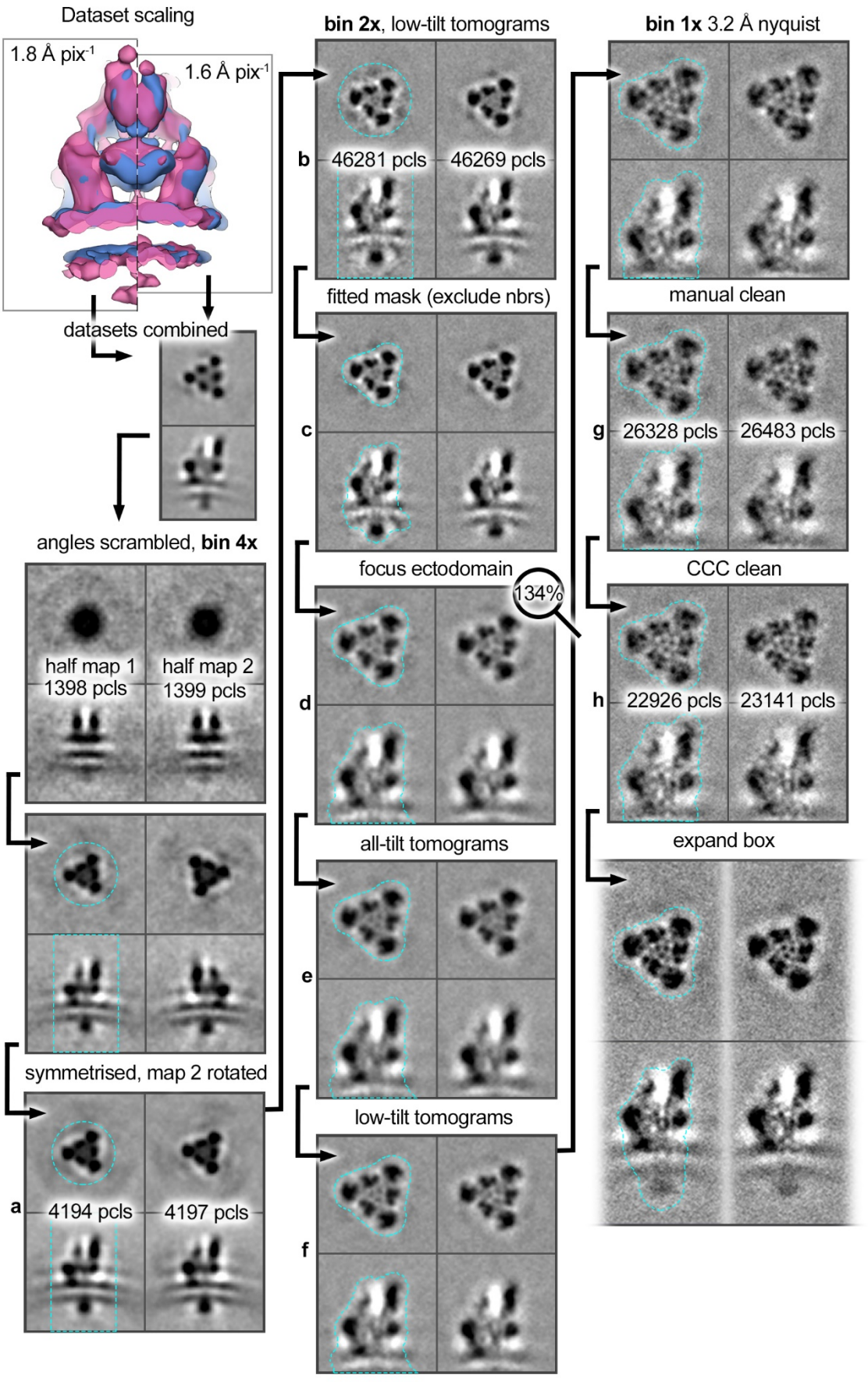

Dataset scaling
1.8 Å pix-1
1.6 Å pix-1
datasets combined
angles scrambled, bin 4x
half map 1
1398 pcls
half map 2
1399 pcls
symmetrised, map 2 rotated
a
4194 pcls
4197 pcls
bin 2x, low-tilt tomograms
b
46281 pcls
46269 pcls
fitted mask (exclude nbrs)
c
focus ectodomain
134%
d
all-tilt tomograms
e
low-tilt tomograms
f
bin 1x 3.2 Å nyquist
manual clean
g
26328 pcls
26483 pcls
CCC clean
h
22926 pcls
23141 pcls
expand box

Figure 1.11 Overview of SVA steps. The order of SVA steps that lead to the highest resolution average volume, depicted as boxes, is arranged top to bottom, left to right, starting in top left corner. Each box shows central slices through SVA half maps (left and right) viewed perpendicular (upper) and parallel to the membrane bilayer. The outline of masks used for alignment are highlighted with cyan dashed lines. Magnifying glass at step (**d**) indicates increased scale of SVA averages in this figure only. Lower case letters indicate steps where FSC was determined (Figure 1.12). Each step depicted typically involved several iterations within PEET. As a rule, particle angles were refined during steps where all-tilt tomograms were used, and only translations were refined with low-tilt tomograms. Angular refinement with low-tilt tomograms invariable lead to model (noise) bias, as judged by modest increase in high-resolution and reduction in low-resolution FSC. This was also accompanied by appearance of filamentous features within, but not outside the mask.

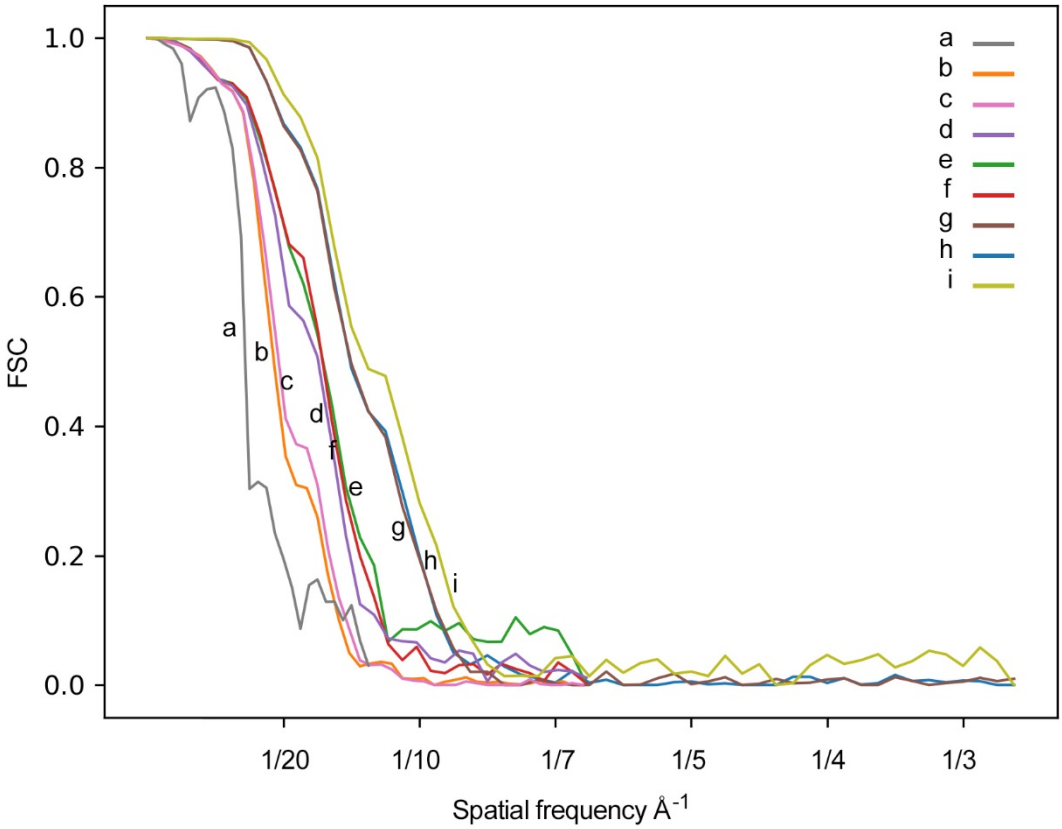


Figure 1.12 Gold-standard FSC of SVA steps depicted in Figure 1.11. FSC curves (**a**-**i**) were determined at steps labelled a-i in Figure 1.11. Each subsequent SVA step in Figure 1.11 corresponded to an overall increase in resolution, with the exception of steps (e, green) and (f, red), where all-tilt tomograms were replaced with low-tilt tomograms. In this step, the FSC dropped at higher-resolution shells around 1/14 $Å^{-1}$, but mainly between 1/10 and 1/7 $Å^{-1}$ where it was likely the result of noise correlation. The difference between curves (**h**) and (**i**, olive) is the result of volume masking (same as Figure 1.5, E).

Averaging and self-consistency check between SVA half-data sets

Initial independent averages for the two half-datasets were generated by averaging (*averageAll*, PEET), aligning and symmetrising (*pex_symmetrise*) of particles from Polara tomograms acquired with 5.5 $e^{-}Å^{-2}$ per tilt. These were used as references for subsequent alignment of all particles within each half-dataset. All-tilt tomograms were replaced by low-tilt tomograms after reaching a "resolution-improvement plateau". Importantly, only translations were allowed for alignment of low-tilt tomograms due to their larger missing wedge. Alignment was focused on the protein ectodomain (including the outer membrane leaflet) after a resolution-improvement plateau around 13 Å (~100,000 symmetrised particles). Angles were refined at this stage with all-tilt tomograms followed by further low-tilt translation refinement. Particles were cleaned by plotting their position and orientation as atom-bond pairs in UCSF Chimera (Pettersen *et al.*, 2004) (*pex_make_chim_markers_from_prm*) where they could be manually selected. The corresponding pairs of particles and orientations were removed from PEET models and initial motive lists using *pex_clean_using_marker_file*. Particles were then symmetrised and aligned to references from previous SVA steps. An average volume containing the protein C-terminal domain (Figures 1.8 A, B, 1.13) was obtained by expanding the alignment box and mask, and allowing translation refinement. FSC was calculated between half-data set averages masked with a binary mask and a soft-edge mask in order to avoid mask correlation (*bresolve*, *bmask*, *Bsoft*, *clip*, IMOD). Due to a slight misalignment between the half-data set averages, one half-map was aligned to the other in Chimera before FSC calculation. The 0.143 FSC cut off was used to determine the ectodomain (9.0 Å) and the whole protein (10.1 Å) resolution.

Generation of combined sub-volume average

The final average containing both half-data sets (~60,000 particles) was generated by merging particles after manual cleaning and aligning their positions to the sum of the half-data set averages. The experimental B-factor was estimated using *embfactor* (Fernandez *et al.*, 2008) to ~ 400 Å^2. A more conservative value of -300 Å^2 was applied to combined averages using *bfilter* (Bsoft).

Model building

Crystal structure of post-fusion gB (5V2S) was adjusted by manually shifting and rotating atoms of individual domains in Chimera. The rigid fit of domain IV was used as a starting position and a reference point for symmetrisation of protomer models. This model was submitted to Namdinator (Kidmose *et al.*, 2019) with a B-factor filtered SVA map using the default parameters (20,000 steps). Visualisation and figure generation was performed in Chimera or ChimeraX (Goddard *et al.*, 2018).

Chapter 2 Fixing tomograms with Flexo

2.1 Introduction

EM imaging is extremely damaging to the specimen

Transmission electron microscopy imaging inflicts extensive damage to cryogenically preserved biological specimens. This is due to the high proportion of inelastic scattering events that deposit energy in the specimen, and the extremely high potential energy of the incident electrons used for imaging. 370 $MJKg^{-1}$ is deposited in proteinaceous specimens illuminated with 100 $e^{-}Å^{-2}$ accelerated to 300 kV (Baker and Rubinstein, 2010). In contrast, the energy released by combustion of protein is ~23 $MJkg^{-1}$ (Paladines *et al.*, 1964) meaning that a typical tomographic acquisition deposits enough energy to break all bonds in a specimen many times over. At 300 kV the potential energy of each electron is ~ 300 keV, which is many orders of magnitude higher than energy stored in any single bond of biological macromolecules, which are generally in the order of single eV. On average, inelastic scattering events deposit on average 20 eV (~ 5 – 100 eV). This generally results in the ionisation of valence shell electrons, leading to bond breakage. Carbon-hydrogen bonds are broken much more frequently than carbon-carbon bonds (Symons, 1982); the net effect is a build-up of hydrogen gas, which can be observed as the formation of bubbles at sufficiently high exposures (between 60 and 400 $e^{-}Å^{-2}$, depending on the specimen). Importantly, there is very little hydrogen gas produced by pure vitreous water (Leapman and Sun, 1995); it is mainly biological macromolecules and small organic molecules that cause bubbling (Meents *et al.*, 2010).

Local and global distortions attenuate high-resolution information

The breaking of a covalent bond between two atoms causes their internuclear distance to increase substantially. For example, the hydrogen-oxygen bond length in a molecule of water is ~ 1 Å, compared to ~ 2 Å of the intermolecular hydrogen bond (Jeffrey, 1997, Petrenko and Whitworth, 2006). This distance becomes much larger in cases where the leaving group is a gas. This leads to the decay of high-resolution information, since the atomic structure of the observed molecule changes as it is being imaged. This effect has been quantified by determining average 3D maps of isolated virus particles suspended in vitreous ice (Grant and Grigorieff, 2015) or by measuring diffraction spot intensities of 2D crystals (Baker *et al.*, 2010). Comparing these data, the rate of decay matches at frequencies above ~ 0.25 $Å^{-1}$ but low-resolution information decays substantially faster in 2D crystals. Low resolution decays much faster in crystals because it depends on a high degree of order over very large distances. The cumulative effect of a large number of bonds being broken is that the specimen expands, which leads to large scale distortions referred to as warping. cET suffers from warping to a similar extent as 2D crystals because the whole field of view (typically several hundred nanometres across) is essentially a single entity whose projections need be aligned precisely to preserve high-resolution information.

Compensating for specimen damage is difficult in 3D

Homogeneous specimens, such as evenly distributed proteins in solution, can exhibit relatively predictable motion, which is often referred to as “drumming”. Assuming constant acquisition geometry (no stage tilt), out of plane motions of individual particles

become projected into lateral motion. Fractionating projection images into frames with sufficient SNR, combined with frame to frame alignment of local patches, can make warping an insignificant factor within achievable resolution limits. This approach is not possible with tomographic tilt series because of the changing specimen geometry during tilting. Furthermore, specimens used for cET, such as cells or pleomorphic viruses, undergo larger and much more heterogeneous distortions due to the high protein content, uneven distribution and varying susceptibility of specific molecules to radiation damage (Figure 2.1). Moreover, thicker specimens (more than 50-100 nm) can no longer be approximated as a single sheet of material, as radiation-induced motion can vary substantially between the two surfaces. Two different solutions to this problem have been proposed: Fernandez *et al.* (2018) demonstrated that warping could be (partially) compensated for by modelling specimen warping over time as a continuous polynomial to which positions of gold fiducial markers are fitted. This method depends on a high density and homogeneous distribution of fiducial markers, which is often difficult to achieve. Himes and Zhang (2018) used sub-volume averages of biological molecules as references for template matching against projections of individual molecules in each tilt. Each molecule essentially becomes a fiducial marker that can be used for localised tomographic reconstruction performed by IMOD (Kremer *et al.*, 1996).

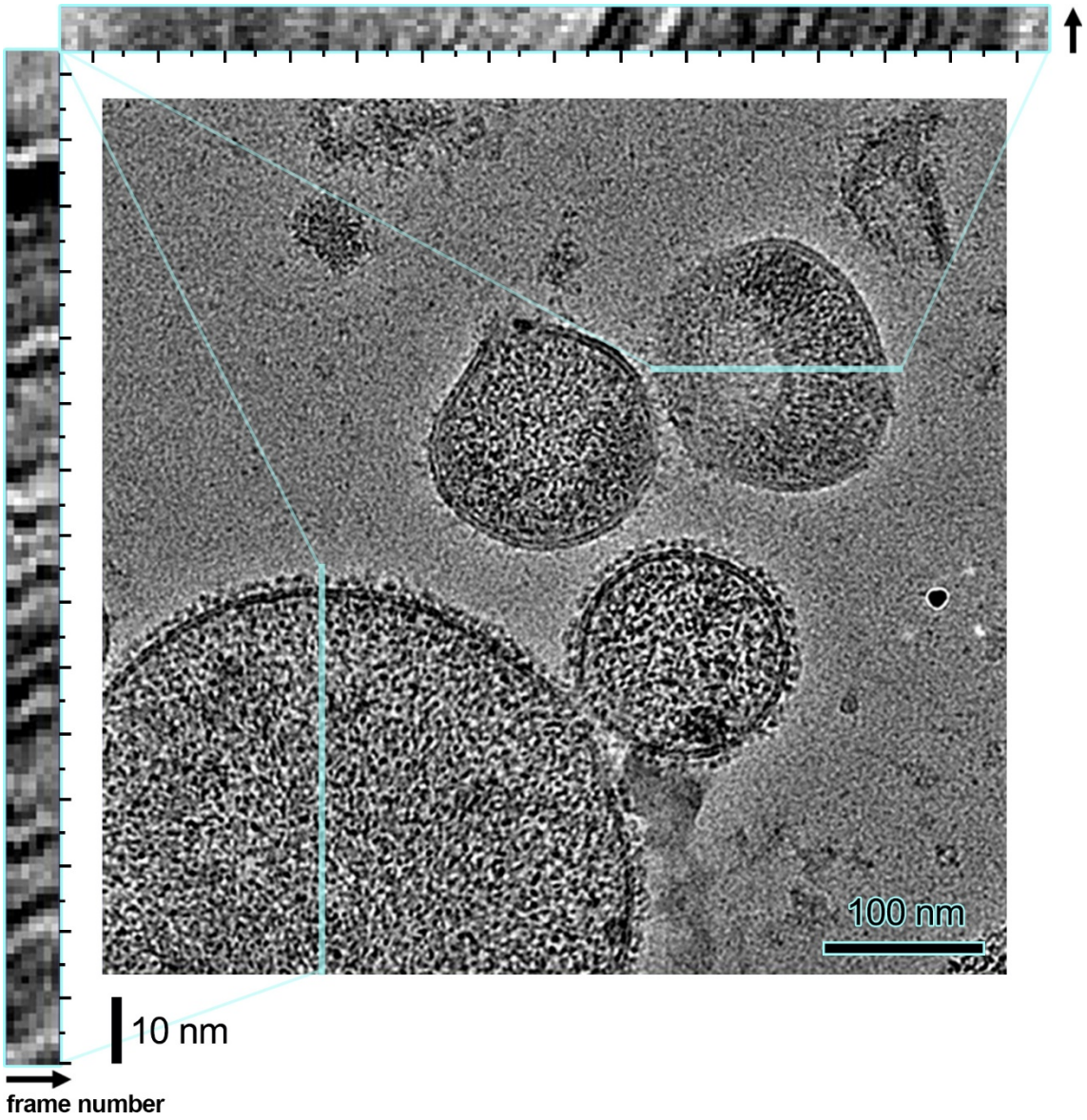


Figure 2.1 Demonstration of warping in complex specimens. A projection image of several glycoprotein-coated vesicles was acquired at 0° stage tilt. Image acquisition was fractionated into 8 frames with a fluence of 11 e^-A^2 per frame (88 total e^-A^2). Frames were aligned using a gold fiducial marker to account for unidirectional drift. The resulting frame sum is shown. Cyan lines indicate regions of individual frames that were plotted over time. The resulting kymographs are shown above and to the left of the image sum. Distance between major tick marks represents 10 nm. Large translations of individual structures can be observed as diagonal lines. Translation of less than 5 nm was observed for the majority of structures despite a total electron fluence lower than that used for a typical tomogram.

Flexo: a simple implementation of an existing concept

This chapter describes the development and output of a program called Flexo that can compensate for warping in tomographic data. It is based on the concept of using the density of biological structures as direct fiducial markers, the same approach used by

Himes and Zhang (2018) in a program called emClarity. While the concept is the same, it is the implementation that matters. Both the installation and the use of emClarity is challenging due to poor documentation and a lack of source code annotation. The ultimate goal for Flexo was for a well-documented and user-friendly program well integrated with IMOD that could increase tomogram quality, especially where the number of fiducial markers is limited. Lindsay Baker and Daven Vasishtan (DV) were instrumental in discussions relating to image processing and alignment, and DV contributed to code and debugging. Christoph Pratsch contributed Python code for CTF convolution and bandpass filtering. Presented in this chapter are examples of three types of tomograms that were refined by Flexo: A tomogram of cell periphery originally aligned with 5 nm gold fiducial markers (acquired by VP), a focused ion beam (FIB) milled lamella of nuclear-cytoplasmic interface (by Michael Grange and Christoph Hagen) aligned by patch tracking, and a thin *in-vitro* specimen of purified ribosomes (Bharat and Scheres, 2016). FIB milling enables material to be removed from specimens using a beam of (gallium) ions which eject the impacted atoms. This allows cryogenic specimens to be thinned without affecting their vitreous state, making it possible to image regions of the cell that would otherwise be inaccessible due to thickness. At the same time, there are currently no fiducial markers that can be inserted into cells in sufficient density and without affecting their physiology. As a result, tilt series of FIB milled lamella are difficult to align with high precision.

2.2 Results and discussion

Description of Flexo architecture and workflow

Flexo builds on and attempts to improve tilt series alignment generated by IMOD Etomo (Figure 2.2). The first steps of the workflow involve tomogram alignment and reconstruction in Etomo, followed by sub-volume averaging of (biological) structures (particles) found within using PEET, which is then used as reference for tilt series alignment.

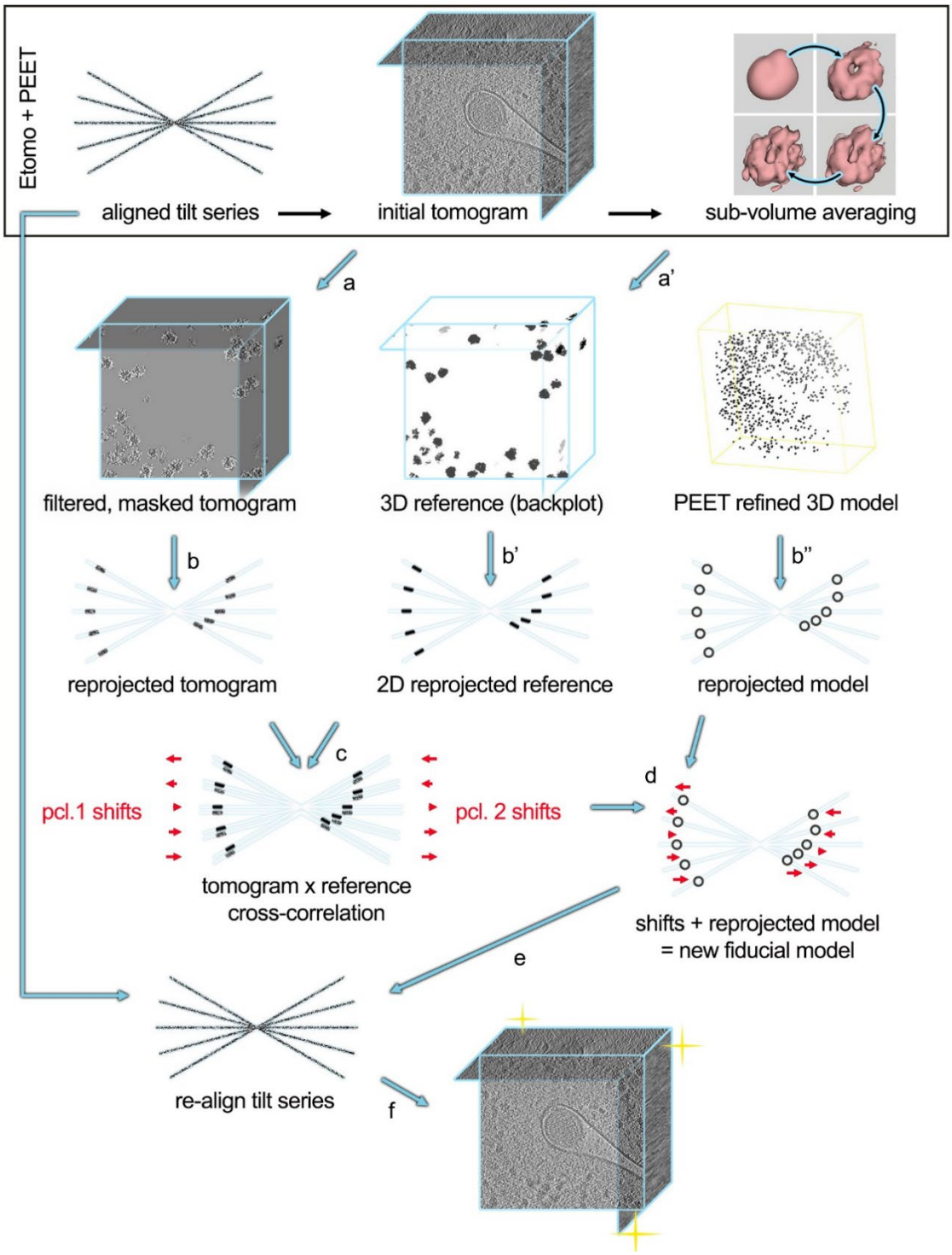


Figure 2.2 Flexo processing architecture. Initial tilt series alignment, tomographic reconstruction and SVA was performed within IMOD and PEET. Flexo used the 3D coordinates of particles refined by PEET and a supplied density map in order to generate a 3D tomogram reference (a'). This reference was dilated and converted into a binary mask used to mask tomogram densities around the averaged particles (a). This masked (and filtered) tomogram, the 3D reference, and the 3D refined model were reprojected into a reprojected tomogram, 2D reference, and a reprojected 2D coordinate model (b, b', b''). Translation search by Fourier cross correlation between the reprojected tomogram and 2D reference was performed at each 2D particle coordinate, resulting in an array of shifts (c). These shifts were then added to the 2D particle model, and the resulting fiducial model was used to re-align the original aligned tilt series (e), followed by tomographic reconstruction (f). Please refer to table 2 for information on libraries used for each step.

Tomogram reference

The process of sub-volume averaging involves finding the best match between each particle and a reference. The desired output of this process is typically an average density SVA map with a (relatively) high SNR. For Flexo, it is primarily the best matching position and orientation of a reference that is relevant. Placing a correctly rotated copy of the SVA map (or a map obtained through a different structural method) into an empty volume at each particle's position (backplotting) creates a high SNR, missing wedge-free model of the density observed in the original tomogram. Importantly, this model is affected by specimen warping; disregarding the effects of noise, missing wedge and tilting, it represents the average shape of the specimen as it undergoes warping during data collection (Figure 2.3). Nevertheless, simple backplotting of the SVA map results in a reference volume that can reduce blurring caused by warping. This 3D reference is forward-projected (reprojected) into a 2D reference tilt series matching the original aligned data.

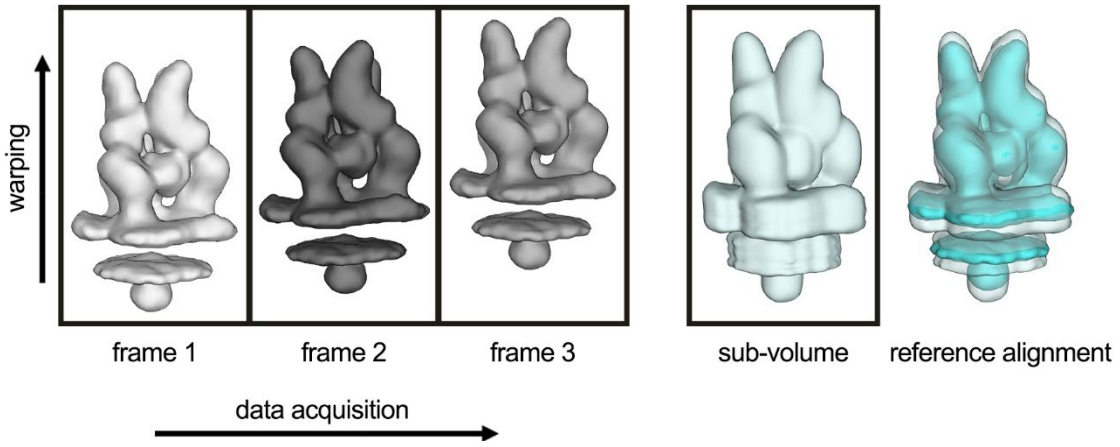


Figure 2.3 Backplotting of reference volumes to particle positions creates an approximation of the specimen's shape averaged over frames of acquired data. Translation of particles in frames 1-3 represents warping during data acquisition. Tomographic reconstruction using this set of data would result in a blurred sub-volume. In an ideal case scenario, SVA would result in the reference being aligned to the mean of this sub-volume. Aligning frames 1-3 to the resulting 3D reference would result in a partially warped tomogram corresponding to the state of the specimen between acquisition of frame 3.

Alignment is performed in 2D

Generation of a 2D reference tilt allows the position of each particle to be compared to its expected position in each tilt. However, the signal in the original data corresponding to any one particle is weak due to shot noise and overlap with other densities. Tomograms were low-pass filtered in 3D to ~ 3 nm with a Gaussian edge in order to reduce high-frequency noise. The overlap with other densities within the specimen was reduced by using a tilt series obtained by reprojecting the original tomogram where all voxels were replaced with the mean voxel value, except for those within a small distance around each particle. Projections of this "masked tomogram" are an approximation of density subtraction above, below, and around each particle, convoluted with the anisotropic low-resolution R-weighting performed during weighted back-projection, (Kremer *et al.*, 1996) and an unknown blurring function resulting from misalignment and warping. Per-particle, per-tilt translation search (by Fourier-space cross-correlation) between a 2D reference and a 2D masked re-projected tomogram resulted in a set of "shifts" that could be considered as the displacement of the observed density compared to the tomogram model. Plotting shifts as a function of tilt angle for each particle indicated that some shifts are exceedingly noisy, especially at higher tilt angles. In an attempt to mitigate this effect, cross-correlation was first performed for tilts collected at lower angles and shifts at higher tilts were restricted to three standard deviations from the mean of low-tilt shifts. In general, there was a benefit to reducing the maximum shift search distance to, e.g. fewer than 10 pixels with tomograms binned by 4 (roughly 10 Å pixel size). These shifts were added to a 2D coordinate model generated by reprojection of the 3D particle coordinates with the same parameters as the 2D reference and the masked tomogram. The resulting fiducial model was refined with

IMOD tiltalign. A robust tuning factor of 0.5 to 1 was used depending on the number of 3D particles and the ratio of mean shift size and standard deviation. Local refinement was used with ~ 40 particles for each patch, but these parameters had to be manually adjusted based on visual evaluation of the resulting tomogram. The large number of particles supplied for tilt series refinement in tiltalign was sufficient to compensate for the large standard deviation of individual shifts. The offsets calculated by tiltalign were applied to the original aligned data to create a new aligned tilt series, which was used for tomogram reconstruction.

Application to specific examples

Flexo was tested with a variety of tomograms from many different specimens, some of the best results are presented in this chapter. Approximately 800 ribosomes were manually picked in a tomogram of a cell periphery that was originally aligned using 5 nm gold fiducial markers, followed by SVA in PEET (Figure 2.4). Simulated map of 4UG0 (Khatter *et al.*, 2015), filtered with a Gaussian edge (full width half maximum ~ 50 nm), was used as the reference volume. The resulting SVA map had a resolution of ~ 8 nm measured by gold-standard FSC at 0.5 cutoff. Visual comparison before and after Flexo refinement revealed several features that could not be clearly interpreted before the procedure (Figure 2.4, A). Importantly, these structures, such as actin filaments, were not used for Flexo processing and are unlikely to be the result of reference bias. The propensity for reference bias was considered low due to the fact that a large number of individual particle shifts were averaged by tiltalign in order to produce the final alignment. However, this could conceivably become a problem in tomograms

containing a uniformly oriented set of particles (e.g. a protein crystal). Subsequent SVA of ribosomes in the Flexo-refined tomogram resulted in a map with ~ 6 nm resolution. There were a large number of 5 nm gold fiducial markers in this tomogram (~ 100) located above and below the cell. Some of these had to be picked manually for initial alignment as the automated procedure in Etomo failed due to their small size and specimen warping. It was possible to refine the fiducial positions in 2D very quickly and with high precision using Flexo. This was done by using the Etomo "findbeads3d" function to locate the gold nanoparticle position in 3D followed by PEET alignment to a binary spherical density. Interestingly, alignment using ribosomes, rather than gold beads, produced the better tomogram. This could be the result of different directions of warping on the surfaces of the tomogram (where the majority of fiducials were located) compared to the cell interior, or the substantially larger number of ribosomes. However, this observation was not quantified.

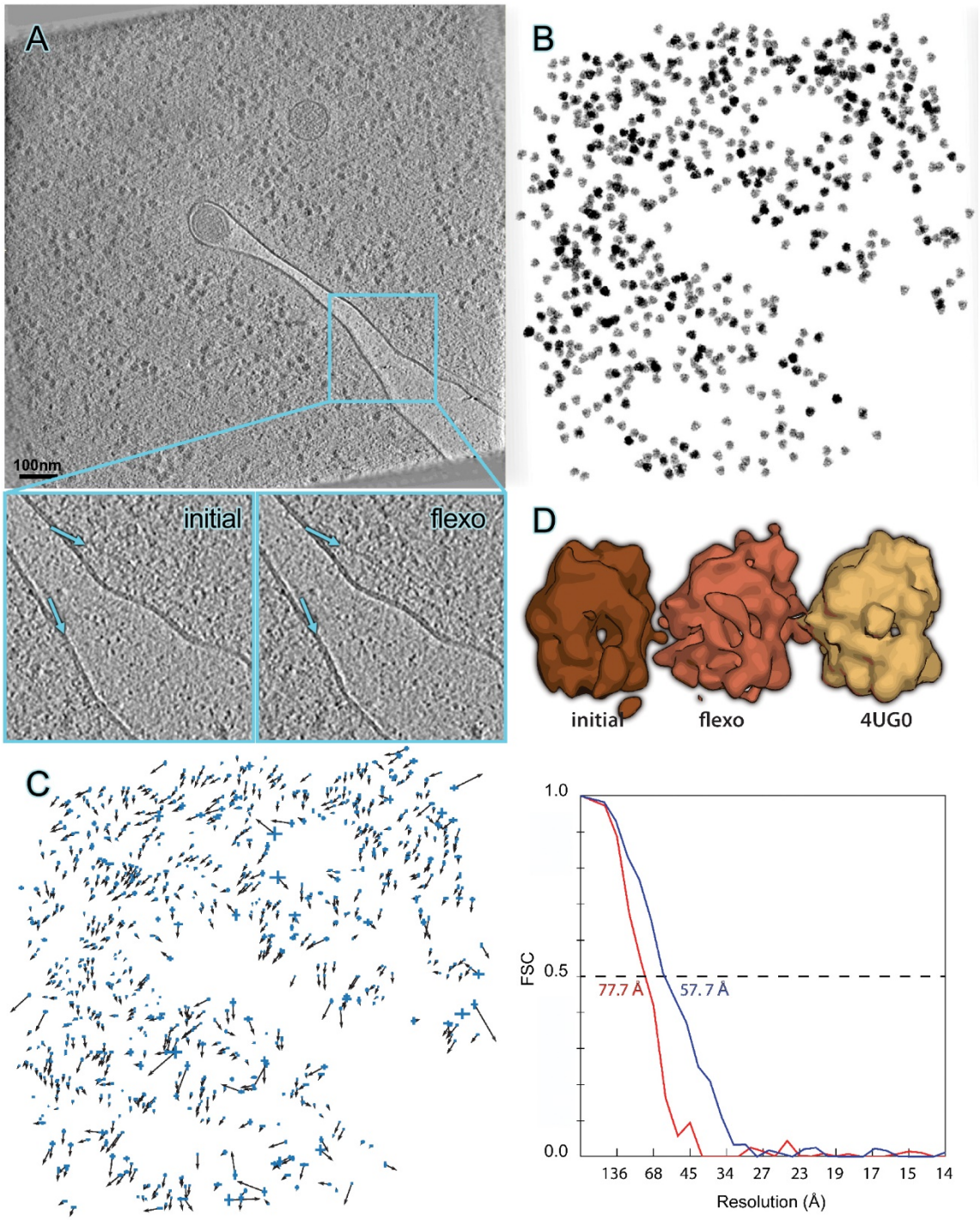


Figure 2.4 Flexo improved alignment of a cellular tomogram using ribosomes as fiducial markers. (**A**) A single slice through the Flexo-refined tomogram is shown. A cyan box indicates the area used for comparison with the initial tomogram displayed below. Recognisable structures, such as an actin filament and cell membrane are highlighted in both for comparison. (**B**) A slice through the 3D reference volume that was used for Flexo alignment. (**C**) Mean particle shifts and standard deviations were plotted at particle XY coordinates as a way of representing the noisiness of Flexo-calculated shifts. The shift size was multiplied by 50; standard deviation was multiplied by 5 for visualisation. (**D**) Comparison of 3D surface rendered SVA maps obtained with the initial and Flexo-refined tomograms and the corresponding FSC curves below. A simulated volume of 4UG0 (Khatter *et al.*, 2015) filtered to 37 Å was included for reference.

In the next example, a tomogram of the nuclear periphery was initially aligned using patch-tracking within Etomo due to the absence of reliable fiducial markers (Figure 2.5). Ribosomes and icosahedral virus capsids were averaged in PEET and used for Flexo refinement. The general quality of the tomogram, judged by visual comparison, was improved. Features, such as membrane bilayers and (putative) intermediate filaments that were substantially blurred in the initial tomogram could be clearly resolved in the Flexo-processed tomogram.

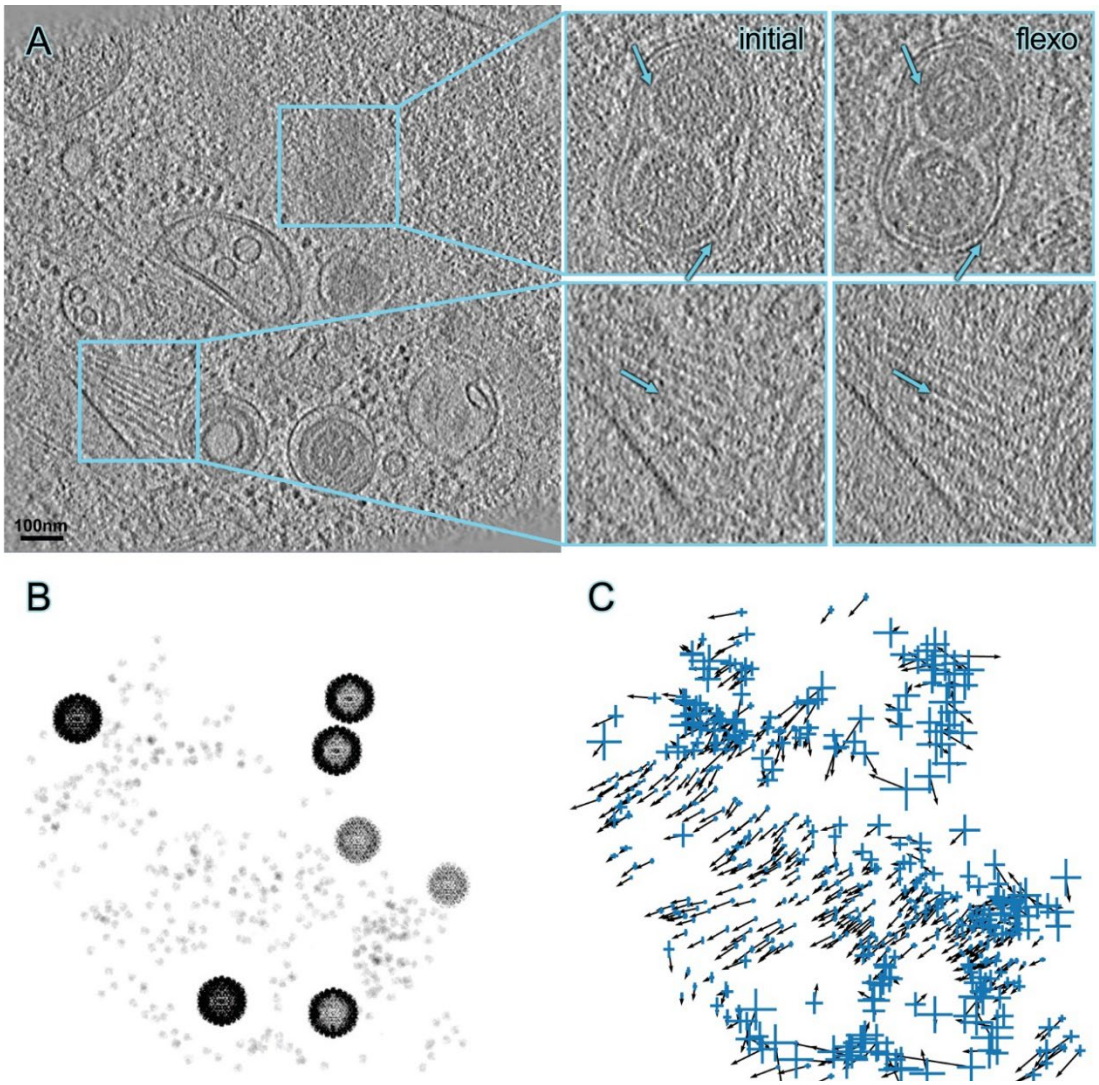


Figure 2.5 Tomogram of a lamella was improved despite extremely noisy shifts. (**A**) A section through the Flexo-refined tomogram with cyan boxes indicating regions where it was compared to the initial reconstruction. Features such as virus capsid penton and hexons, and parts of the vesicle membrane are clearly visible after Flexo refinement, but not before. (**B**) A section through the 3D reference used for unwarping. Both ribosomes and virus capsids were used concurrently. (**C**) A plot equivalent to figure 2.4, C showing mean shifts and standard deviations.

The final example presented in this chapter is an *in vitro* tomogram of purified *S. cerevisiae* ribosomes suspended in a thin film of vitreous ice (Bharat and Scheres, 2016). The major difference compared to the previous two examples is the relatively high SNR of individual ribosomes and a very limited overlap with other structures in individual tilts. This was reflected by the very low standard deviation of particle shifts (Figure 2.6, B). It was even possible to see the "misalignment" of some particles in the original aligned tilt series, after they were extracted at their expected 2D coordinates and heavily low-pass filtered (Figure 2.6, E). Comparison of tomogram slices before and after Flexo refinement showed a clear increase in low-resolution content after the procedure. This was confirmed by comparison of ribosome SVA maps before and after Flexo refinement which showed a boost in gold-standard FSC across all frequency shells and a visually "clearer" SVA map (Figure 2.6, D, G, H). Interestingly, was a substantial boost to all resolution shells above, but not at, or below the 0.143 FSC cutoff. This could be interpreted in several ways. Clearly, there was a boost to the low-frequency SNR and it is arguably mainly the low-frequencies that drive alignment in SVA averaging. In a small subset of particles, the alignment precision is reduced due to a low SNR of the reference. A boost to the low-resolution signal, therefore, improves alignment precision. The lack of resolution improvement, despite the increased low-resolution content could feasibly be caused by other factors such as errors in CTF estimation. Alternatively, it could be an artefact of Flexo implementation: The reprojected tomograms are a good approximation of the original data at low, but not high resolution despite reduced low-pass filtering (below 1.5 nm). This could lead to improvement of alignment at higher tilts, but relative alignment deterioration at low tilts where warping

is not as pronounced. The low-resolution, but not high-resolution boost in the SVA map of the whole dataset would support this conclusion. Furthermore, the aligned tilt series generated by Flexo uses the original aligned tilt series as input. This means that the final data has been interpolated multiple times which could feasibly affect the resolution in SVA. In all likelihood, both of these factors play a role and have to be addressed before Flexo can be released for public use.

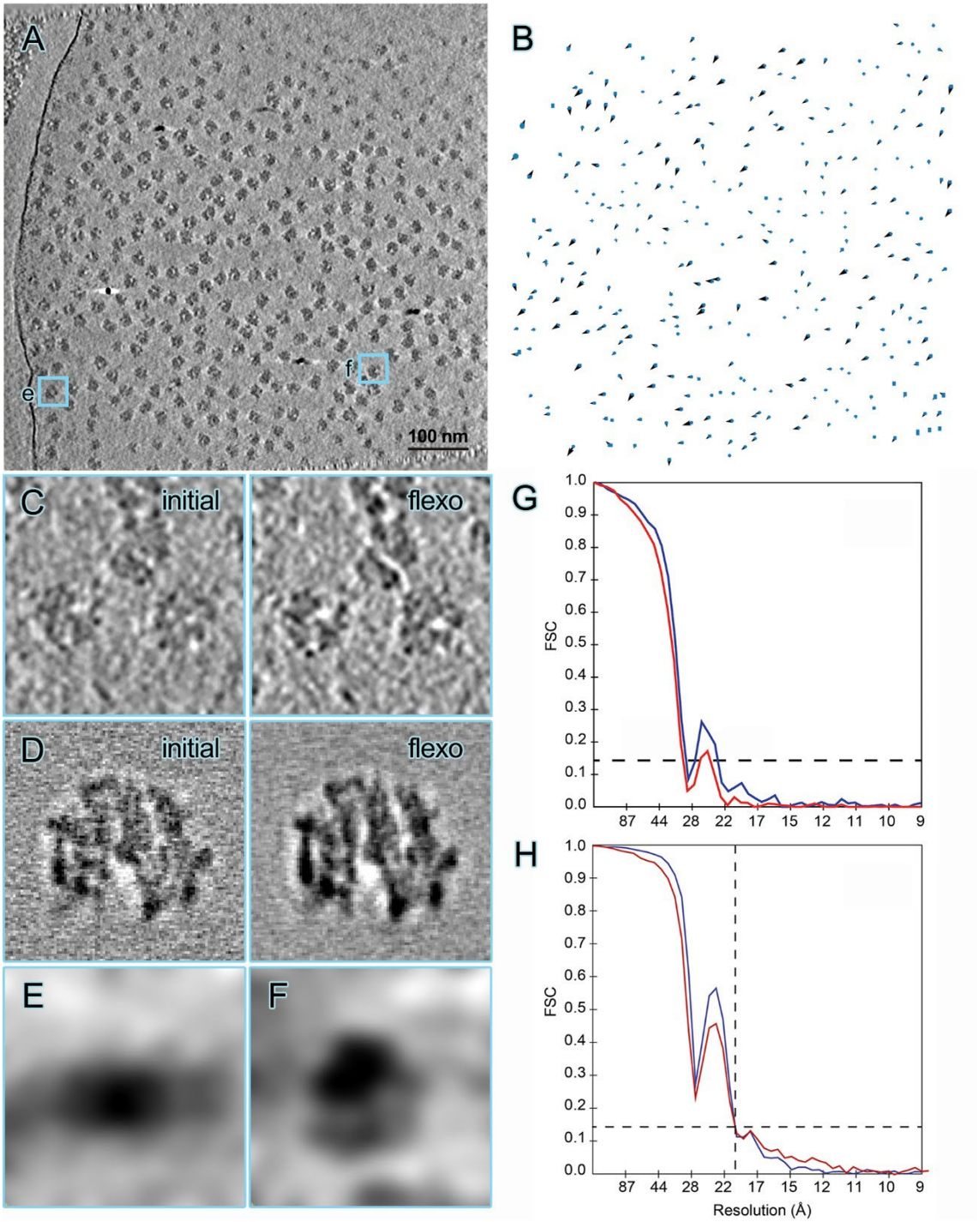


Figure 2.6 Accurate shift measurement was achieved with an *in vitro* ribosome data set. (**A**) A slice through the Flexo-refined tomogram. (**B**) Mean shifts and standard deviations of individual particles. Please refer to Figure 2.4, C for details. (**C**) Magnified tomogram slices of initial and Flexo-refined tomogram indicating a substantial increase in low-resolution content. (**D**) Slices through SVA maps of ~ 2400 particles before and after Flexo refinement. Cyan boxes marked with (e) and (f) in (A) indicate position of particles shown in (**E**) and (**F**). Projection images of these particles were extracted from the original aligned tilt series, filtered and averaged in order to indicate that some parts of the tomogram undergo larger translations than others. The average image in (E) shows a horizontally smeared density corresponding to the ribosome moving from side to side. Projections of the particle shown in (F) were centred on their expected position, resulting in a sharper average image. (**G**) Gold-standard FSC between SVA half-maps of ~ 200 particles. The corresponding gold-standard FSC is shown in (**H**).

Future development

The potential benefit of using Flexo to refine tomographic alignment was demonstrated using three different tomograms. However, the contributions of some steps, such as the use of a masked and reprojected tomogram as opposed to the raw data was not evaluated. A set of simulated tomograms was generated towards this end by adding increasing amounts of Gaussian noise to a volume containing backplotted ribosome maps. These volumes were reprojected into tilt series and reconstructed. Warping was simulated by an increasing whole image magnification of higher tilts, and changes to tilt angles. Performance of Flexo on these data is yet to be fully evaluated.

Ribosomes were used as "Flexo fiducial markers" in all three cases; they are one of the few densities that can be reliably identified in noisy cellular tomograms and are usually represented in sufficient numbers to enable localised reconstructions. Other structures with isotropic dimensions, such as virus capsids, could be used, provided they are also sufficiently homogeneous for sub-volume averaging. Filamentous densities, such as F-actin or DNA strands are often clearly visible in individual tilts of tomographic data and their use for unwarping would be of clear benefit. Implementation of this feature would require anisotropic weighting of the calculated shifts, as it is more likely that translations parallel to the filament are a result of noise correlation compared to perpendicular shifts.

A boost in the SNR of individual projection images would lead to an overall improvement in shift estimation. Omitting possible improvements due to progress in EM hardware, it might be possible to achieve a SNR increase by grouping several tilts together. An initial alignment between these can be performed using either an SVA reference, or simply by

tilt to tilt translation search as the geometric changes due to tilting are small in neighbouring views. Furthermore, CTF convolution should be applied to each particle in order to make it more similar to the raw data. More sophisticated density subtraction is needed for robust computational unwarping. Initial testing performed with masktomrec (Fernandez *et al.*, 2016) showed promise as this allowed the original tilts to be used; these have much fewer tomographic artefacts compared to masked and reprojected tomograms. However, initial testing of this concept with simulated tomograms resulted in significant shifts being reported by Flexo, where zero shifts were expected. The use of a masked and reprojected tomogram correctly returned zero average shifts. An error in implementation is the most likely explanation for this observation, but it is possible that the use of masktomrec is not adequate for this application.

It is possible to see clearly the expansion of membrane vesicles in some aligned tilt series, similar to the ribosome example in Figure 2.6, E. It would be interesting to explore whether it would be possible to allow users to "draw" the direction of warping and use this information for shift refinement. It is unlikely that such large translations would be detected by Flexo, as the best results were obtained by limiting the maximum allowed shift. A step forward would be the implementation of multiple iterations. Making use of the simplistic example outlined (Figure 2.3), relative translation between particles can only be corrected to within the mean of the original warping. Making use of multiple iterations might result in further improvement relative to a single step refinement. Testing an initial implementation of iterative alignment resulted in alignment improvement after the first iteration, but subsequent iterations produced increasingly worse tomograms. Similar to testing of density subtraction with

masktomrec, poor implementation was the likely cause, and more work remains to be done in this direction.

There are several avenues that should be explored in order to make Flexo a more robust program for tomogram unwarping. Extensive documentation together with code annotation will follow in order to allow changes and improvements to be performed by the scientific community. The ultimate aim is to achieve good integration with IMOD and PEET, which could make Flexo a standard part of tomographic reconstruction. Contact and discussion with David Mastronarde (developer of IMOD package) on this has been established.

2.3 Materials and methods

Data acquisition

Tilt series of the cellular periphery was acquired using Tecnai F30 with a post-column BioQUANTUM energy filter (Gatan) operated in Zero-Loss mode using 20 eV energy slit and K2 Summit direct electron detector operating in counting mode (Gatan). A 70 µm C2 aperture was in place during brightfield data acquisition. Tilt series was collected bi-directionally from 20° to -40° and 23° to 53° in 3° increments at 3.41 Å pixel size, 4 µm defocus and 2.3 $e^{-}Å^{-2}$ per tilt. Tilt series of the nuclear periphery was acquired by Michael Grange and Christoph Hagen using Tecnai F30 "Polara" with a post-column BioQuantum energy filter operated in Zero-Loss mode using 20 eV energy slit and K2 Summit direct electron detector operating in counting mode (Gatan). Tilt series was collected bi-directionally from 13° to 61° and 10° to -62° at 3° increments, -7 µm defocus, 3.5 Å pixel size and 4.8 $e^{-}Å^{-2}$ per tilt.

Software packages and libraries

Step	Process	Source
	SVA	PEET, DV, TEMpy, Chimera
a	3D low-pass filter	Scipy, Numpy, CP
	Dilation	Scipy
	Masking	Numpy
a'	Volume backplotting	DV, TEMpy
b, b', b''	Reprojection	tilt (IMOD)
c	Particle extraction	Numpy
	Fourier cross correlation	DV, Scipy, Numpy
d	Fiducial model refinement	tiltalign (IMOD)
e	Tilt series alignment	newstack (IMOD)
f	Tomogram reconstruction	tilt (IMOD)
	Parallel computation	Joblib

IMOD	(Kremer *et al.*, 1996)
Numpy	(Walt *et al.*, 2011)
Scipy	(Jones, 2001)
TEMpy	(Farabella *et al.*, 2015)
Joblib	(Joblib)

Table 2 Source of libraries used for Flexo. Steps refer to arrows in figure 2.2. CP = Christoph Pratsch, DV = Daven Vasishtan

Chapter 3 Cryo-SOFI: A general solution to cryogenic super-resolution imaging

3.1 Introduction

Fluorescence imaging

Correlative light and electron microscopy (CLEM) combines the labelling specificity of fluorescence light microscopy (FM) and the high-resolution of electron microscopy (EM). This method is routinely applied to plastic embedded specimens, where localisation of fluorescently labelled proteins can provide necessary context for observations of chemically stained structures (Figure 3.1, left panel). Chemical fixation and heavy-metal staining lead to disruptions of biological structures (Figure 3.1, right panel), highlighting the need to perform CLEM at cryogenic conditions (cryo-CLEM) in order to preserve specimens at near-native conditions.

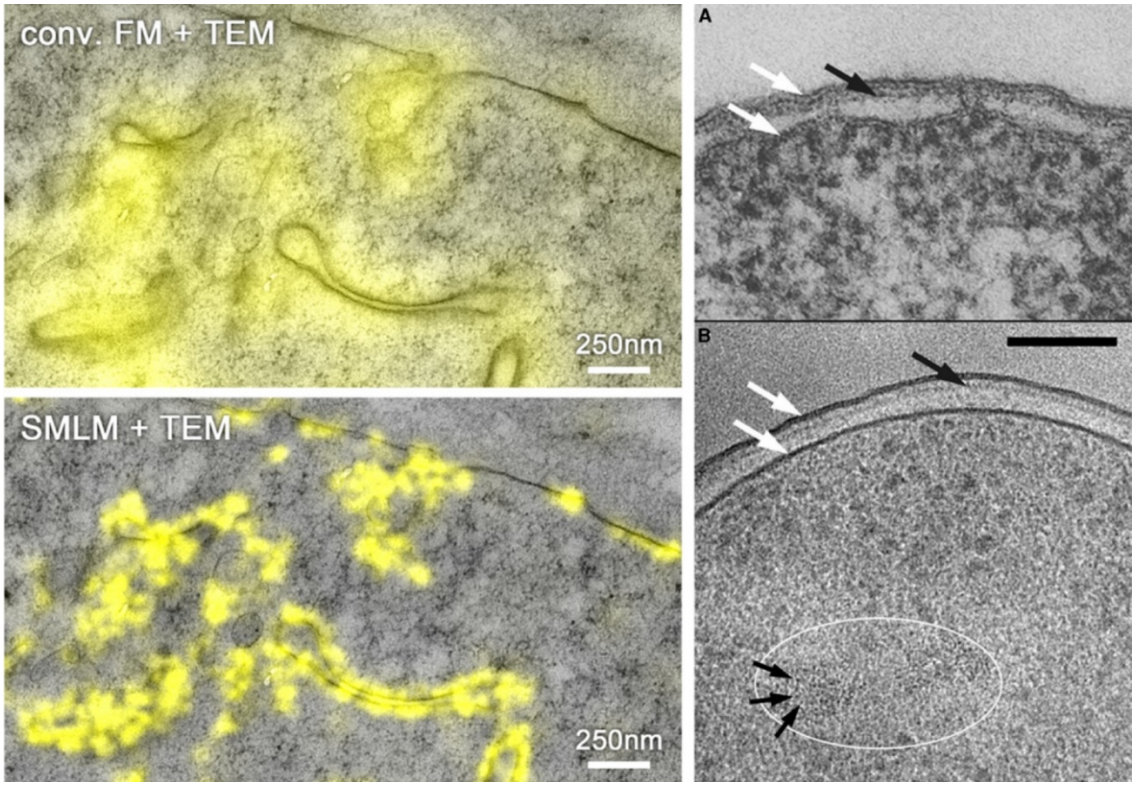


Figure 3.1 Conventional and cryo-CLEM. Left panel shows conventional FM and super-resolution FM images overlaid with EM images of resin embedded HEK293T cells expressing ephrin A2 fused to mVenus fluorescent protein. Ephrins are cell guidance molecules (Seiradake *et al.*, 2010) that are used as cell entry receptor by henipaviruses, an emerging group of human pathogens. Reproduced with permission from Ando *et al.* (2018), originally published in (Johnson *et al.*, 2015). Right panel shows the difference between a *Pseudomonas aeruginosa* cell embedded in resin (**A**) and imaged under cryogenic conditions after vitrification by high-pressure freezing (**B**). White arrows indicate inner and outer membranes, black arrow indicates peptidoglycan cell wall. White ellipse in (**B**) encircles the location of nucleolus and small back arrows point towards back dots resulting from imaging the chromosomal DNA edge-on. Reproduced with permission from Al-Amoudi *et al.* (2004). The original data was published by Beveridge (1999) and Matias *et al.* (2003).

However, cryo-CLEM comes with several considerable challenges that make it a niche, low-throughput technique requiring a substantial level of time investment and expertise (Jun *et al.*, 2019). Similar to other technically demanding cryogenic techniques (Al-Amoudi *et al.*, 2004), the probability of obtaining positive results *p* can be expressed as the product of the probabilities of successfully completing each individual step, and the frequency with which the biological process of interest can be observed:

$$p = GIVEUPNOW \quad (9)$$

where *G* is the probability of growing cells on EM grids, *I* cryo-LM imaging, *V* vitrification, *E* transfer to EM, *U* transfer to cryo-LM, *P* observing the biological process of interest in undamaged cells, *N* fraction of undamaged grid area, *O* fraction of cells that are vitreous, and *W* correlation of fluorescent signal with EM position for acquisition. This chapter will focus mainly on factors contributing to the value of *I*: imaging biological specimens, primarily cells at cryogenic temperatures.

Bridging the resolution gap

Figure 3.1 (left) illustrates that while conventional light microscopy is sufficient to infer the presence of a certain molecule in a specimen, a much higher resolution is needed to draw conclusions about its location relative to subcellular structures observed in EM. The fundamental resolution limit of an optical system was defined by Ernst Abbe:

$$d = \frac{\lambda}{2NA}, \quad (10)$$

where λ is wavelength, and *NA* (numerical aperture) is the product of the index of refraction of the immersion medium, and $sin\theta$, the maximum collection half-angle of the objective lens (Abbe, 1873). Super-resolution methods (with the exception of structured illumination microscopy) make it possible to narrow the effective point spread function (PSF) by either photo-physical (stimulated emission depletion microscopy, STED) or statistical means (single-molecule localisation microscopy, SMLM) with the assumption that the fluorescent signal originates from a single point (Hell, 2009). In the latter case the error in localisation Δx decreases proportionally with the number of collected photons N_{coll}:

$$\Delta x \geq \frac{s}{\sqrt{N_{coll}}} \qquad (11)$$

where *s* is the spatial standard deviation of the PSF (Deschout *et al.*, 2014, Vangindertael *et al.*, 2018). It is, therefore, theoretically possible to achieve nanometre-precision localisation even with low-NA instruments. This is particularly appealing for cryo-LM due to technical limitations on lenses at cryogenic temperatures.

Light microscopy at cryogenic temperatures: technical challenges

Arguably the largest unsolved technical limitation of cryo-CLEM is keeping specimens cooled close to the temperature of liquid nitrogen (~ -196° C or ~ 78 K) during FM imaging. Heating of specimens above ~ -135° C results in devitrification: the transition from amorphous to crystalline ice, which damages biological structures and causes a loss of contrast in EM due to the appearance of Bragg reflections. In contrast, the

microscope optical elements, such as the objective, have to be kept close to room temperature (RT) to avoid structural damage and changes in optical properties. Most cryo-CLEM setups therefore make use of long-distance air objectives with NA ≤ 0.9. The reduction in NA compared to RT oil-immersion objectives (NA = 1.4) results in a lower resolution of conventional images, but it also results in a substantial drop in the amount of collected light (between 30 and 60%) (Weisenburger *et al.*, 2014, Wolff *et al.*, 2016). Cryogenic immersion objectives do exist, but their use is still experimental (Nahmani *et al.*, 2017). High NA also exacerbates aberrations brought about by an asymmetric PSF stemming from the arrested spatial orientation of fluorophores (Gould *et al.*, 2008), which leads to significant aberrations in FM images. This and other photo-physical properties have to be considered when designing high-resolution cryo-LM instruments and methodologies.

Fluorescence at cryogenic temperatures

The photo-physical properties of a fluorescence emitter change with the ambient temperature. This is exacerbated at cryogenic temperatures due to the transition from liquid to solid state, which limits, for example, the diffusion of reactive oxygen species that have a major impact on molecule photo-stability. Photo-bleaching decreases by several orders of magnitude as the ambient temperature approaches 0 K (Weisenburger *et al.*, 2014). Together with long-lived bright and dark states (i.e. slower blinking), it is possible to achieve sub-nanometre localisation precision of fluorescent dyes at cryogenic conditions, since photo-bleaching is one of the main resolution-limiting factors at RT. The longer-lived on and off states also make it easier to identify individual

blinking events in densely labelled environments like cells. Conversely, reduced bleaching decreases the signal-to-noise ratio (SNR) in cellular specimens due to longer-lived auto-fluorescent signal (Kaufmann *et al.*, 2014), and an increase in phosphorescence resulting from a higher occupancy of the triplet state (Giske, 2007, Kaufmann *et al.*, 2014). Furthermore, super-resolution methods generally rely on high-intensity excitation light in order to reduce the volume of fluorescence emitting molecules (STED) or to drive fluorophores to either bright or dark state in single-molecule localisation microscopy (SMLM). This results in specimens warming up, primarily through absorption of the specimen and the support film. The intensity of excitation light therefore becomes the main factor limiting resolution in cryo-CLEM due to the requirement to maintain specimens below devitrification temperature for subsequent EM imaging (Chang *et al.*, 2014, Wolff *et al.*, 2016, Tuijtel *et al.*, 2019). Higher temperatures result in the transition from amorphous to cubic and eventually hexagonal forms of ice; particularly high laser intensities can even lead direct sublimation.

Low-intensity super-resolution imaging

There are two methods that can achieve super-resolution with sufficiently low excitation intensities to prevent devitrification: super-resolution optical fluctuation imaging (SOFI) and structured illumination microscopy (SIM). The latter is limited to 2-fold increase in resolution, but its fast acquisition rate and the possibility of easily extending the concept in the axial direction enables the generation of 3D data. SOFI is similar to SMLM in that it makes use of stochastic fluctuation of fluorophore emission, but it can extract

super-resolution information from data where it is not possible to identify individual blinking events. This is achieved by looking at the correlation of each pixel's intensity fluctuation over time. Assuming that neighbouring molecules do not impact each other's fluorescence (apart from Förster resonance energy transfer), a high level of fluctuation correlation indicates that the fluorescent signal originated from the same molecule. The correlation function of the n^{th} order contains the PSF taken to the n^{th} power. By plotting the amplitude of the correlation function, it is possible to reconstruct an image with $\sqrt{n}$ improvement in resolution.

Cryo-SOFI, a collaborative effort

This chapter presents the application of the SOFI principle to imaging cryogenic specimens (dubbed cryo-SOFI) with an intent to develop a widely applicable super-resolution technique for cryo-CLEM. The SOFI method was modified for cryo-FM by Felipe Moser and Rainer Kaufmann (RK) to account for thermal drift and asymmetrical PSF of cryogenic specimens (Moser *et al.*, 2019). Cryo-FM data was collected by RK. Specimen preparation, EM data acquisition and processing was done by VP. These data were published (Moser *et al.*, 2019) with additional contribution from Valerie Mordhorst, Débora Andrade, Lindsay Baker, Christoph Hagen and Kay Grünewald.

3.2 Results

Two different subcellular structures of mammalian cells, actin or mitochondria were labelled (by Dendra2-Lifeact and mClover-TOMM20, respectively) and used as model systems to validate the general applicability of cryo-SOFI. XC cells expressing Dendra2-Lifeact contained a network of fluorescent filaments on top of diffuse cytoplasmic fluorescent signal. Cryo-LM data collection was targeted to long pseudopod-like structures which were thinner than cell bodies, making them more suitable for EM (Figure 3.2, A and G).

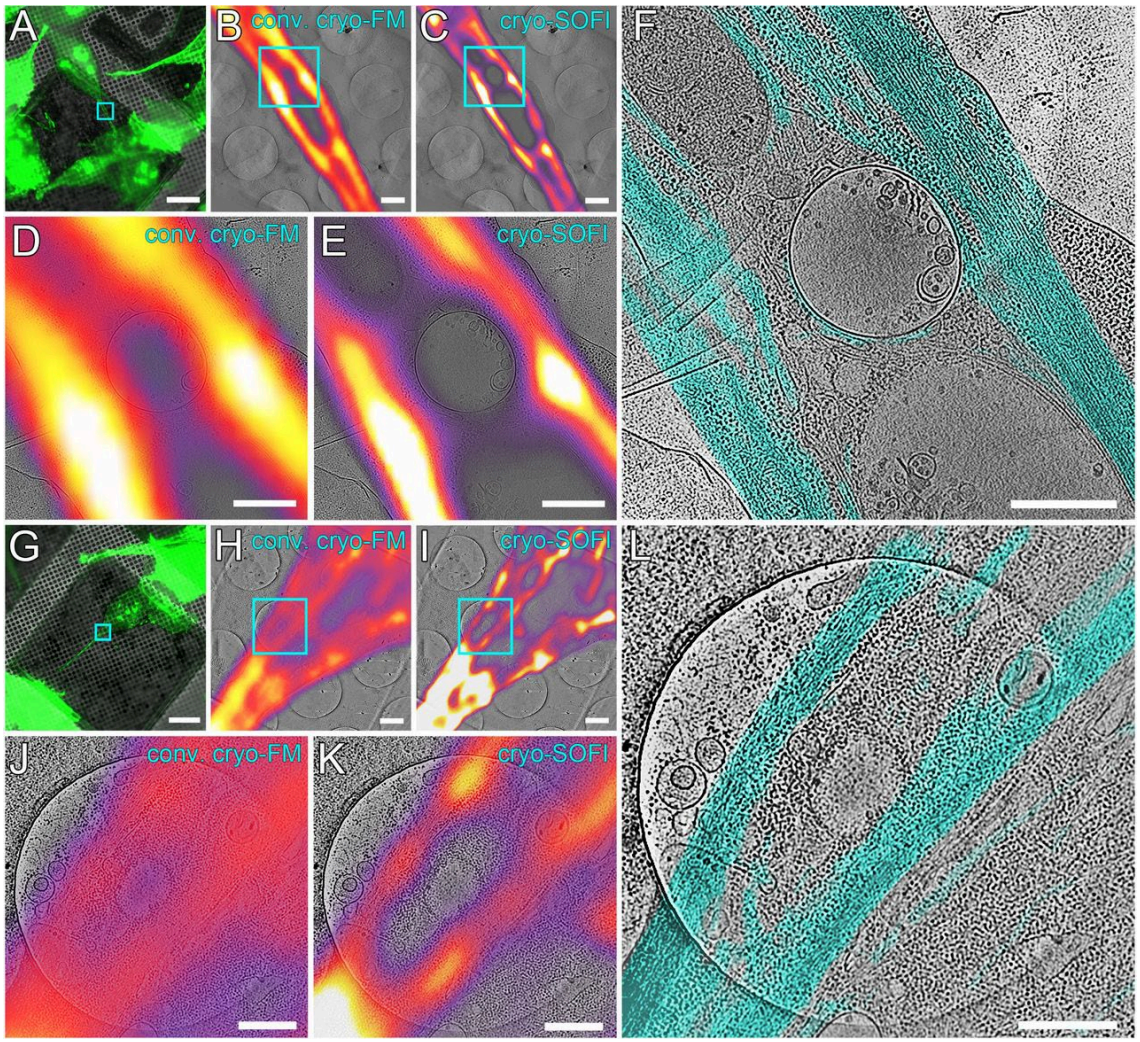


Figure 3.2 Cryo-SOFI improves resolution of Dendra2-Lifeact labelled actin filaments. Pseudopods of two XC cells stably expressing Dendra2-Lifeact were imaged in cryo-FM and processed by cryo-SOFI (**A-E** and **G-K**). (**A, G**) An overview of grid squares showing the morphology and fluorescence distribution of imaged cells; areas shown in **B**, **C** and **H**, **I** are highlighted with cyan squares (scale bars 20 µm**).** (**D, E; J, K**) Magnified areas from **B**, **C** and **H**, **I** are shown to compare conventional cryo-FM and cryo-SOFI images (scale bars 1 µm). (**F, L**) Medium magnification electron cryo-tomograms (nominal 9300x) were subsequently acquired at the same areas. Actin bundles were manually segmented in 3D and the projections of the segmented volumes (cyan) were projected on 23 nm thick tomogram slices. In both cases the cryo-SOFI image matches the segmented volumes better than the conventional image and the signal is excluded from vesicles and mitochondria to a greater extent.

Cryo-SOFI substantially improved the localisation of LM signal to areas not occupied by large vesicles and mitochondria (Figure 3.3, E and K). The large pixel size (23 Å) of the tomography data set did not permit a completely unambiguous segmentation of actin densities, but manual segmentation was possible due to the characteristic spacing of actin filaments within bundles; cortical actin on the sides of the pseudopod was clearly distinguishable (Figure 3.3).

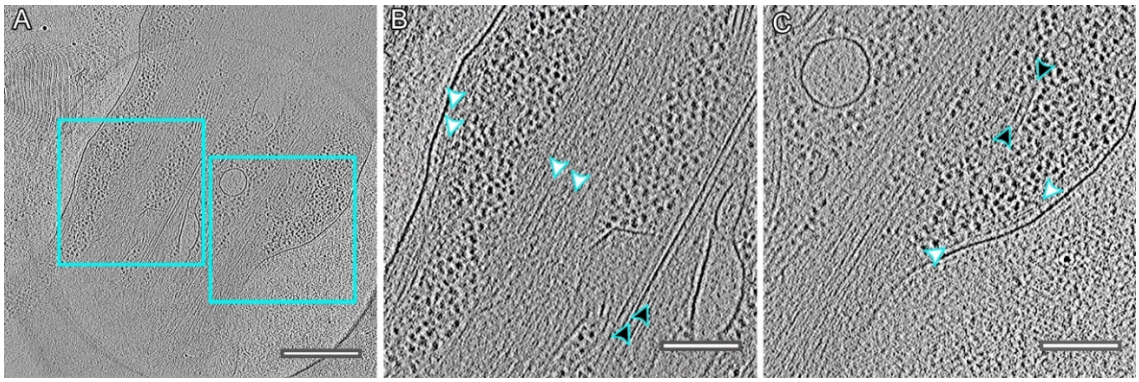


Figure 3.3 Actin filament distribution in pseudopods of XC cells. (**A**) A subsection of tomogram shown in Figure 3.2, B with reduced band-pass filtering; cyan squares indicate the position of sections magnified in (B) and (C) (scale bar 500 nm). (**B, C**) The characteristic periodicity of actin that is apparent at higher magnification tomograms, comes from pairs of neighbouring monomers which have a helical raise ~ 4.6 nm. This periodicity cannot be discerned in these tomograms, as 4.6 nm is the Nyquist frequency of the raw data. However, it was possible to identify actin bundles due to the spacing of parallel filaments which is ~ 9 nm (white arrowheads). They are easily distinguished from microtubules which have denser walls and a defined thickness (black arrowheads, scale bars 200 nm).

Mitochondrial membranes of XC cells were labelled with mClover-TOMM20 (a mitochondrial outer membrane translocase) by transient transfection. There was a clear improvement in resolution after cryo-SOFI processing which resulted in a better correlation with projections of mitochondrial membranes observed in cryo-EM (Figure 3.4). Comparing cryo-SOFI and conventional cryo-FM indicated that some mitochondria contained very weak or no associated fluorescent signal relative to other mitochondria (Figure 3.5).

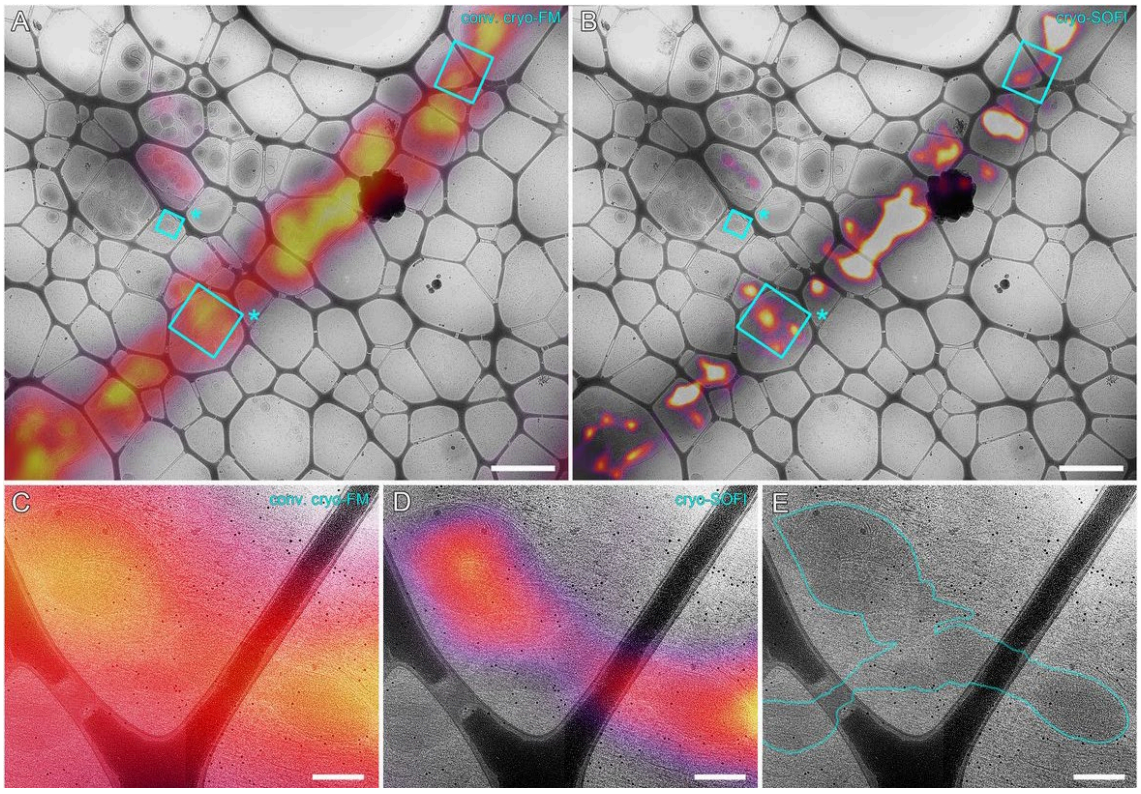


Figure 3.4 Cryo-SOFI restricts fluorescence to areas occupied by mitochondria in XC cells. (**A, B**) Comparison of conventional cryo-FM and cryo-SOFI images overlaid with cryo-EM montage of the corresponding area (scale bar 2 µm). Square in the top-right corner indicates the position of areas magnified in (**C**)-(**E**). (**E**) Same area as (C), (D); projections of outer mitochondrial membranes were manually traced (cyan) to indicate their position (scale bar 500 nm). Cyan squares marked with an asterisk indicate the position of areas magnified in Figure 3.6, B, C and D.

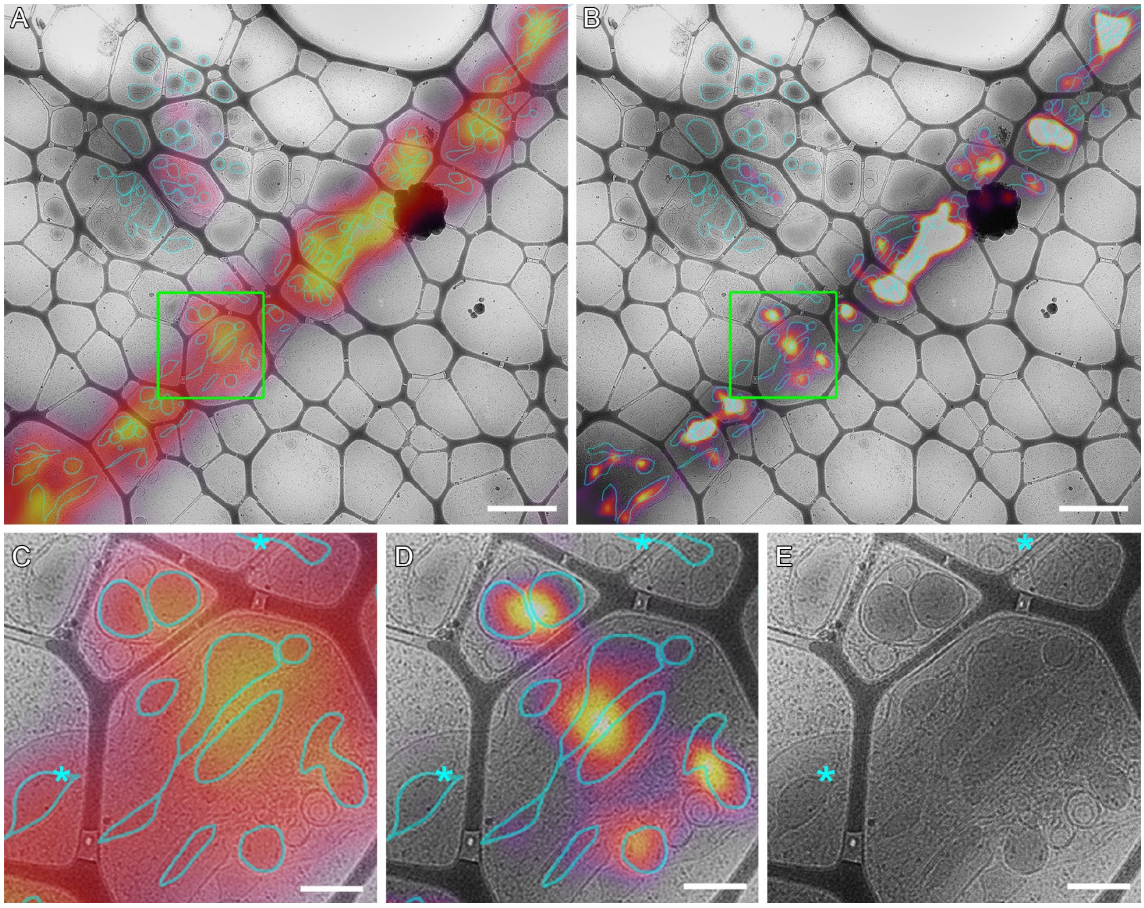


Figure 3.5 Uneven distribution of mClover-TOMM20 among mitochondria of XC cells. All mitochondria discernible in EM montage (same as Figure 3.5) were outlined in cyan. Mitochondria could be distinguished from other membranous structures due to a denser matrix, presence of cristae and calcium phosphate crystals (see figure 3.6, B for a higher-magnification image). (**A, B**) A comparison of conventional cryo-FM and cryo-SOFI. An aggregate of cellular debris can be seen adjacent to a pseudopodium (scale bars 2 µm). It contained a large number of mitochondria, presumably in various stages of decay, with lower or no fluorescence compared to the pseudopodium. Green square indicates area magnified in C-E. (**C-E**) Several mitochondria (marked with an asterisk) contain no cryo-SOFI signal where the conventional cryo-FM image indicated the contrary (scale bars 500 nm).

Preservation of a specimen's vitreous state is the minimum necessary requirement for correlative cryo-FM imaging. There was no evidence of devitrification caused by cryo-SOFI data acquisition in any of the imaged areas (Figure 3.6). The laser intensity was restricted to 100 W cm^{-2}, an empirically determined safe level. The illumination beam was restricted to approximately 40 µm diameter in order to further reduce energy deposition to the specimen. In most cases, it is the flatness of a specimen (or the lack of thereof) combined with the depth of focus, rather than the beam diameter, that limits the observable area. The "critical dose", i.e. dose which leads to the transition from

amorphous ice to crystalline ice, depends on the thickness and composition of the support film, specimen thickness and composition, and proximity to the gold support bars. Increasing the illumination intensity to 200 W cm^{-2} resulted in substantial thinning of the specimen, presumably due to sublimation (Figure 3.7). Small ice crystals could be observed in a ~ 25 µm radius from the illuminated area, however, a thin layer of amorphous material remained suspended over holes in the carbon support film. It was hypothesized that this was an amorphous protein residue as the specimen contained 10 % foetal bovine serum. The material was prone to breakage under EM illumination in contrast to the "melting" or "receding" behaviour of ice at high electron fluxes.

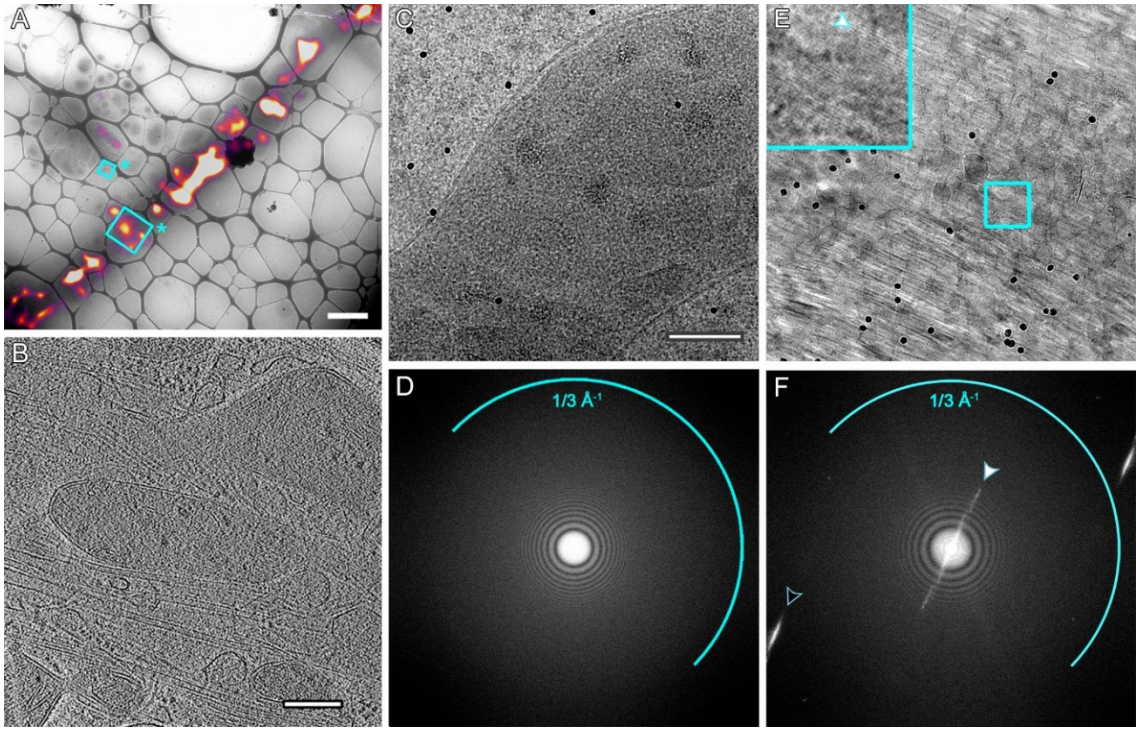


Figure 3.6 Areas imaged for cryo-SOFI remained vitreous. (**A**) Overview of areas shown in (B, bottom square) and (C, top square, scale bar 2 µm). (**B**) A slice through tomogram acquired at 4.2 Å pixel size showing mitochondria and microtubules (scale bar 200 nm). (**C, D**) Projection image acquired with 1.4 Å pixel size and 75 $e^{-}A^{-2}$, and its power spectrum showing no evidence of devitrification (scale bar 100 nm). (**E, F**) Projection image (with the same acquisition parameters as C) and power spectrum of an area containing crystalline ice that was acquired at a different location of the same grid. The presence of crystalline ice is readily noticeable at medium to high magnification (≥ 4,000) as black-and-white Moiré patterns in real-space and high-contrast spots and lines on power spectra. Inset shows a detail of lattice lines with ≈ 8.1 Å spacing and the corresponding reflections in (**F**) at 7.6^{-1}-11^{-1} $Å^{-1}$ are indicated with white arrowhead. A peak at 2.4^{-1}-2.7^{-1} A^{-1} could be observed (black arrowhead) indicating the presence of a finer lattice spacing in the image. It is possible that this peak is offset from its correct position due to aliasing.

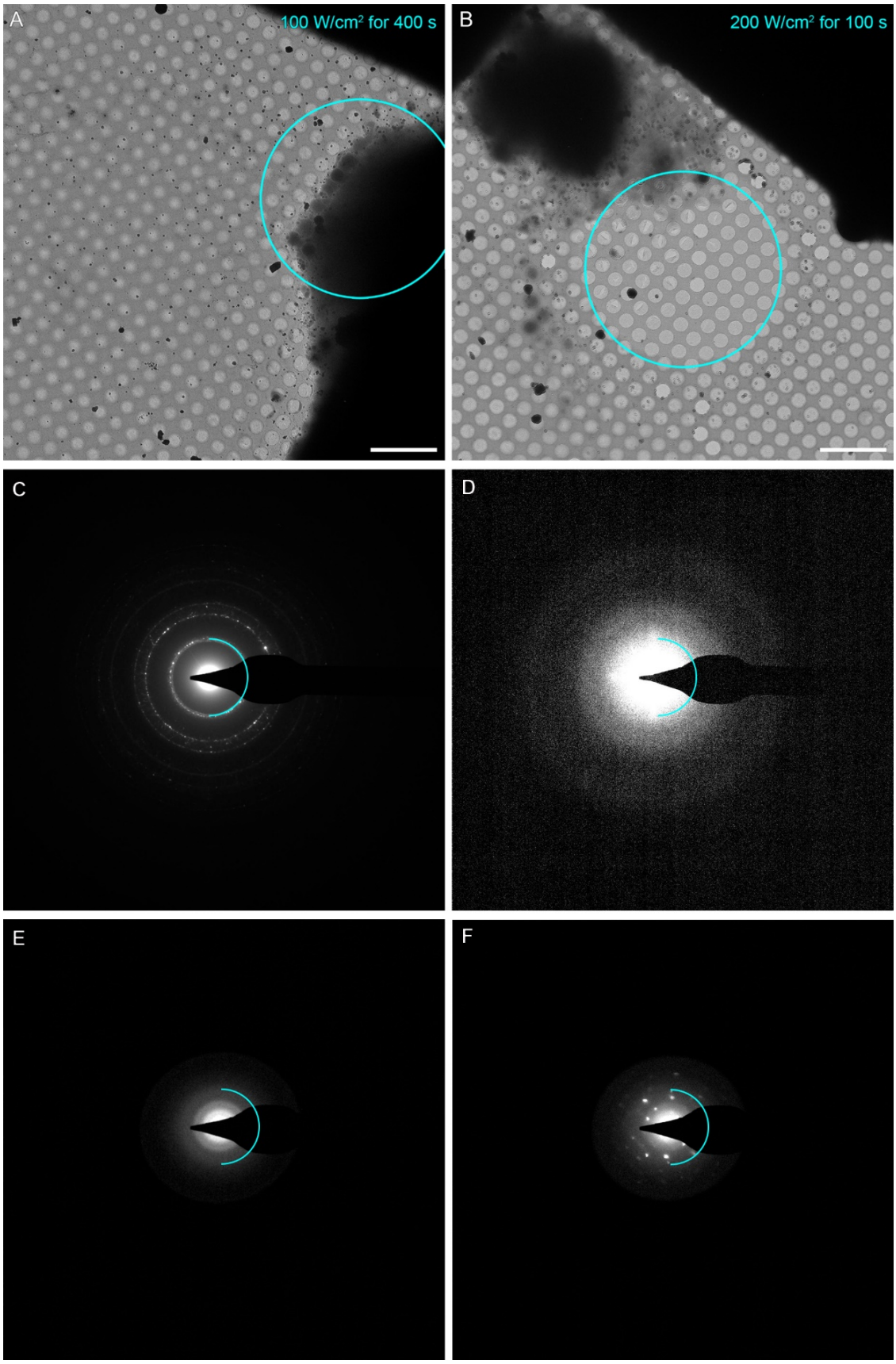

A
100 W/cm² for 400 s
B
200 W/cm² for 100 s
C
D
E
F

Figure 3.7 Laser-induced specimen damage. Areas illuminated with 100 Wcm^{-2} for 400 s (**A**) or 200 Wcm^{-2} for 100 s (**B**) are indicated in cyan (scale bar 10 µm). While there was no discernible damage in (A), (B) shows substantial thinning of the illuminated area and deposition of material in the surrounding area. This indicates that the threshold for inducing specimen damage is between 100 and 200 Wcm^{-2} and it does not depend on the total energy supplied but on the dose rate. The exact threshold will depend on a multitude of parameters such as composition and thickness of specimen and support film, photo-physics of fluorophores (e.g. Stokes-shift) and proximity to gold support bars. A layer of material, presumably the dehydrated contents of cell medium (DMEM + 10% foetal calf serum), remained suspended over holes in (B). (**C, D**) diffraction images acquired after performing the same experiment as (A, B) on a grid containing DMEM supplemented with 10% FBS but no cells. (D) was acquired over a hole of a laser-thinned area while (C) was acquired outside the illuminated circle. Due to a high sensitivity of the residual material, the electron fluence used to acquire (D) was reduced to ~ 2.5 $e^{-}A^{-2}$ from ~ 30 $e^{-}A^{-2}$ in (C). Diffraction patterns of amorphous ice (**E**) and hexagonal ice (**F**) are shown for comparison. Cyan half-circle indicates approximately 3.7^{-1} $Å^{-1}$.

3.3 Discussion

High-resolution comes at the cost of vitrification

Fluorescence microscopy imaging at cryogenic temperatures has many advantages over room temperature experiments. Movement of large macromolecular complexes is restricted, and fluorophore photo-stability is substantially increased allowing more photons to be collected from each individual molecule. These properties can be exploited in order to achieve high localisation precision using super-resolution microscopy techniques (Chang *et al.*, 2014, Liu *et al.*, 2015, Bykov *et al.*, 2016, Wolff *et al.*, 2016). However, the applicability to more complex biological systems and compatibility with other imaging techniques, especially EM (i.e. imaging on EM grids) and FM data acquisition time needs to be taken into account. For example, it was possible to determine single Ångström localisation of individual fluorophores scattered on silica cooled to liquid helium temperature during a 2-hour acquisition time (Weisenburger *et al.*, 2017). Vitrified cells have been imaged with super-resolution SMLM to achieve high localisation precision followed by electron cryo-tomography

(Chang *et al.*, 2014, Liu *et al.*, 2015). However, the former example made use of Formvar support film which does not allow acquisition of high-resolution EM data due to high radiation sensitivity. The latter study employed cryo-protectants, which are not compatible with mammalian cells and tend to increase the specimen's radiation sensitivity.

Cryo-SOFI, a general solution to cryogenic super-resolution FM

The motivation for the development of cryo-SOFI was to achieve super-resolution FM data and to preserve a vitrified state of cellular specimens using a lightly modified commercially available microscope (Figure 3.9). The data presented above show cryo-CLEM experiments of two sub-cellular structures, where the use of cryo-SOFI substantially improved FM resolution without affecting the specimens' vitrified state. It was possible to achieve resolution improvement of 2- to 3-times with 100 s acquisition times (Figure 3.10). The illumination intensity (100 W cm^{-2}) and acquisition time was restricted in order to minimise the likelihood of specimen devitrification. However, it is likely that it is the dose rate, rather than total dose that is the most important factor affecting the specimen temperature (Figure 3.7). This suggests that longer acquisition times could be used (and therefore higher-order SOFI correlation) to achieve higher resolution. More efficient specimen cooling might permit higher laser intensities to be used, but this ultimately relies on a better understanding of the specimens' thermal conductivity and buffering capacity (e.g., thinner compared to thicker specimens). Liu *et al.* (2015) could, reportedly, make use of up to 15 times higher illumination intensities without causing specimen devitrification. This suggested that the carbon support film is

the main contributor of specimen heating. Currently, the only plausible alternative are silicon oxide support films, but silicon-based substrates are generally much less favourable for growth of mammalian cells than Formvar or carbon substrates. Overall, cryo-SOFI is likely the method of choice for super-resolution cryo-FM of whole cells, regardless of the maximum available illumination intensity, due to its excellent performance on densely labelled specimens (Dertinger *et al.*, 2009).

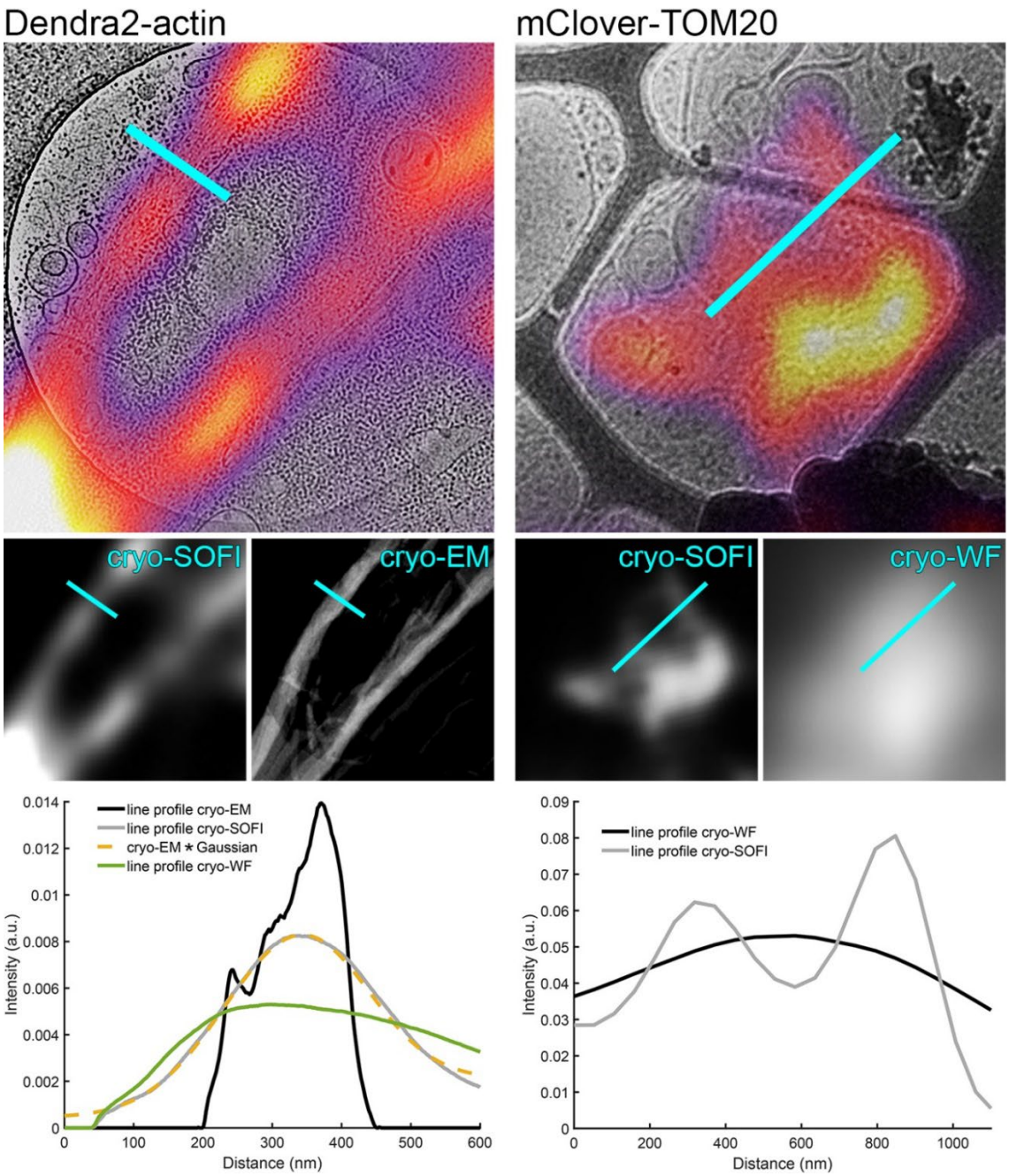


Figure 3.8 Determining resolution improvement of cryo-SOFI. The choice of complex cellular specimens prevented direct quantification of resolution improvement, as this requires the fluorescent structures to be significantly smaller than the wavelength. Nevertheless, the tomographic data can be considered to approach the "ground truth" and was therefore used to model the expected fluorescent signal. The projection of manually segmented actin filaments was multiplied with a Gaussian; full width half maximum of 200 nm matched the cryo-SOFI signal well (3^{rd} order correlation and deconvolution) corresponding to 2-fold improvement in resolution. The left panel shows resolution improvement achieved with fluorescently labelled mitochondria.

Hardware improvements are needed for routine cryo-CLEM

The data presented above are a result of cryo-SOFI imaging performed with the current "state of the art" cryo-FM microscope with minor modifications. However, cryo-FM technology is still in its infancy and substantial technological developments are needed for routine use. Specimen transfer is performed in a liquid nitrogen-cooled chamber that is open to ambient air. This results in the deposition of ice crystals ranging in size from tens of nanometres to several micrometres. While not all areas are obstructed, equation (9) indicates that the addition of even minor inefficiencies impacts the probability of achieving a successful experiment. There are multiple possible solutions to this problem that have been used in other branches of science that make use of extremely low temperatures. For example, displacement of air with dry nitrogen gas or even vacuum are technologically feasible approaches.

Specimen drift is a limitation that can be partially mitigated by drift correction during data processing (Figure 3.9), but this cannot compensate for drift in the axial direction and corresponding changes in focus. SOFI is particularly susceptible to specimen drift as it results in a strong apparent signal fluctuation. Current cryo-FM systems make use of microscope stages converted from RT systems, which are susceptible to thermal drift and mechanical instabilities. An increase in stage stability, or a robust active drift

correction would enable longer data acquisition times and therefore resolution for experiments where very high-resolution is needed.

Cryo-SOFI would benefit heavily from the increase in light collection efficiency of higher NA immersion objectives, making it possible to reach higher resolution with shorter acquisition times. Higher NA exacerbates specimen optical aberrations that can be particularly severe in cryogenic specimens due to large differences in specimen and ice thickness (Wolff *et al.*, 2016). A clear "lensing" effect resulting from spherical aberration can be seen in transmitted light images of thick ice. A possible solution to this problem could be the implementation of adaptive optics that have been successfully used to correct optical aberrations of specimens at RT (Burke *et al.*, 2015). This does require highly sophisticated optical setup, but it may be necessary for projects where resolution is the limiting factor.

Cryogenic specimens are 3D objects and imaging at a single optical plane is not always sufficient to capture the full complexity. While it is true that EM requires very thin (less than 200 nm) specimens to achieve high-resolution, they can no longer be approximated as planar objects in FM as the axial resolution increases. Furthermore, focused ion-beam milling of thicker specimens is becoming increasingly important to study biological processes that only occur, for example, in cell nuclei. There it is needed to achieve accurate axial targeting, which in turns requires high-resolution 3D data. The PSF reduction of cryo-SOFI data extends in all directions meaning that optical sectioning is achieved alongside increased resolution. Simultaneous SOFI imaging at multiple focal planes has been achieved at RT (Geissbuehler *et al.*, 2014) and could be feasibly implemented for cryo-SOFI.

With these improvements it should be possible to achieve high enough FM localisation precision to enable identification of mid-sized (larger than 300 KDa) fluorescently labelled proteins in cET data. Such experiments would be invaluable for validation of a range of in-vitro experimental data, from protein-protein interactions to large-scale structural rearrangements.

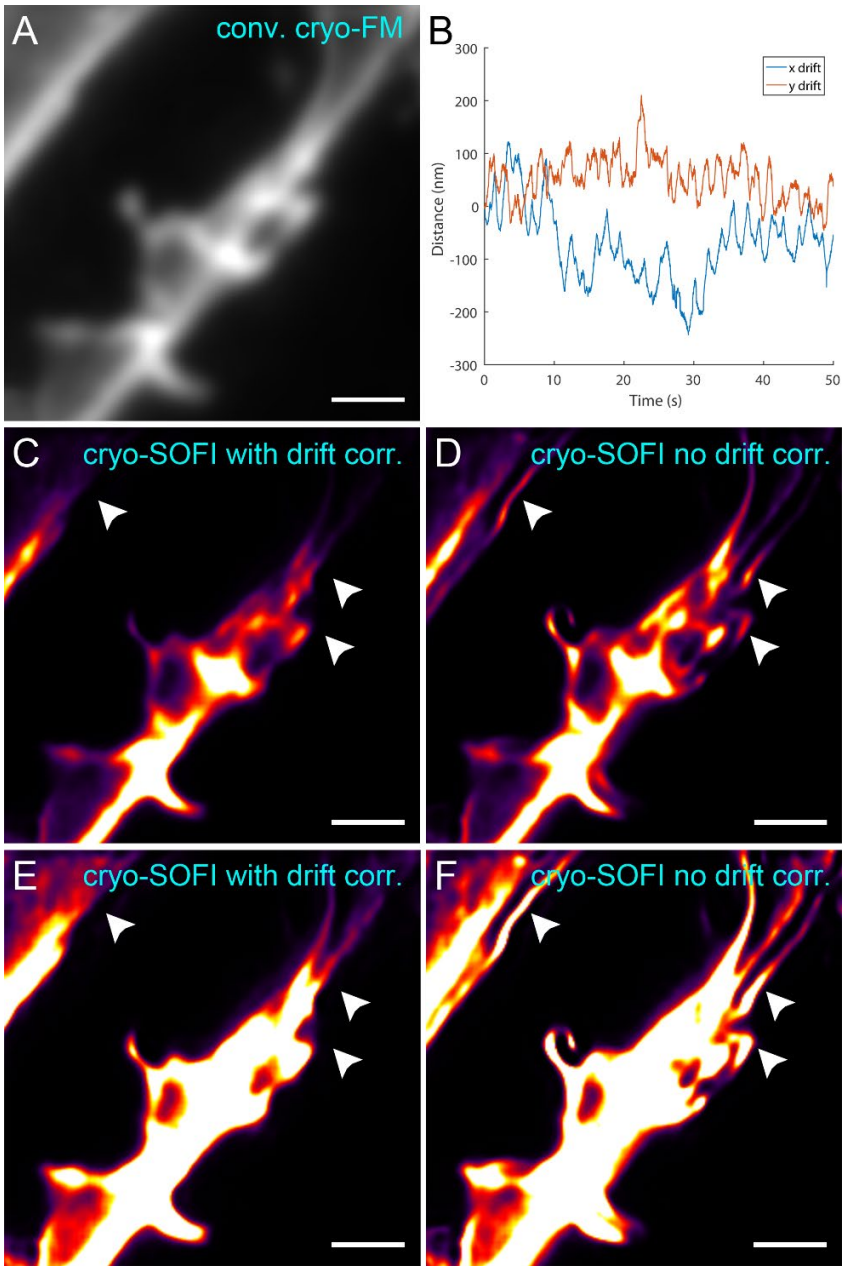


Figure 3.9 Specimen drift causes artefacts in cryo-SOFI data. (**A**) Simple sum of raw cryo-FM data and (**B**) specimen drift measured during post-processing drift correction. **(C)** and **(E)** shows drift-corrected cryo-SOFI data at high and low contour levels; (**D**) and (**F**) shows the equivalent data before correction. Arrowheads indicate artefacts caused by drift-related SOFI autocorrelation.

3.4 Materials and methods

Cell Culture

Cells were propagated in Gibco™ Dulbecco's Modified Eagle's Medium (DMEM) GlutaMAX™ (Thermo Fisher) and 10% foetal calf serum at 37°C and 5% CO_2. Stable cell lines expressing Dendra2-Liefact were generated by transfection with pDendra2-Lifeact-7 (pDendra2-Lifeact-7 was a gift from Michael Davidson, Florida State University, Tallahassee, FL, Addgene plasmid 54694) using X-tremeGENE HP DNA Transfection Reagent (Roche) and selection with 600 µg ml^{-1} G-418 (Sigma). XC cells expressing mClover-TOMM20 were generated by transient transfection in the same manner (mClover-TOMM20-N-10 was a gift from Michael Davidson, Addgene plasmid 56307).

Specimen preparation

EM grids with adherent cells were prepared by deposition of detached cells (0.04% trypsin) on holey or lacey carbon gold-finder (type F1) grids overlaid with graphene oxide (GO) and coated with fibronectin. Holey carbon grids (Quantifoil) were glow-discharged, a layer of GO was deposited by adding an aqueous suspension of GO, blotting and washing with ultrapure water (Bokori-Brown *et al.*, 2016). Subsequent coating with 50 µgml^{-1} fibronectin resulted in GO being washed off (compare Figure 3.10, A and B). While it is possible to improve GO adhesion by ageing (storing grids for several days), a straight-forward step of 1-minute incubation with 4 % paraformaldehyde and washing with ultrapure water resulted in superior adhesion that could be immediately followed

up with fibronectin coating (Figure 3.10, C). Lacey carbon grids with GO (EM resolutions) were used with XC cells expressing mClover-TOMM20 due to their superior hole-to-carbon ratio. Regardless of grid type, cells were incubated for 20-24 h after seeding before they were plunge-frozen.

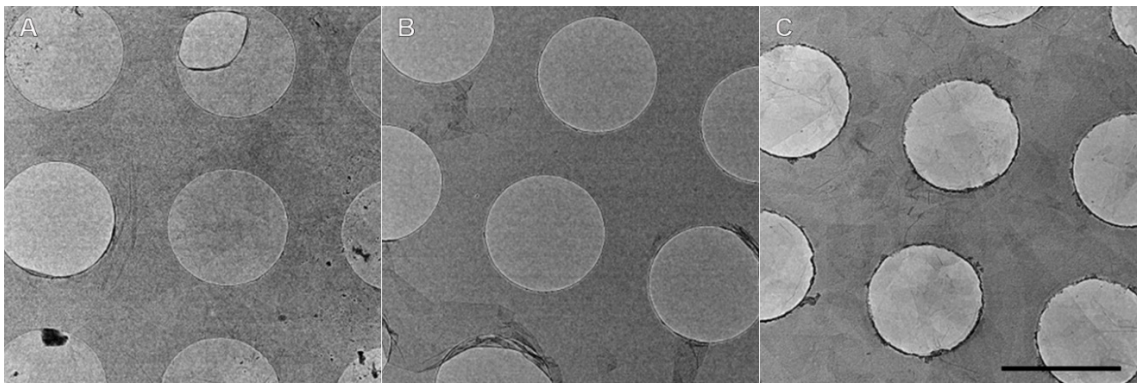


Figure 3.10 Formaldehyde treatment promotes graphene oxide adhesion to amorphous carbon surface. (**A, B**) Holey-carbon grids (C-flats, Protochips) were overlaid with graphene oxide (GO) and imaged at room temperature before (**A**) or after (**B**) coating with fibronectin. (**C**) Incubation with 4% paraformaldehyde resulted in a superior GO coverage after fibronectin coating. Please refer to specimen preparation text above for more details. Scale bar 2 μm.

Electron Microscopy Data Acquisition and data processing

EM imaging was performed using Tecnai F30 "Polara" (FEI) at 300 kV with a post-column QUANTUM 964 energy filter (Gatan) or Titan Krios (Thermo Fisher) with a post-column BioQuantum energy filter, both operated in Zero-Loss mode using 20 eV energy slit and K2 Summit direct electron detector operating in counting mode (Gatan). A 70 μm C2 aperture was in place during brightfield data acquisition but was removed for diffraction measurements. These were acquired on Ceta CCD camera (Thermo Fisher). Where possible, tilt series were collected bi-directionally from 0° to -60° 3° to 60° in 3° increments. Tomogram shown in Figure 3.6, B was acquired with a variable defocus

between -0.5 and -2 µm. Lower magnification tomograms shown in Figures 3.2 and 3.3 were collected after initial focusing to -50 µm. All brightfield data acquisition was performed using SerialEM (Matias *et al.*, 2003), diffraction measurements were acquired using TIA (Thermo Fisher). Tomograms were reconstructed using IMOD Etomo (Kremer *et al.*, 1996).

Cryo-SOFI setup, data acquisition and processing

Cryogenic LM imaging was performed using a modified Cryo-CLEM upright microscope (Leica) equipped with 50x 0.9 NA objective lens (Cryo-CLEM Objective HCX PL APO 50×/0.9; Leica) and DFC365 FX CCD camera (Leica). The microscope was modified by adding a laser illumination source and an electron-multiplying CCD camera (EMCCD, iXon Ultra 897; Andor) with additional 2-times magnification in order to match the magnification (100x) with the camera pixel size (Figure 3.11). Please refer to Moser *et al.* (2019) for further details as the author of this thesis was not involved in cryo-SOFI acquisition and processing; a copy of materials and methods was included in Appendix I.

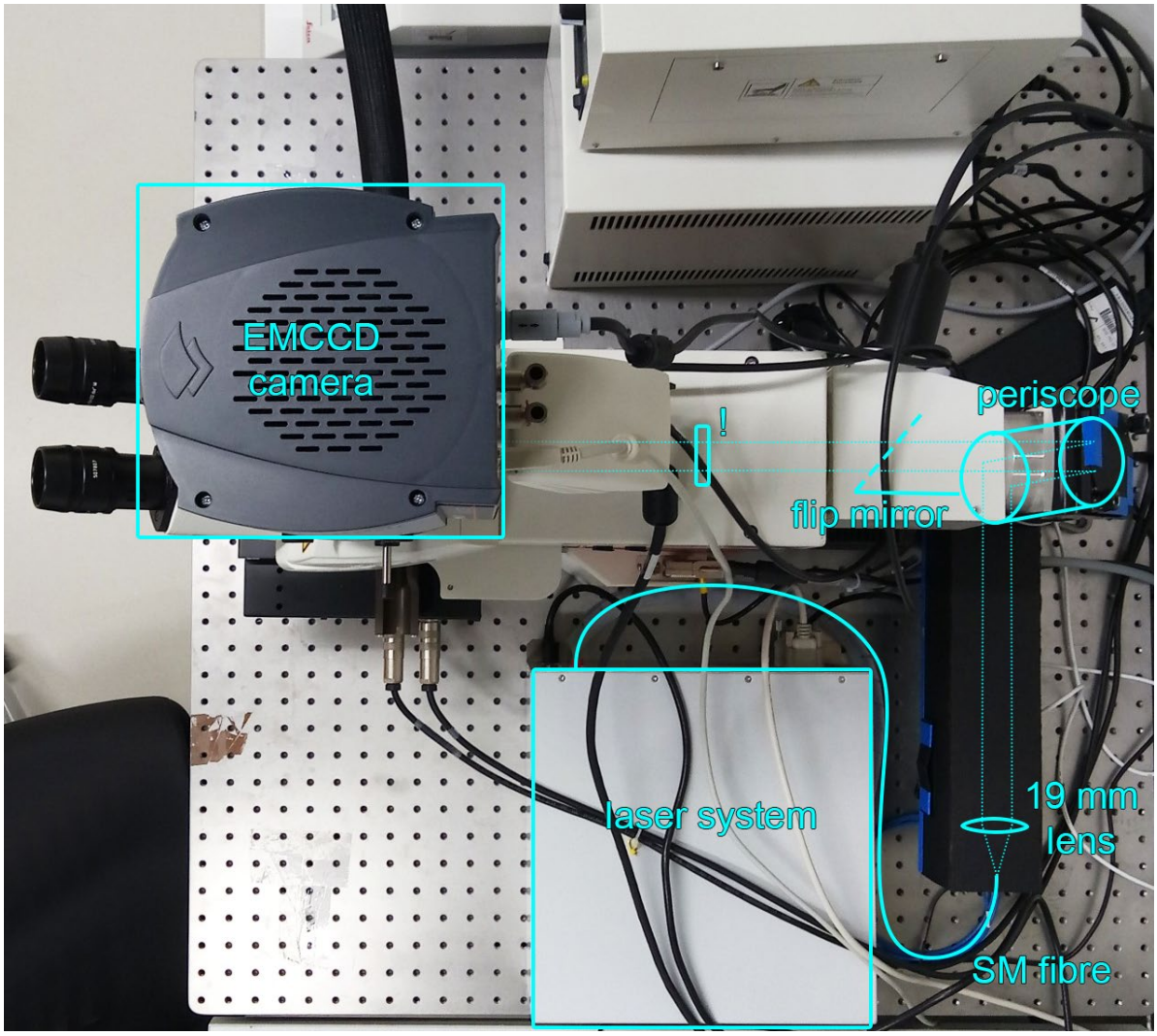


Figure 3.11 Minimal modification of a Leica Cryo-CLEM system was required for cryo-SOFI imaging. Shown is a top-view of the setup with a schematic representation of bespoke modifications: Laser illumination output from a single-mode (SM) fibre was collimated with a 19 mm focal-length achromatic lens in order to restrict the illumination area to 40 µm diameter at the specimen plane. A flip mirror was included to allow switching between laser and mercury lamp illumination. This version of Cryo-CLEM contains a diffuser in the light path that needed to be removed. Finally, a camera with a high detective quantum efficiency was attached to the second camera port.

Chapter 4 How (not) to Catch a Surfing Virus

4.1 Introduction

Virus surfing precedes entry

To establish an infection, viruses must gain entry to the host cell, either by direct fusion with the plasma membrane or through endocytosis. Neither fusion with the plasma membrane, nor endocytosis, occur homogenously across the cell surface. Endocytosis does not occur at the actin-rich cell periphery, but rather at pre-defined centrally located regions often referred to as endocytic hotspots (Nunez *et al.*, 2011) . Virions have been commonly observed in association with dynamic, actin-rich protrusions such as microvilli and filopodia (Helenius *et al.*, 1980, Smith and Helenius, 2004), yet plasma membrane fusion events were not observed in these thin cell membrane extrusions (Lehmann *et al.*, 2005). Microvilli cover the surface of mucosal epithelial cells which are the first point of contact for a variety of pathogens; viruses therefore need to find a way to reach the cell body to achieve cell entry. It is more difficult to imagine how filopodia could play a role in virus infection in whole organisms as they are most commonly observed *in vitro*, not whole tissues. They are thought to play a role primarily during embryogenesis and development (Martin and Parkhurst, 2004), initiating contact between cells as prelude to formation of longer-lasting connections. Notable examples of filopodial involvement are mediating cell-cell contacts during organ development and wound healing, or directing the growth of neuronal growth-cone (Figure 4.1). Rather than in *de novo* infection, filopodial protrusion may be important for cell-cell spread (i.e. the direct uptake of virions from the surface of infected cells (Sattentau, 2010). Cell-cell

spread is thought to be the primary route of dissemination *in vivo* (Uchil *et al.*, 2019). Human immunodeficiency virus (HIV) infected lymphocytes can initiate virus receptor-mediated binding to target cells. This leads to the formation of a virological synapse, an analogue to the immunological synapse formed between healthy immune cells (Jolly and Sattentau, 2004). Similar connections, mediated by filopodia, were observed *in vitro* between target and MLV-infected cells (Sherer *et al.*, 2007).

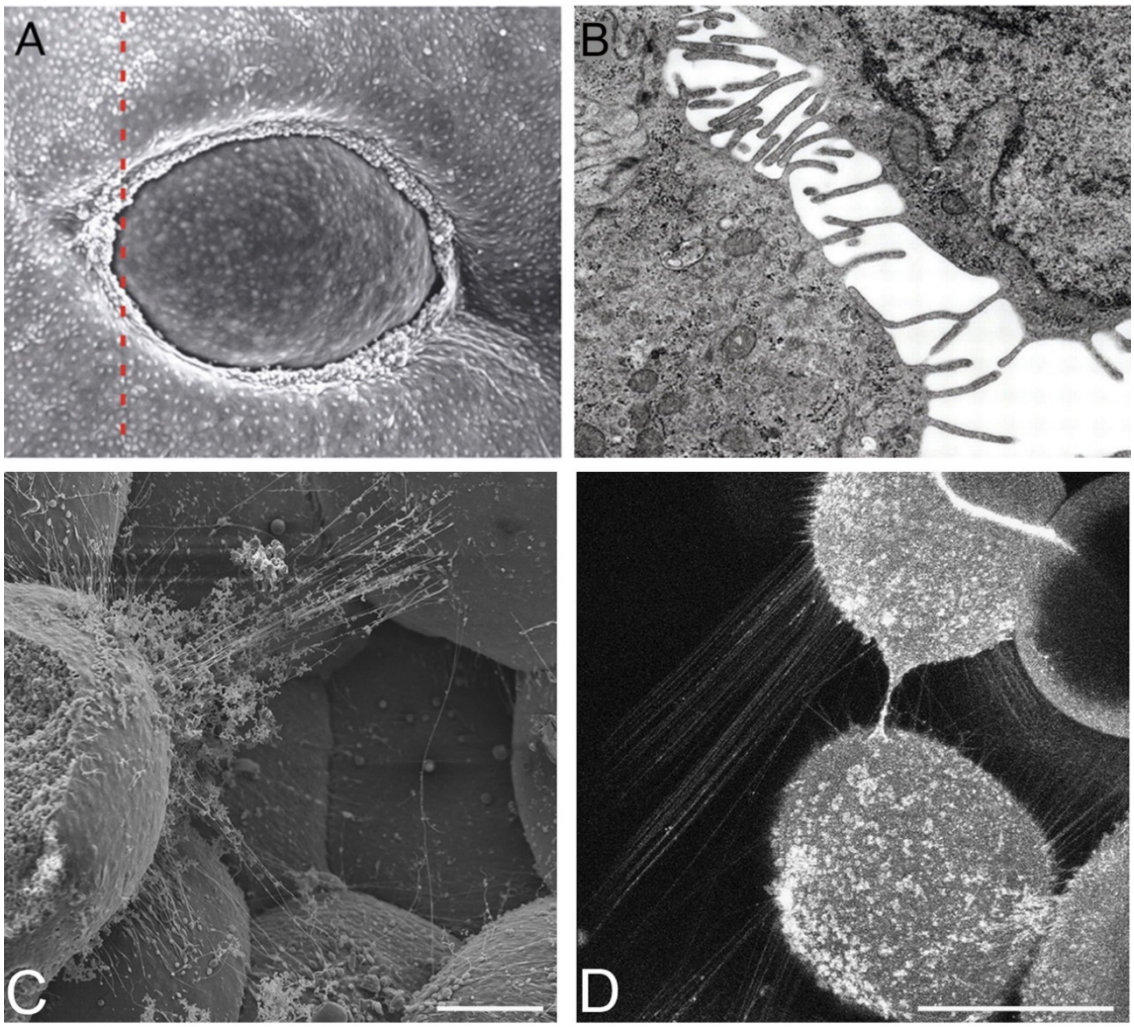


Figure 4.1 Role of filopodia in development. (**A**) A scanning EM image of a resin-embedded mouse embryo eye that was undergoing eyelid fusion. Dashed red line indicates the position of sections that were subsequently imaged in transmission EM. (**B**) A detailed view of one of these sections, showing a large density of filopodia between opposing cells. (**C**) An SEM image of *Xenopus Laevis* blastula, magnified to show numerous long membranous protrusions connecting opposing cells of the central cavity (blastula). (**D**) An equivalent experiment performed with fluorescently labelled membrane in light-sheet FM. In time-lapse data it was possible to see transport of large vesicles along the outside of the long protrusions. Scale bars represent (C) 50 µm (D) 200 µm. Figure modified from Martin and Parkhurst (2004). Data originally published in Zenz *et al.* (2003) and Danilchik *et al.* (2013).

In 2005, Lehmann and colleagues described a process where murine leukaemia virus (MLV) particles were transported along filopodia towards the body of adherent cells, which they termed virus surfing (Figure 4.2) (Lehmann *et al.*, 2005). A large number of viruses from *Retroviridae*, *Poxviridae*, *Papillomaviridae*, *Herpesviridae*, *Adenoviridae* and *Rhabdoviridae* have been shown to engage in surfing; notably there has not been an example of a virus that does not (Lehmann *et al.*, 2005, Mercer and Helenius, 2008, Schelhaas *et al.*, 2008, Oh *et al.*, 2010, Burckhardt *et al.*, 2011, Xu *et al.*, 2015).

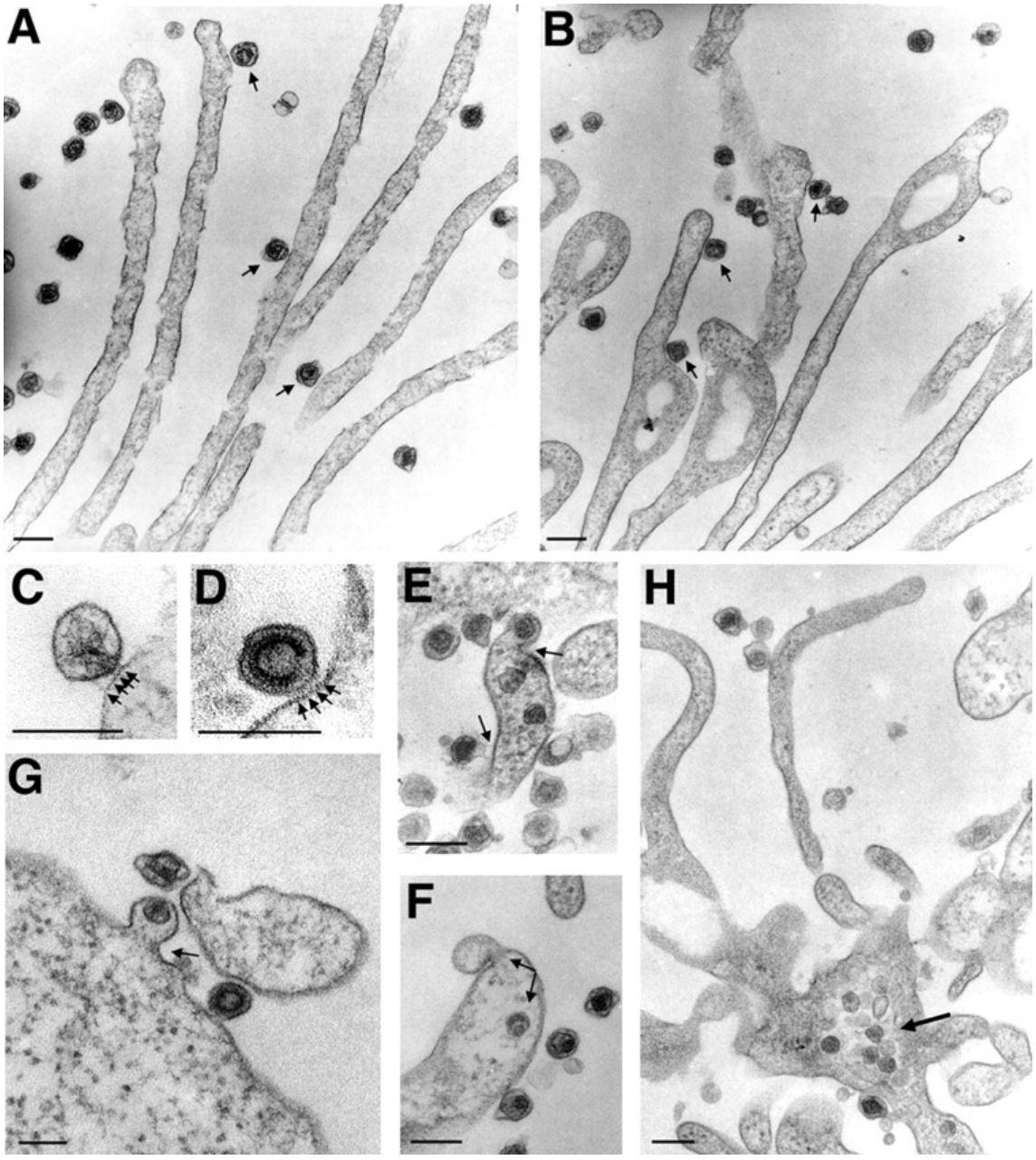


Figure 4.2 Putative surfing events and MLV membrane fusion. Sections of resin-embedded HEK 293 with MLV particles bound to filopodia (**A, B, H**). Membrane fusion at the base of filopodia (**E, F, G**) and spikes connecting the virus and cell membranes (**C, D**) were observed. Scale bars represent 200 nm. Reproduced from Lehmann *et al.* (2005).

Uptake of non-viral particles

It is tempting to surmise that this surfing phenomenon may be a route for virions to bind the host membrane and be trafficked to areas of active plasma membrane fusion or endocytosis as a prelude to cell entry. Disruption of the actin network or myosin-II

activity abolished surfing and also reduced virus infectivity in microvilli-rich cells (Lehmann *et al.*, 2005). Surfing may therefore increase infectivity *in vitro* by facilitating virus entry. In addition to virus particles, there have been several examples of non-viral particles engaging in a similar process. For example, bovine serum albumin-coated gold nanoparticles have been used to probe actin motility before the discovery of fluorescent proteins (Albrecht-Buehler and Lancaster, 1976). Others include (uncoated) polystyrene beads, epidermal growth factor-coated beads, DNA-lipofectamine complexes used for transfection of mammalian cells, and exosomes produced by neighbouring cells (Lidke *et al.*, 2005, Rehman *et al.*, 2013, Kohler and Rohrbach, 2015). This large number of different surfing cargoes suggests that surfing might be a (currently unknown) transport process that can be hijacked by viruses to facilitate cell entry. Considering the large number of transmembrane proteins that can engage in surfing (inferring from the abundance of surfing viruses, each with a unique cellular receptor) it is possible to speculate that it is ubiquitous for most plasma membrane proteins. The lack of information about this process comes, presumably, from the transient nature of the surfing complex stemming from the dynamic state of actin cytoskeleton at the cellular periphery.

Actin retrograde flow

The molecular mechanism of surfing is unknown, but its rate (~ 1 µm min^{-1} ~ 20 $nm.s^{-1}$) and direction correlates strongly with actin retrograde flow (ARF). Additionally, it was observed that disruption of the actin network or myosin-II activity abolished surfing (Lehmann *et al.*, 2005). ARF is a description for the rear-ward flow of actin network at

the leading edge of adherent cells. It is generated both by the force of polymerising actin filaments pushing against the plasma membrane, and by activity of myosin-II motors (Lin *et al.*, 1996). ARF is involved, for example, in maturation of focal adhesions, which in turn transmits its force to the extracellular matrix. Similar to focal adhesions, there has to be a physical connection between actin filaments and the (virus) receptor bound to surfing cargo (Figure 4.3).

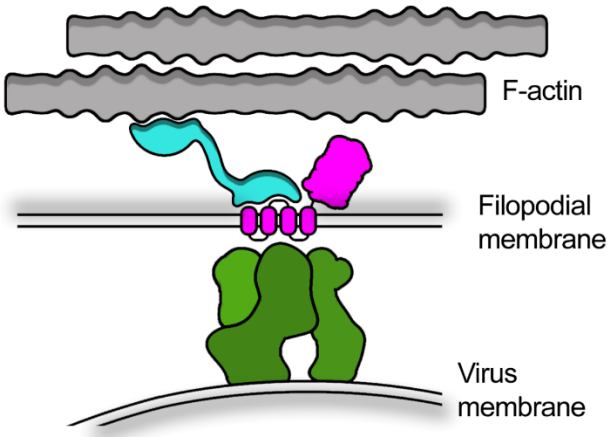


Figure 4.3 Current model of virus surfing. Viruses, such as murine leukemia virus (MLV) bind to their recognition receptor on the cell surface. MLV contains a single envelope glycoprotein Env that mediates both binding to mCAT-1 (mouse cationic amino acid receptor 1) and membrane fusion. There is likely a direct or indirect connection between mCAT-1 and F-actin that transmits the force of actin retrograde flow to the virus particle located on the outside of the cell.

Studying dynamic virus-host interactions by cET

The aim of this study was to characterise virus surfing by cET. This method is uniquely suited to observe virus surfing, as the speed of vitrification ensures the preservation of even transient interactions that may occur between the virus, its receptor and any direct or indirect connections to the actin network. For example, Riedel *et al.* (2017) visualised a density for putative MLV Env binding event to the host receptor mCAT-1 which, presumably, precedes membrane fusion (Figure 4.3).

There are several reasons that make viruses suitable vehicles to investigate surfing over other cargoes: Their interaction with the cell is relatively well understood, allowing observations to be validated with existing structural data. The size of virions (80-140 nm) allows them to be identified at medium magnification in EM, which is needed for selection of areas for data collection. And finally, there is a potential for observing host-pathogen events that may not be related to virus surfing but are valuable for understanding of virus infection.

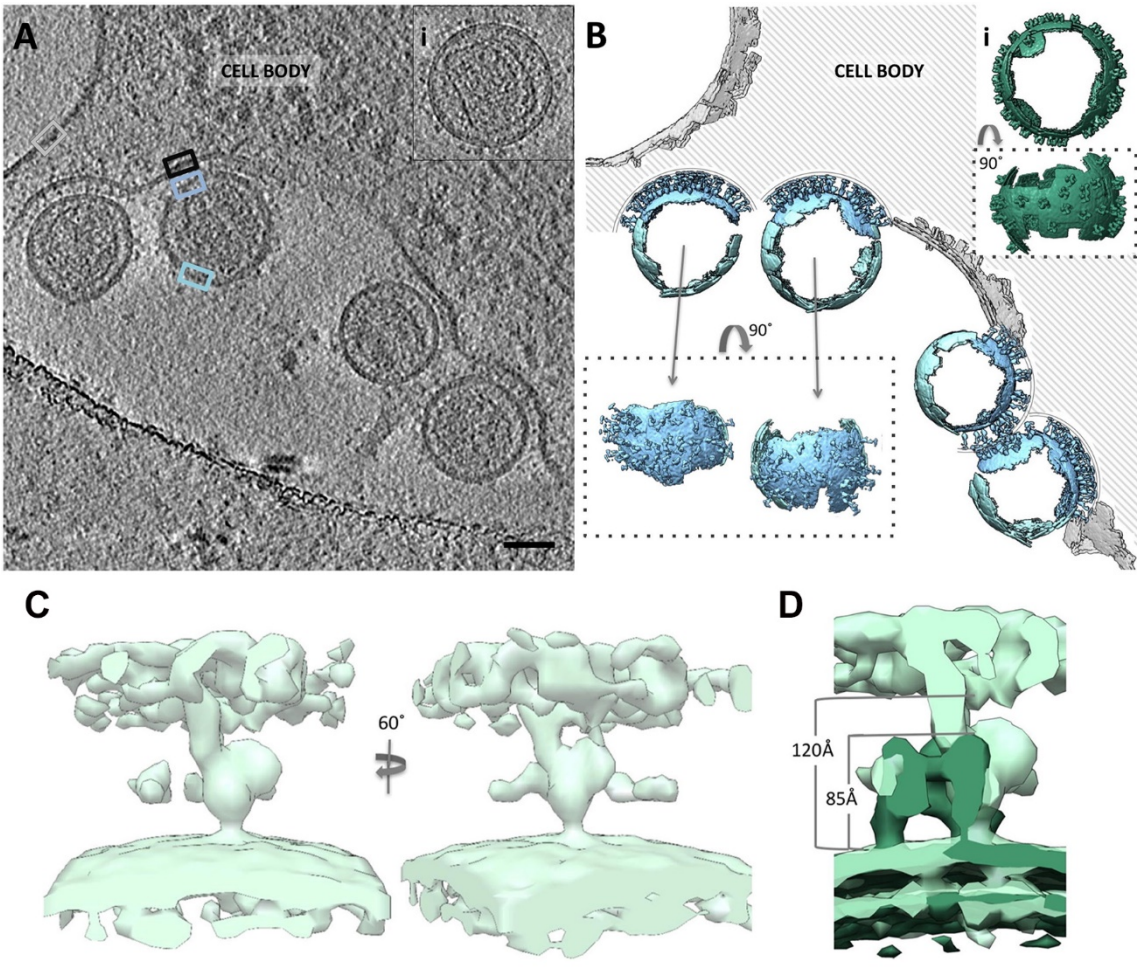


Figure 4.4 Putative MLV Env fusion intermediate captured by cET. (**A**) A slice through a tomogram showing four MLV particle binding to XC cell membrane through apparently periodic densities. Inset shows an example of a typical MLV mature particle observed in the absence of cells. (**B**) The same volume represented by plotting SVA map at the coordinates of each individual particle. Inset shows an equivalent plot generated with SVA map of MLV Env particles from isolated virus particles. (**C**) SVA map of the putative Env fusion intermediate, showing a connection with the host membrane. (**D**) Overlay of (**C**) with SVA map of MLV Env indicating substantial conformational changes taking place. Scale bar 50 nm. Modified from Riedel *et al.* (2017).

Two viruses, adenovirus type 2 and MLV were used to study viral surfing. Adenovirus type 2 is a non-enveloped virus; it binds to cellular receptor coxsackie adenovirus receptor (CAR) via its extended penton fibres (Freimuth *et al.*, 1999). CAR is an immunoglobulin superfamily protein found in a wide variety of tissue types, mediating cell-cell adhesion by forming homodimers localised to tight junctions. This high affinity interaction achieves viral attachment but is not sufficient for entry. Entry is mediated by a second binding event of the viral penton base capsid protein with the host αV-integrin, which triggers clathrin mediated endocytosis (Wickham *et al.*, 1993). Once encapsulated in the endosome, acidification triggers the release of protein VI which ruptures the endosomal membrane in a process called endosomal escape. Following endosomal escape, the capsid is transported along microtubules to the nucleus where it can inject its double stranded DNA genome. The separation of viral attachment and entry by two sets of interactions makes this particularly useful for investigating surfing behaviour.

At first glance, surfing is not as beneficial for those enveloped viruses, such as MLV, that are able to fuse with the plasma membrane as they should, in theory, be able to fuse with any part of the plasma membrane. Even though the natural mode of cell entry is still debated, XC (rat Rous-induced sarcoma cell line) cells are unique in that they allow MLV fusion to occur at the plasma membrane. Nevertheless, MLV fusion has not been observed on filopodia or lamellipodia by FM or classical EM. There is no concrete data suggesting why this is the case, but it is presumably related to the dense actin network at the cell periphery. Virus surfing transports MLV virions towards the cell body where

fusion, or endocytosis is possible. A mature MLV virion typically contains multiple copies of Env (envelope) glycoprotein, which consists of TM (transmembrane) and SU (surface) subunits that are covalently linked by a disulphide. SU mediates binding to mCAT-1 (mouse cationic amino acid transporter 1); this leads to a Ca^{+2} dependent isomerisation of the SU-TM disulphide bond. TM, following SU dissociation, catalyses membrane fusion. Notably, SU-TM dissociation can occur independently of mCAT-1 binding in a process called shedding.

Utilising these two model systems, the structural basis of surfing was investigated by a variety of approaches including fluorescence microscopy, cET and live-CLEM. This study is a result of a long-lasting collaboration between Kay Grünewald, Christiane Riedel (CR), Harald Woodrich (HW) and Walther Mothes (WM). CR established initial methods for cellular cET and MLV preparation. WM provided MLV plasmids and XC cell lines and HW provided adenovirus stocks, CAR plasmids and U2OS cell lines (human osteosarcoma). Personal communication with Lloyd Smith and Matthew Lockett was essential for development of covalent carboxylic acid coating of EM grids. VP performed all other work.

4.2 Results and discussion

Overview of experimental systems

Virus surfing experiments, i.e. FM virus tracking on target cells were performed in order to characterise the behaviour of the experimental setup. Two different viruses, MLV and adenovirus, were used for observation of virus surfing. MLV was labelled with

yellow fluorescent protein (YFP) inserted in the proline-rich region of Env (MLV-YFPenv). The target cells, XC, express endogenous CAT-1, but were labelled by stable transfection with mCAT-1 labelled with C-terminal mApple (this cell line will be referred to as XCmCAT). Adenovirus particles labelled with Alexa488 were initially used with U2OS cells expressing mCherry-labelled CAR (CAR-mCherry). U2OS cells, however, contain very few filopodia and were replaced by XC cells expressing CAR-mCherry. XC cells typically contain a large number of long filopodia (~ 2 μm) which made them suitable for this study. The morphology of XC cells varied substantially; seeding very low densities of cells would result in colonies with consistent intra-colony morphology, indicating that it was hereditary. The most typical morphology was a cell with no distinct polarity, and a mixture of lamellipodia and one to six pseudopodia terminated with filopodia (reminiscent of neuronal growth-cone).

MLV surfing on XCmCAT cells

Addition of MLV-YFPenv to XCmCAT cells resulted in rapid YFP-staining of the cell membrane most likely the result of SU-YFP binding. This was followed by binding and surfing of fluorescent foci, presumably single virus particles (Figure 4.5). The majority of particles that bound to cells proceeded to surf immediately after binding (the lag time between time frames was typically 2-12 s). A small proportion of particles first diffused in 2D (on lamellipodia) or in ~ 1D (on filopodia) before surfing. It has been suggested that this could be the result of non-specific virus binding to cellular glycosaminoglycans (Quentin Sattentau, personal communication). The surfing rate of individual events was in the range of 20-30 $nm.s^{-1}$ and generally decreased closer towards the body of the cell

(Figure 4.6). Particles on the same cellular protrusion typically moved with similar velocities and without stopping, but substantial velocity gradients could also be observed.

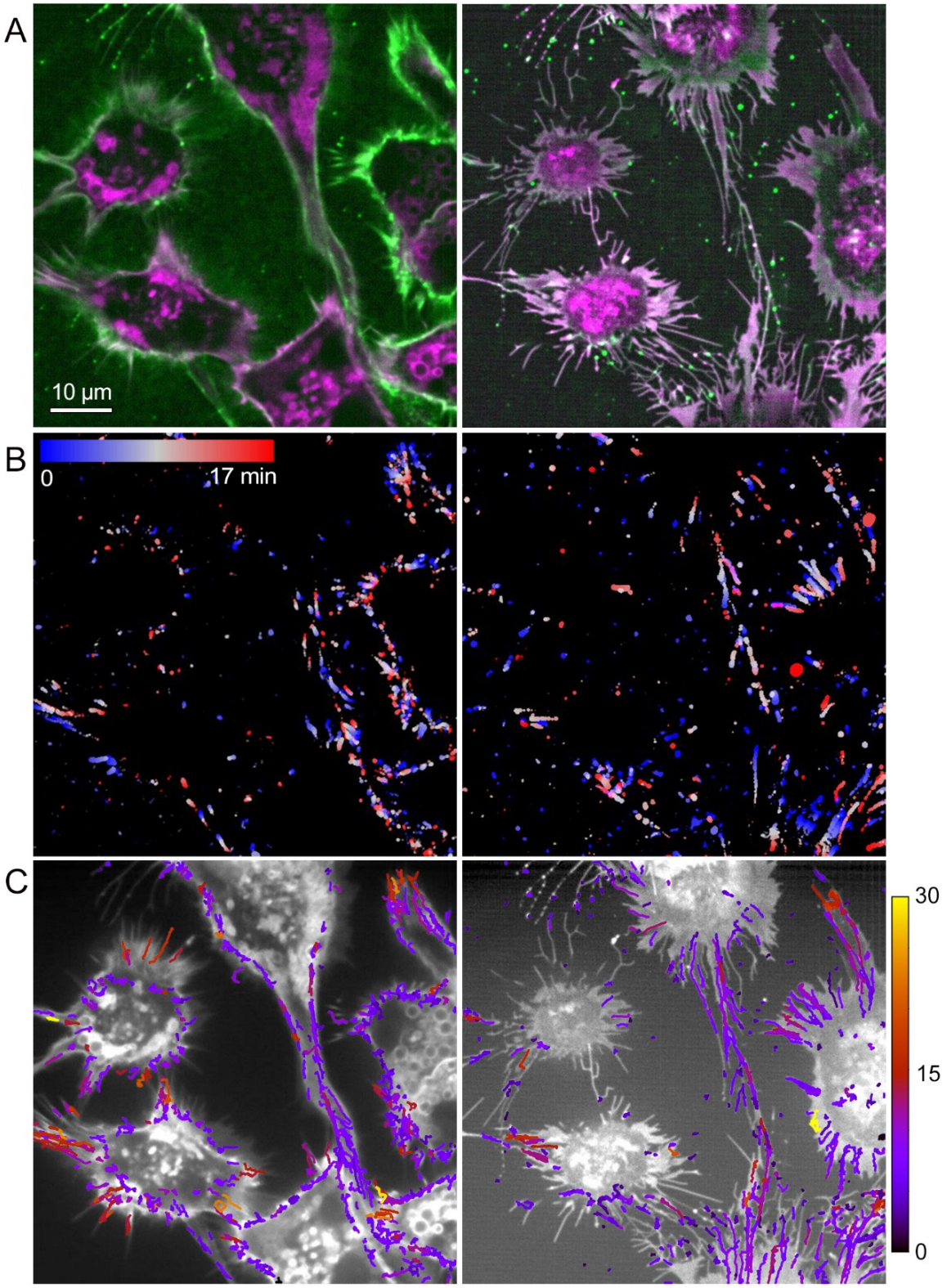


Figure 4.5 MLV virus surfing experiment. MLV-YFPenv particles (~ 10^5 focus forming units, ffu) were added to XCmCAT cells and imaged over 4 hours at 12 s intervals using a spinning disc confocal microscope. All panels correspond to the same experiment; left column shows data from the first 17 min, right column shows the last 17 min. Please note that the focus has shifted slightly over the course of the experiment from ~ 1 µm to ~ 100 nm above the coverslip, judging by the increased intensity of filopodia (100-200 nm diameter**).** (**A**) Composite image showing median sums of the green (MLV-YFPenv) and magenta channel time frames (XCmCAT), showing the extent of cell retraction over the course of the experiment. These morphological changes occurred, to a lesser extent, without virus addition, indicating that they were the result of stress caused by both virus infection and illumination. Several green foci can be seen, which correspond to immobile virus particles (or clusters of virus particles) bound to the coverslip or membrane-bound structures that were "abandoned" by cells (see also Figure 4.6). Both stationary and 1D-diffusing viruses could be seen on retraction fibre remnants. (**B**) Temporal colour-coded images indicating particle dynamics. Before colour-coding, 3 time frames were averaged to reduce intensity of unbound (diffusing) particles. (**C**) Automated single-particle tracking results were overlaid with median sums of the red channel. The median velocity of each particle track colour-coded, scale bar units are in [$nm.s^{-1}$]. Some yellow tracks, likely corresponding to diffusing particles, can be seen in both images.

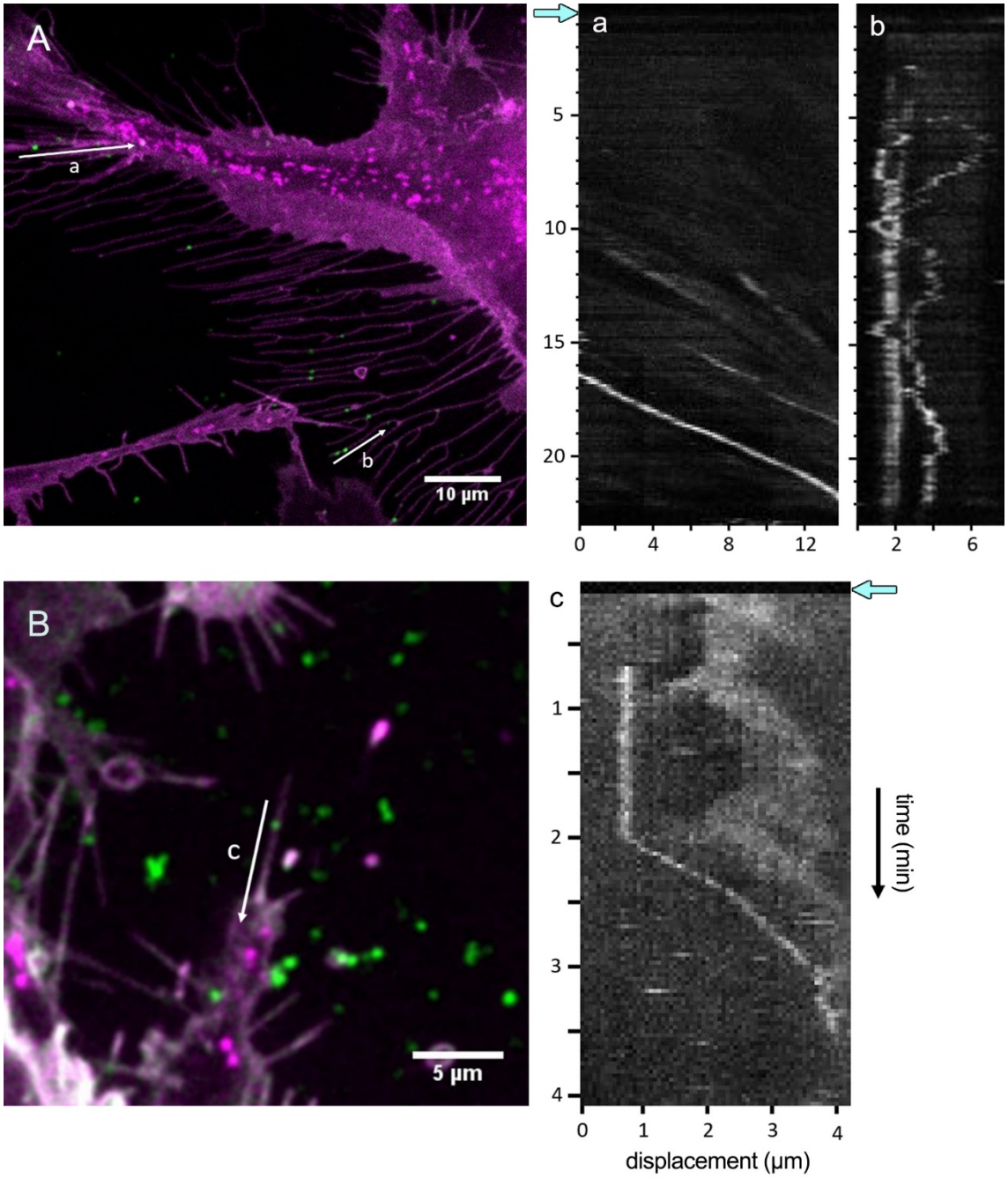


Figure 4.6 Heterogeneous behaviour of virus particles interacting with target cells. Representative frames (confocal sections) of time-lapse virus surfing experiments. MLV YFPenv virions bound to and surfed along filopodia of XCmCAT cells (magenta). White arrows (a, b, c) indicate the area sampled for kymographs **a**,**b** and **c.** There were three main categories of interactions that could be identified in fluorescence microscopy: (**A**) shows a steady directional transport of virions towards the cell body and (**B**) restricted diffusion of MLV along remnant retraction fibres. The virus particle in (**C**) attached to a filopodium and remained stationary, before surfing towards the filopodial base. Cyan arrows indicate the point where MLV YFPenv was added.

Surfing experiments could be performed for extended periods of time (longer than 240 min, Figure 4.5). Longer observations resulted in substantial morphological

changes, but both the surfing velocities and frequency of surfing events remained constant. Cells typically retracted their long pseudo- and filopodia after seconds to minutes and would continue to round up. Nevertheless, virus particles continued to surf on protrusions that remained attached to the cell substrate (retraction fibres, figure 4.5). The extent of retraction was highly variable between individual cells, as some continued to extend their filo- and lamellipodia after tens of minutes. Cell-cell fusion could be observed between closely-packed cells, which was a clear evidence for MLV fusing at the plasma membrane (Figure 4.7).

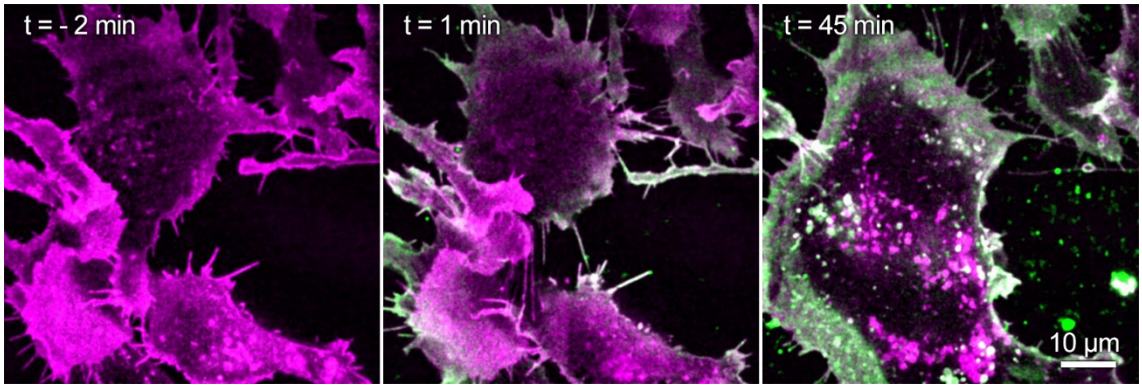


Figure 4.7 Cell-cell fusion caused by large number of virus entry events. Shown are single frames of a confocal time-lapse experiment 2 min before virus addition, 1 min and 45 min after virus addition. Colour-coding is equivalent to figures 4.5 and 4.6. Fusion of three neighbouring cells was observed ~ 45 min after virus addition. The cell-cell fusion is likely caused by MLV YFPenv particles that were mixed with host membrane during cell entry, but were not directly involved in membrane fusion.

MLV-YFPenv does not bind to a large proportion of XC cells

There was a large variability in the number of surfing events that could be observed on any one cell on a microscope slide. In order to quantify this observation, surfing experiments were imaged for a set amount of time (36 s) and all virus particles bound to cells were counted in a 7 µm thick confocal Z-stack. Five different XC cell lines were

used in order to investigate whether there was an effect of passaging or selection: XC cells sourced from Walther Mothes's laboratory (XC_{WM}) stably expressing mCAT-1 labelled with mApple, mCherry, or CFP, XC_{WM} parental cell line, and XC cells from Quentin Sattentau's laboratory stably expressing mCAT-1-mApple. Across all cell lines a total of 444 putative surfing events was counted on 159 cells, but only 45 were observed on filopodia or retraction fibres that would be accessible by EM. Approximately two thirds had less than 5, and a third of all cells had no surfing virus particles associated with them. The XC parental cell line did not perform substantially worse than average (Figure 4.8).

A likely explanation for the extremely low number of binding events is that virus-free SU particles outcompete virus particles for mCAT-1 binding, due to their smaller size (Figure 4.8). Consistent with this hypothesis, there was a linear relationship between the average cell-associated fluorescent intensity of green and red fluorescent channels despite a large variation between individual cells. This indicates that the concentration of virus-free SU is vastly in excess of any variability in the number of mCAT-1 on the cell surface. An obvious solution to this problem would be reduce virus-free SU concentration. Increasing Ca^{2+} buffer concentration and using CaptoCore columns, which bind small molecules (smaller than 0.7 MDa), reduced virus-free SU concentration in MLV-YFPenv preparations, but this did not result in a substantial increase in the number of observed surfing events.

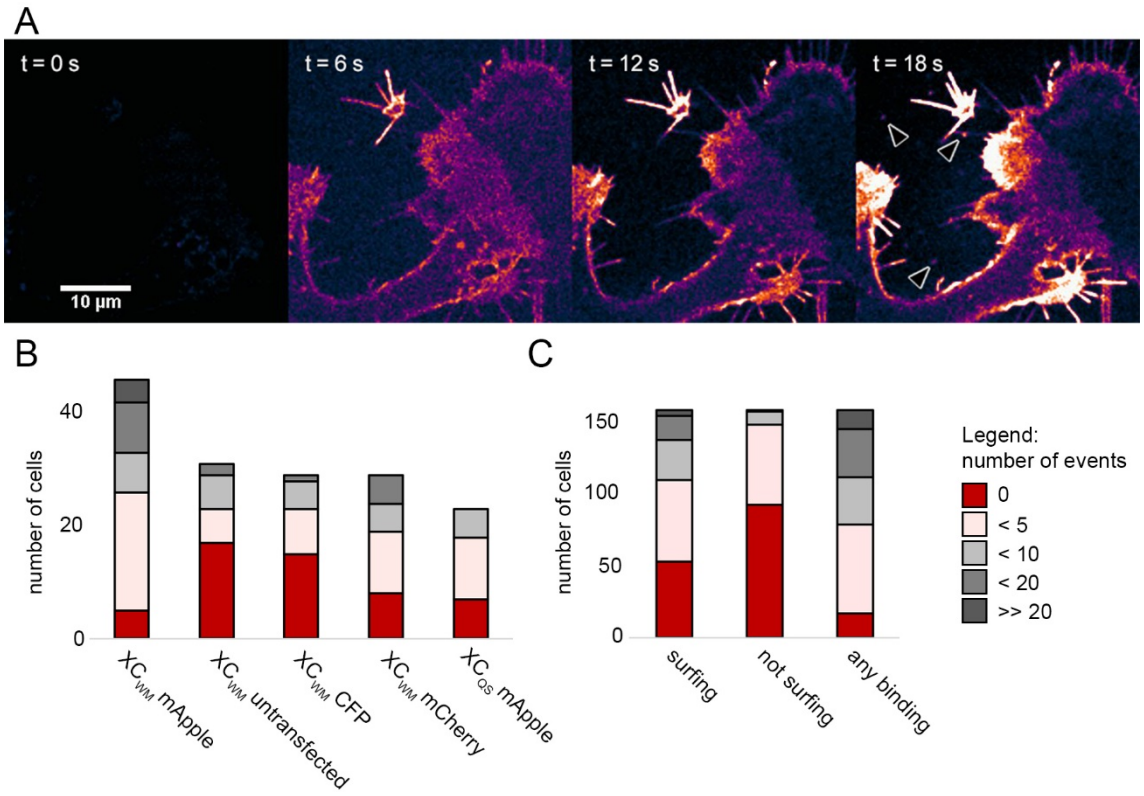


Figure 4.8 Virus surfing events are rare, possibly due to competition with SU-YFP. (**A**) Frames of confocal time-lapse virus surfing experiment showing several time points after virus addition. Only the green channel, corresponding to YFP fluorescence is shown. Cell medium was not mixed to visualise the difference in diffusion rates of what is presumably shed SU-YFP, and full virus particles. Membrane staining could be observed quickly after virus addition, several seconds before first virus particles can be observed (highlighted with black arrowheads). (**B**) The frequency of observing virus surfing was quantified by counting all events associated with any one cell observed within 36 s inside a confocal volume. Acquisition was started several seconds after virus addition to allow re-focusing. This experiment was performed with XC cell lines from two different sources (XC_{WM}, XC_{QS}, both presumably originating from the same parental cell line) stably expressing mCAT-1 labelled with a fluorescent protein where indicated. (**C**) Comparison of surfing, not surfing (static or diffusing, refer to Figure 4.6 for examples) or any binding events (combination of surfing and not surfing) across all cells used for (**B**). These data indicate that ~ 50% of cells were not bound by 5 or fewer virus particles. The relatively low numbers of non-surfing particles indicate that binding events almost always result in surfing.

Adenovirus surfing precedes endocytosis

Adenovirus surfing was observed on U2OS expressing native levels of CAR, or XC cells expressing CAR-mCherry. XC cells were used for their superior numbers of thin protrusions, despite it being a rat cell line used to study a human pathogen. Transfection with CAR-mCherry resulted in a faint amount of fluorescence on the cell membrane with

the majority originating from intracellular vesicles. The appearance of bright patches between cells, presumably cell-cell adhesions, was observed. Addition of adenovirus-Alexa488 particles resulted in bright fluorescent foci surfing towards cell bodies where they switched to a much faster mode of movement, presumably microtubule-mediated transport (Figure 4.9). A larger number of surfing events was observed relative to MLV-YFPenv using ~ 10-fold less virus, but this observation was not quantified further. There was no adenovirus binding to XC cells expressing fluorescent mCAT-1, indicating that CAR is the principal adhesion receptor in this model system.

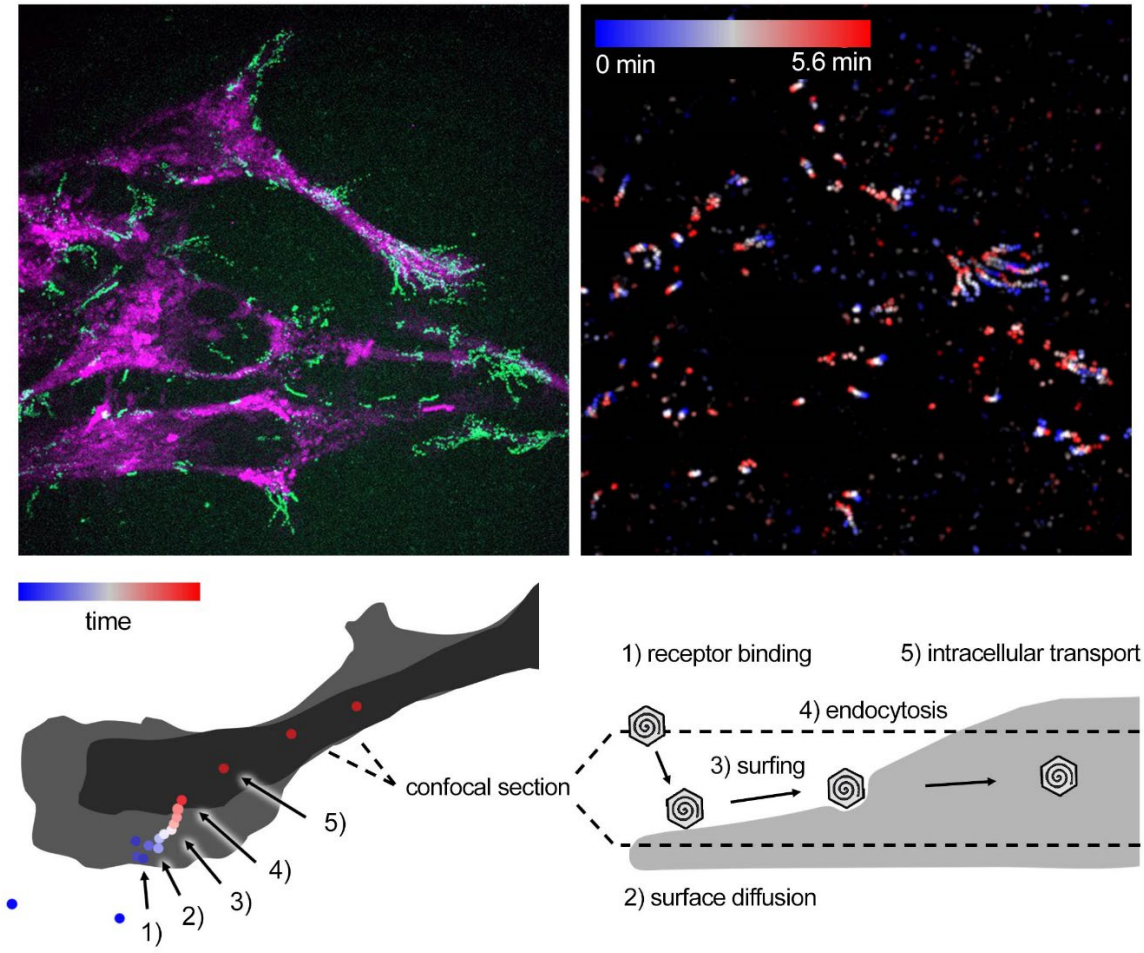


Figure 4.9 Adenovirus surfing. An equivalent experiment to that described in figure 4.5 was performed with adenovirus labelled with Alexa488. Top left shows a median sum of the red channel (displayed in magenta) corresponding to CAR-mCherry overlaid with the green channel corresponding to adenovirus Alexa488. Numerous, sometimes overlapping virus tracks are apparent on cell peripheries. Top right panel shows only the green channel, coloured by time. At the bottom is a diagram describing individual stages of a "typical" adenovirus entering a cell.

Virus binding events observed by cET are structurally heterogeneous

MLV and adenovirus interaction with XC cells was investigated by cET in parallel to FM surfing experiments. Putative virus binding events were observed in medium magnification images (nominal 9300x); tomograms were collected of events suspended over holes in support film (Figure 4.10). Visual inspection of tomograms showed a large heterogeneity in virus binding to cell membranes. The distances between MLV envelope and the cell membrane ranged from ~ 0 nm to more than 10 nm (Figure 4.11). There were a few events where Env spikes could be reliably identified in an orientation consistent with binding to (presumably) mCAT-1. However, the majority of connections were long filaments (longer than 10 nm) with no resemblance to Env. The cell membrane generally contained a large density of similar filaments, which makes it unclear whether such connections are significant. Inside the cytoplasm, there were no consistent structural features observed between actin filaments and the cell membrane. While there were several membrane-actin connections in the vicinity of virus binding sites, similar structures could be found elsewhere. The large heterogeneity and crowding inside the actin-membrane gap did not allow rigorous classification to be performed. Adenovirus binding events were similar in that there was substantial heterogeneity of both the distances between virus capsids and cell membranes, and composition of the actin-membrane gap (Figure 4.12). The analysis was further complicated by a shadowing effect caused by the large density of viral nucleic acid, which reduces the SNR of regions around the adenovirus capsid.

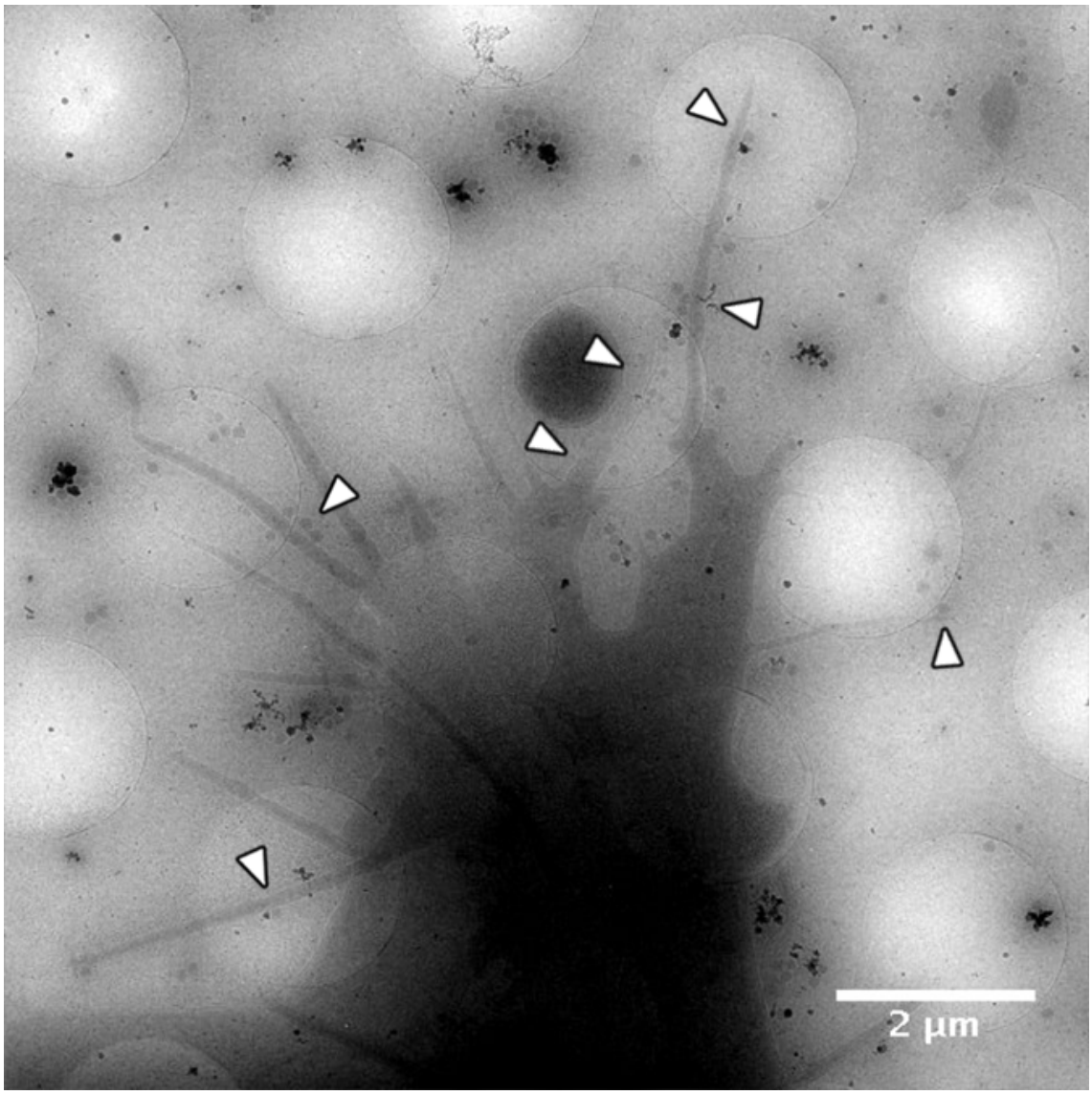


Figure 4.10 An overview of MLV virions interacting with a pseudopodium. A range of putative virus-host interaction events can be discerned; some are indicated with white arrowhead. Notice that the majority of events are located over the carbon support and would not be used for tomogram acquisition. It is also apparent that several mitochondria are damaged, presumably as a result of the medium flowing through the holes in carbon film during blotting. This EM grid was coated with fibronectin but not graphene oxide (GO) nor continuous carbon.

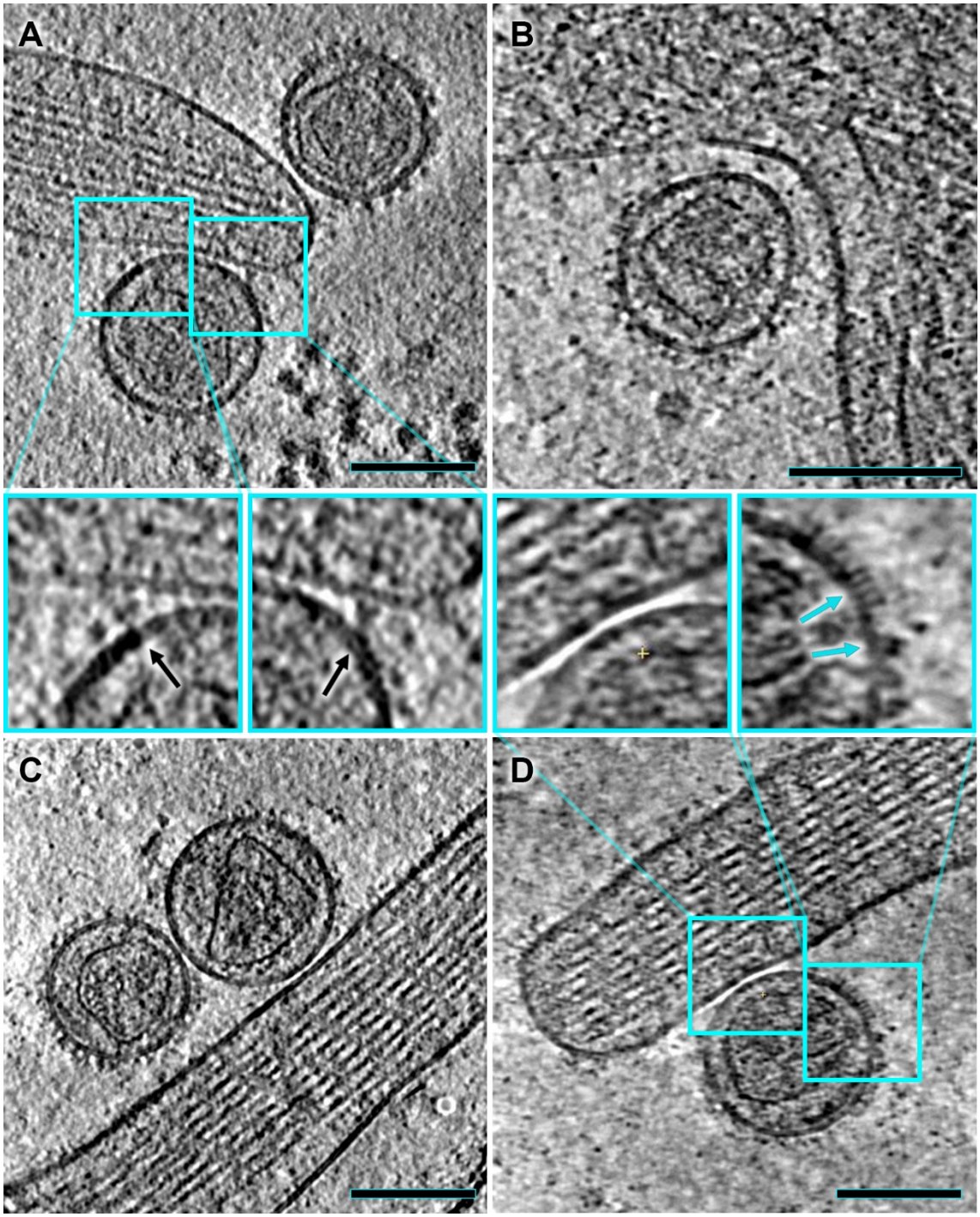


Figure 4.11 Tomographic sections of representative MLV-XC cell interactions. Tomograms were reconstructed with SIRT-like filter for visual analysis, shown are slices ~ 10 nm in thickness. Areas indicated with cyan squares were magnified 2x in the middle panel. Notice the range of distances between the viral and cell membranes. (**A**) Two virions bound to the tip of a filopodium and several ribosomes released (presumably) by blotting-induced cell rupture. There are two Env-like densities that might be engaged in binding to mCAT-1. (**B**) A longer-distance interaction observed at the base of a filopodium. (**C**) An interaction observed further along a filopodium, indicating a large variability in the Env coverage of MLV particles. (**D**) Two different types of spikes highlighted with cyan arrows were observed on the surface of a (presumably) bound virus. One has clear resemblance to particles averaged by Riedel et al 2016. It is tempting to speculate that the other type corresponds to the TM subunit leftover after SU dissociation. Scale bars represent 100 nm.

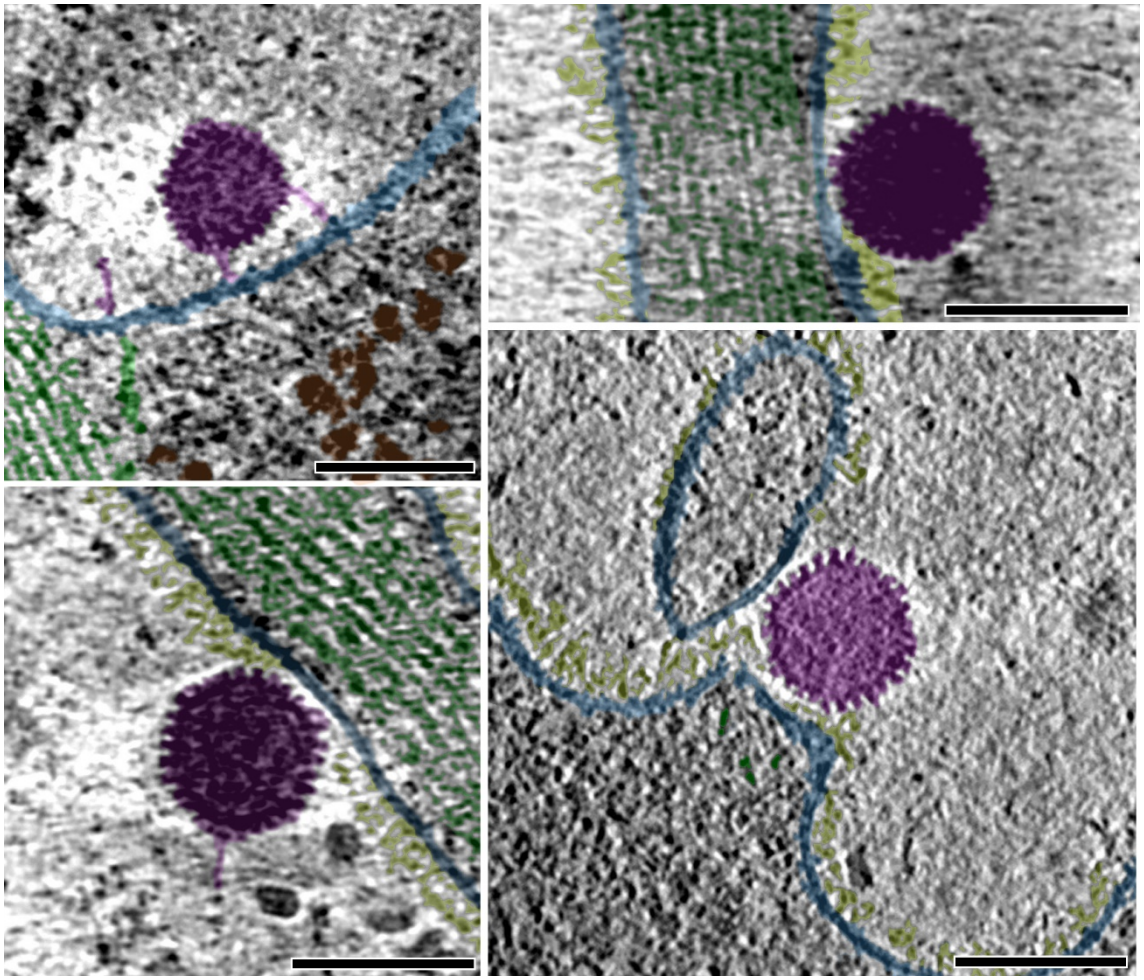


Figure 4.12 Tomographic sections of representative Adenovirus-XC cell interactions. Sections of tomograms were generated as described in figure 4.11. Manual segmentation was performed to indicate densities corresponding to actin filaments (green), adenovirus capsids (magenta), cell membrane (blue), cellular surface glycoproteins (yellow) and ribosomes (orange). Similar to MLV binding, adenovirus capsids were observed at a range of distances from the cell membrane. Penton fibres were observed in orientations consistent with CAR binding in the majority of interaction events. Scale bars represent 100 nm.

Live-CLEM, because history matters

Overall, the largest uncertainty was whether or not any of the observed events were surfing, specific or non-specific binding, or artificial proximity caused by blotting during specimen preparation. This made it clear that the dynamic information about each virus particle (i.e. its history) prior to vitrification was required to allow putative binding events to be correctly classified. It is possible to imagine a method where virus surfing

experiments are performed on EM grids followed by quick blotting and plunge-freezing. The mean surfing velocity is ~ 1 µm min^{-1} and the length of XC cell filopodia is typically more than 2 µm, meaning that there should be a window for plunge-freezing in the order of minutes. It should be possible to predict the position of surfing particles in EM, assuming that it continues to move with approximately the same velocity after the last frame of FM imaging and vitrification. This method will be referred to as "live-CLEM", even though it does not strictly involve correlation between data acquired with the same specimen. Nevertheless, it arguably conveys the general outline and aims of the experimental method. It is important to note that even conventional cryo-CLEM is an extremely low-throughput method, which means that it would not feasible to collect all cET data in this manner. However, it is reasonable to propose that initial characterisation of events by live-CLEM would allow those without any historical information to be classified with sufficient confidence. Structural characterisation obtained by comparison within, and between virus-binding classes would provide sufficient context for sub-volume averaging.

Designing live-CLEM hardware

It was clear that in order to maximise the likelihood of "catching" a surfing virus by live-CLEM would be by minimising the time between FM imaging and vitrification. Without modification to the preparation procedure, the EM grid submerged in cell-culture medium on a microscope slide would have to be mounted on a pair of negative-pressure tweezers (plunging tweezers); these would then be secured to a plunge-freezing device, a solution of gold-fiducial markers applied to the grid, which

would then be blotted and finally dropped into liquid ethane-propane mixture cooled to ~ 81° K. The largest variable in this process is grid mounting which can take anywhere between 15 s and several minutes. This is a consequence of the requirement to keep cells submerged in a sufficient volume of liquid to make concentrating effects of evaporation negligible and the extremely delicate nature of the ~ 20 μm thick gold grid, which makes it difficult to pick up without inflicting damage.

To address this issue, a microscope stage insert was modified in order to allow imaging of EM grids mounted on plunging tweezers (Figure 4.13). Initial iterations were designed around the use of conventional straight plunging tweezers and an adaptor holding a glass coverslip attached directly to the microscope objective. The reasoning for attaching the coverslip to the objective was that it could be quickly moved out of the way using the microscope motorised controls in order to make space for the grid and tweezers to be extracted safely. Initial testing with a droplet of water suggested that its surface tension would be sufficient to hold enough liquid around the grid. It was also believed that evaporation would not be an issue since it would only take a few seconds of acquisition time to determine if observed virus particles are surfing or not. Both assumptions proved to be wrong, leading to a design with a reservoir for ~ 0.2 ml of liquid (Figure 4.13, B and C). Plunging tweezers were forced into a gap in silicone sealant encased in a "gate". The gate was free to move side to side along rails together with the tweezers, and vacuum grease was used to fill small gaps between moving parts to prevent medium leakage. However, the high viscosity of vacuum grease made specimen movement slow and largely unpredictable.

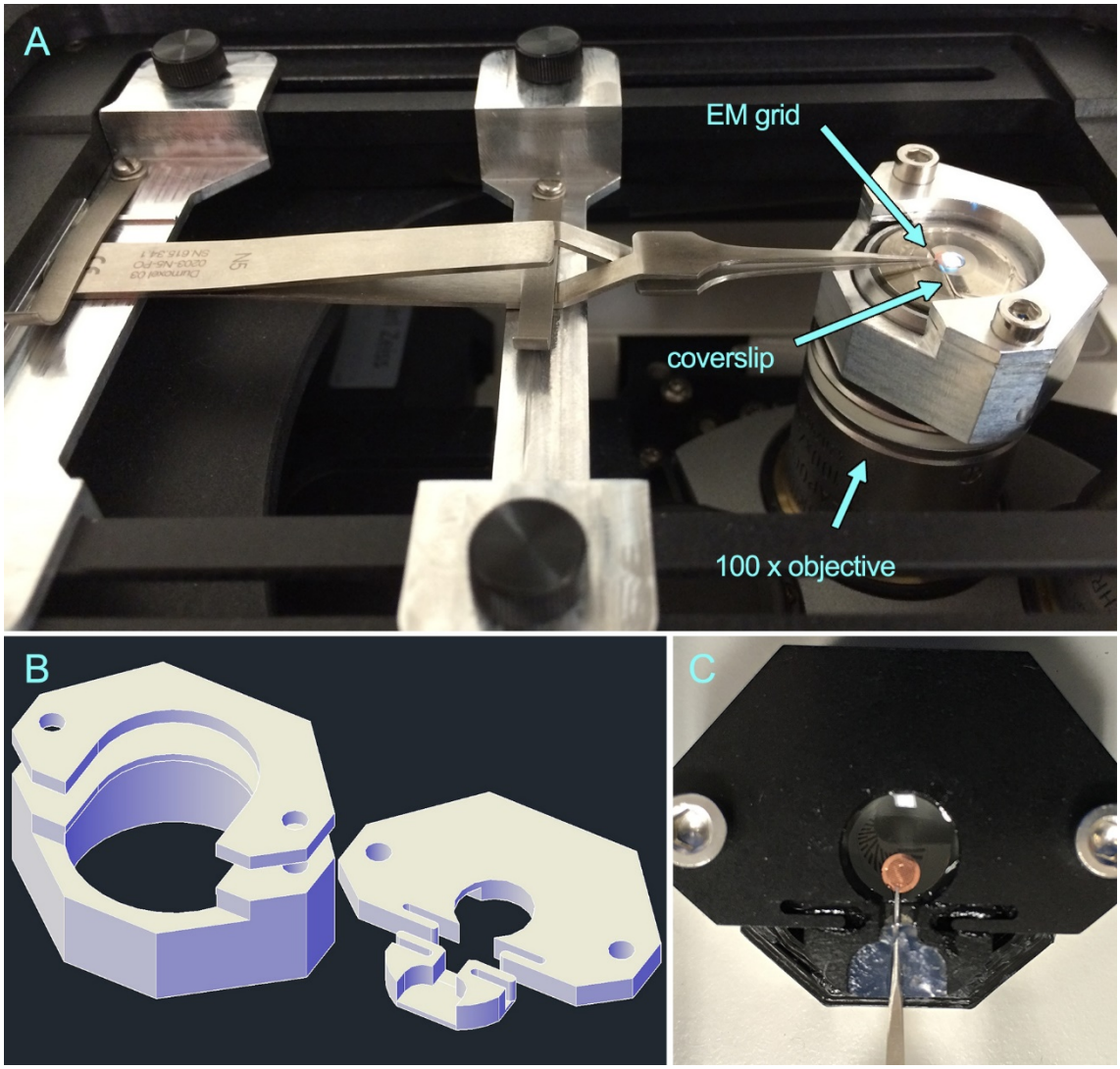


Figure 4.13 Initial live-CLEM stage prototypes for imaging of EM grids mounted on conventional plunging tweezers. (**A**) An overview indicating the position of individual parts. (**B**) 3D rendering of drawings used for machining of prototype parts. (**C**) A "side-entry" adaptor for 100x oil-immersion objective that could hold ~ 0.2 ml of cell medium.

Better results were achieved with designs that made use of "bent tweezers" that have a ~ 3 mm step at the tip, allowing grid to be submerged in liquid and positioned parallel to the coverslip surface. This approach was initially discarded with the assumption that it would not be possible to manufacture tweezers both fine and robust enough for this application. Custom-made tweezers from a commercial manufacturer were too crude for to hold EM grids during FM or plunge-freezing. Surprisingly good results were

obtained by manually shaping straight plunging tweezers using goldsmithing tools and a basic stereomicroscope (Figure 4.14, A). This allowed grids to be suspended above a water-immersion objective lens in a small amount of medium (Figure 4.14, B). The biggest (theoretical) advantage of this approach is that due to the absence of a coverslip, cells can be imaged upside-down, without the signal-attenuating effect of the carbon support film. However, the most successful design made use of a conventional light microscopy slide as a specimen reservoir, secured to the stage rather than the objective itself (Figure 4.14, C). In all previous iterations the specimen moved relative to the surrounding medium, meaning that stage movement could only be used for initial search, not during acquisition. This setup with the working name “live-CLEM stage”, allowed the acquisition of Z-stacks at multiple positions, increasing the chances for observing a surfing event. After FM acquisition, the grid was moved away from the coverslip by pressing against the tweezer handle, which rotated it by ~ 15°, enabling a quick and safe retrieval. Using this system, it was possible to plunge-freeze cells within 30 s of the last frame of FM imaging which would result in ~ 0.5 µm displacement of surfing viruses from their last imaged position.

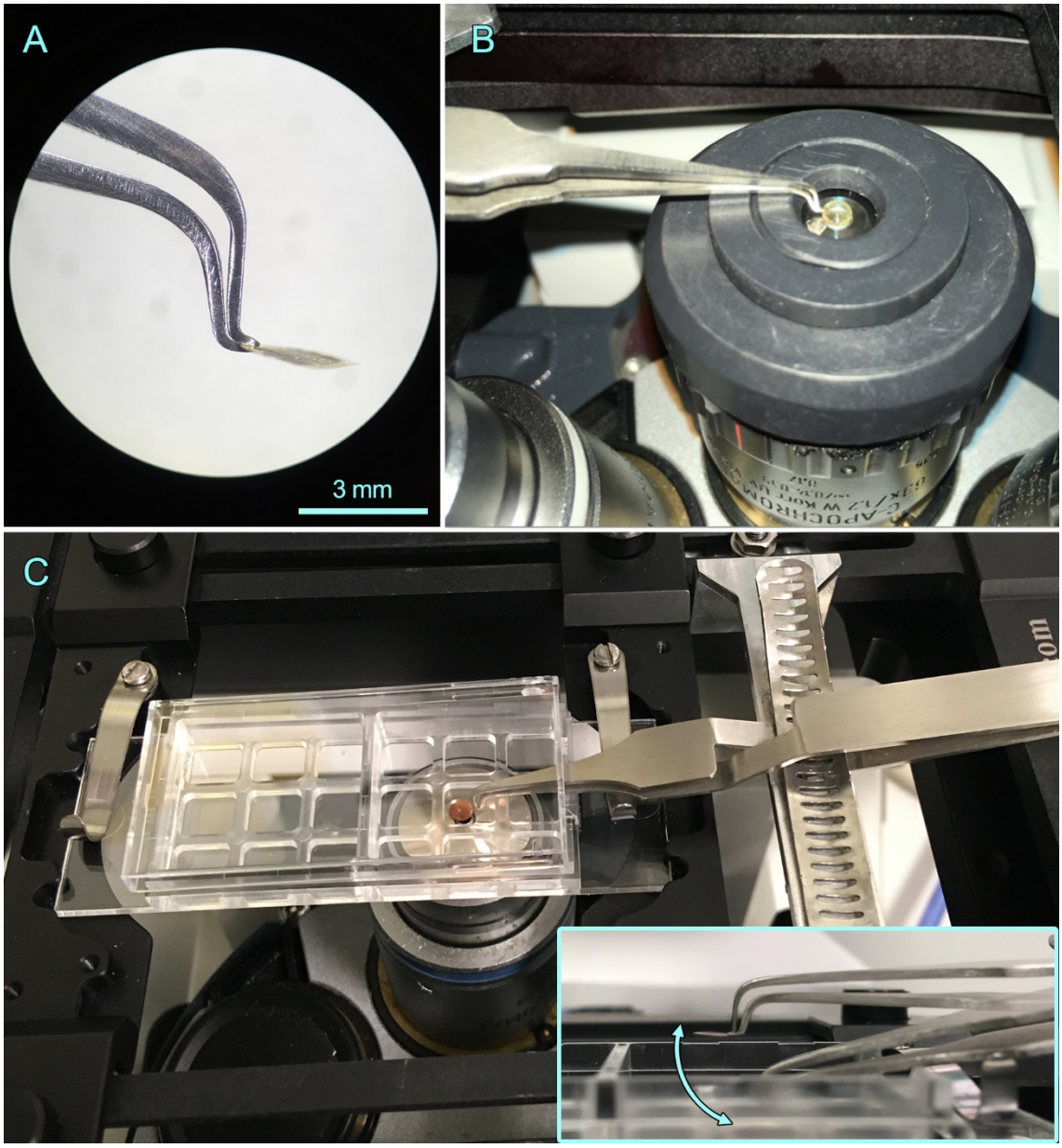


Figure 4.14 The "bent tweezer" approach for live-CLEM imaging. Manual shaping of plunging tweezers allowed grids to be submerged in cell medium during imaging without impeding specimen manipulation capabilities with the motorised stage. (**A**) Stereomicrograph showing a bent tweezer with a grid mounted. (**B**) A water dipping objective adaptor (here mounted on a water immersion objective) allowed imaging of cells suspended upside-down. The benefit of this geometry is that the excitation and emitted light do not pass through the carbon support which otherwise would reduce image SNR. (**C**) The most user-friendly arrangement makes use of a commercially available microscope slide. The grid did not move relative to the slide and cell medium (as is the case in (**B**) and figure 4.13), which reduced the likelihood of it being damaged during manipulation. Insets shows the movement of plunging tweezers that lifted the grid from the slide and allowed the tweezers to be removed safely.

Physical and chemical properties of support film change cell behaviour

Initial FM imaging of cells grown on EM grids indicated that pre-treatment of the support film was critical for the experimental outcome. For example, the standard protocol involved coating with 10 µg.ml^{-1} fibronectin in poly-L-lysine. However, this resulted in virus binding to the carbon film, meaning that it was impossible to distinguish cell binding events (Figure 4.15). This interaction was likely mediated by electrostatic interaction between the net-negative surface of virions and the positively-charged polymer. Moreover, it is conceivable that there was a residual leaching of poly-L-lysine from coated surfaces, which would artificially boost virus-cell binding in a manner similar to, for example, polybrene (Davis *et al.*, 2004). Additional undesirable effects of cell growth on EM grids was that they tended to cluster around the metal support bars. This was attributed to the cells' preference for stiffer surfaces and tendency to avoid growing over holes in support bars. This effect is illustrated by the orientation of filopodia in orthogonal, rather than centripetal directions around a cell (Figure 4.15).

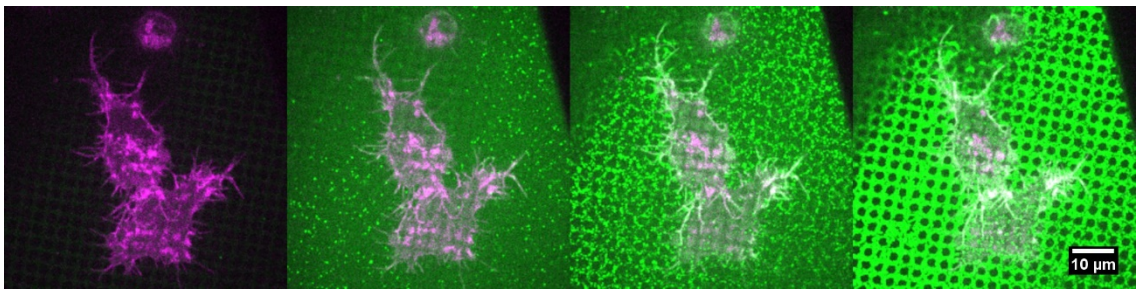


Figure 4.15 Virus particles bind strongly to poly-L-lysine coated carbon film. Shown are confocal sections of XCmCAT cell attached to holey-carbon film coated with a mixture of poly-L-lysine and fibronectin before and after addition of MLV YFPenv particles. Signal from the red channel (mApple) is shown in magenta, green (YFP) signal is shown in green. Frames acquired 1 min before and 0.1, 0.5 and 1 min after virus addition, are ordered from left to right.

This led to the search for an optimal EM grid coating for cell culture. One of the first developments was the use of graphene oxide-coated grids, which is described in chapter

3 (section 3.4, Materials and methods). This also led to the preferential use of lacey carbon film due to its higher hole-to-carbon ratio. Lacey carbon was not used previously specifically because of this reason, as it negatively affected cell growth. Graphene oxide coating created a mostly continuous surface, which promoted cell adhesion. There was a further improvement when a thin layer of continuous carbon was deposited on lacey carbon film, which was attributed to an increase in rigidity compared to graphene oxide sheets. This observation was not quantified due to a lack of a reliable reporter assay.

From ECM proteins to covalent functionalisation

Another variable that was explored was the type of polymer or ECM protein coating used to promote cell adhesion. There is a large ongoing field of research with publications several decades into the past focused on studying the effect of cell adhesion materials (often described as extracellular matrix, ECM) on cell growth. One of the outcomes was the use of petrochemical polymers as growth substrates due to their superior performance, even compared to whole organism-derived ECM proteins. Since the majority of surfing experiments were performed on ibidi microscopy slides, it was hypothesised that replicating their surface chemical composition on EM grids would result in an improvement in cell behaviour. There is little concrete data on the specific chemical composition of ibidi slides (to the author's best knowledge), but the hydrocarbon polymer surface is reportedly treated with atmospheric plasma, which renders it hydrophilic. Carboxylic acid termination was shown to promote cell adhesion (Brandley *et al.*, 1987) and research conducted by Lockett *et al.* (2009) and Colavita *et al.* (2009), together with personal communication with Lloyd Smith and Matthew

Lockett, indicated that amorphous carbon surfaces can be covalently functionalised by plasma treatment followed by UV light-induced reaction with enoic acids. The presence of carboxylic acid groups could be detected (after extensive washing) using a colour-change reaction on EM grids that were glow-discharged and incubated in 9-decenoic acid in the presence of UV light, but not on grids that were kept in the dark.

The effect of EM grid covalent carboxylic acid functionalisation ("carboxylic coating") on cell adhesion, morphology and virus surfing was compared to coating with fibronectin, collagen I, collagen IV and laminin. The most consistent effect observed across the different coatings was that cells grown on laminin-coated grids attached, almost exclusively, to the metal support bars (Figure 4.16). Cells on fibronectin- and carboxylic-coated grids generally had longer protrusions and were more willing to spread over grid squares (as opposed to the metal support) compared to the other ECM proteins. A small number of cells engaged in virus surfing could be found on all types of coating, with none performing substantially better than others. Fibronectin and carboxylic coating (using 9-decenoic or 4-pentenoic acid) were compared on amorphous carbon-coated glass slides in order to eliminate the unpredictable variable of the EM grid topology. The ratio of rounded-up to flat cells grown on this surface was compared, using two related XC cell lines expressing mCAT-1 labelled with mApple or mCherry (Figure 4.16). However, there was a significant difference in morphology between the two cell lines on ibidi slides (used as control), preventing any conclusions to be drawn from this. This result illustrates the difficulty evaluating the high-level behaviour of extremely complex systems, like eukaryotic cells. Both types of coating were used for subsequent live-CLEM experiments, without any apparent difference between them.

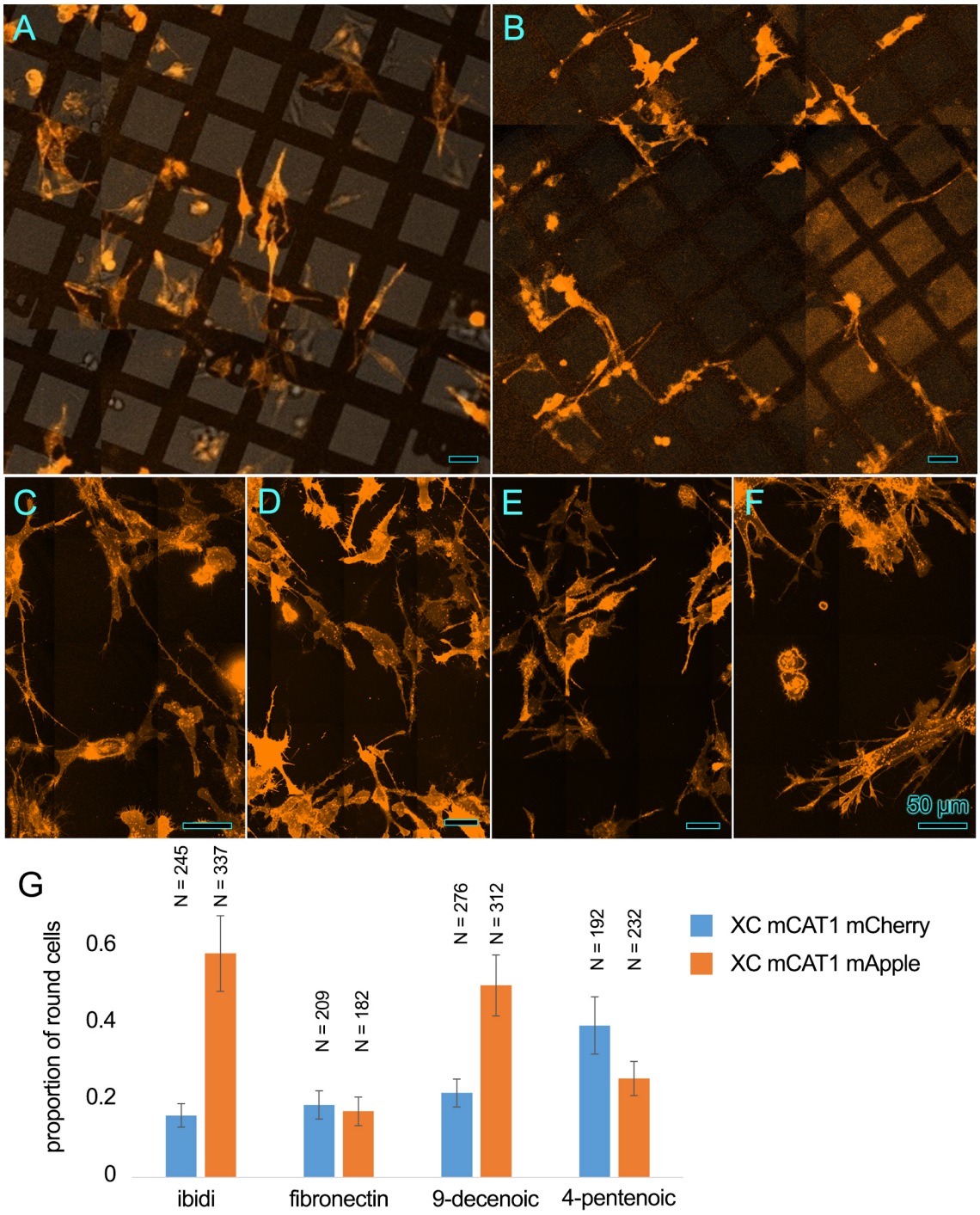


Figure 4.16 Cell behaviour is strongly affected by the surface chemistry of EM grids. (**A**) XCmCAT cells grown on fibronectin coated holey-carbon support were equally likely to adhere to the metal support bars or the grid squares in between, but they showed a clear preference for the metal bars when coated with laminin (**B**). XCmCAT (expressing mCAT-1-mCherry) cells were grown on ibidi slides (**C**) or amorphous carbon-coated glass slides that were surface treated with fibronectin (**D**), 9decenoic acid (**E**), or 4-pentenoic acid (**F**). (**G**) The ratio of cells with an undesirable rounded-up morphology expressed as the fraction of all cells for each of the conditions shown in (**C**-**E**). Blue and orange bars correspond to XC cells stably expressing mCAT-1-mCherry or mCAT-1-mApple, respectively. It is unlikely that the choice of fluorescent protein label affects the cell morphology, instead it highlights the large heterogeneity in cell morphology. The average number of cells counted for each condition was 248 +/- 61; the number of cells (N) in each condition is shown above each bar. Error bars represent standard deviation of Poisson distribution. Scale bars represent 50 µm.

Blotting causes extensive structural changes of cellular specimens

XCmCAT MLV-YFPenv virus surfing live-CLEM experiments were performed using the live-CLEM stage on lacey carbon grids overlaid with continuous carbon and coated with fibronectin or carboxylic acid. FM time-lapse Z-stacks of several cells at a time were acquired. Tweezers with mounted grids were removed from the FM stage upon identification of a promising surfing event. Gold fiducial particles were added, and excess liquid was blotted before plunge-freezing. Cryo-FM imaging was then performed in order to facilitate correlation to EM data. Comparison of live-cell FM, cryo-FM and low-magnification EM data showed large scale changes in cell morphology and shape in all areas where the ice was thin enough for the EM imaging. The term "cell shape" is used to distinguish the general flattening and physical damage caused by the medium surface tension from morphological changes resulting from cytoskeletal rearrangement. Medium-magnification montages were taken of cells with the least changes in shape; figure 4.17 shows a representative example. Overlay of all three image types indicated that long protrusions observed in the last frame of live-cell FM were either damaged or retracted in the vitrified specimen. No virus particles interacting with cells could be found. This set of experiments performed with live-CLEM stage supported previous observations performed with U2OS CAR-mCherry cells and adenovirus, showing large-scale changes in cell shape induced, presumably, by blotting. Correlation between live-cell FM and EM data might still be possible, but this would probably require a completely automated system for specimen manipulation in order to reduce the gap time to less than 5 s.

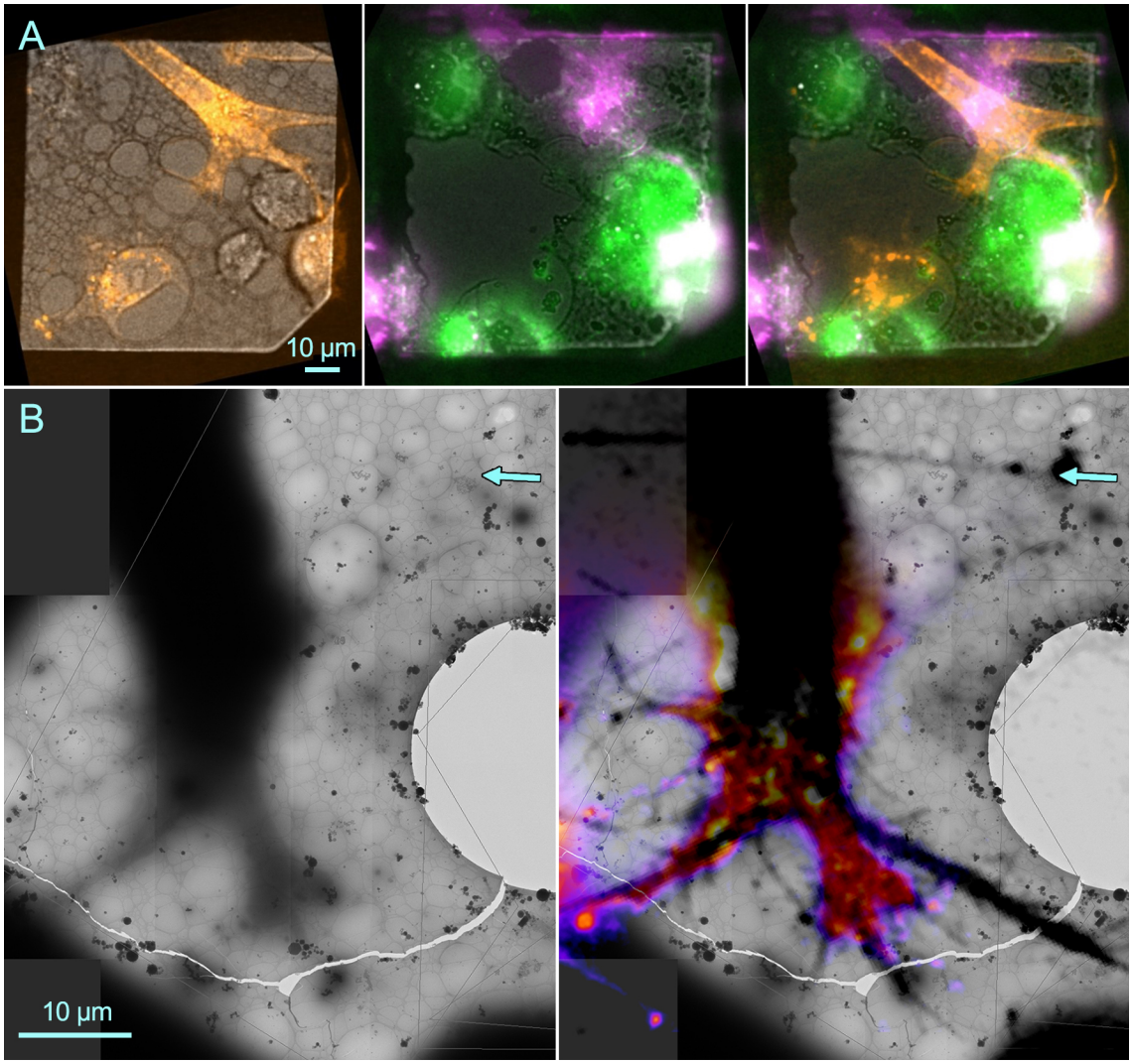


Figure 4.17 Large-scale structural changes occur during specimen preparation. (**A,** left) The last frame of live-cell confocal time-lapse acquired before specimen preparation for plunge-freezing showing XCmCAT cells grown on lacey-carbon grids overlaid with continuous carbon. The image is an overlay of (underfocused) transmitted light (greyscale) and the red fluorescent channel (orange). The green (YFP) channel was acquired but it is not displayed for clarity. (**A,** middle) An overlay of wide-field transmitted light (greyscale), red (magenta) and green (green) fluorescent channels of the same area acquired under cryogenic conditions after vitrification. (**A,** right) Combination of left and middle panels. In addition to breakage of a part of the carbon support, all cells in this area were substantially flattened compared to the RT image acquired 30 s prior to plunge-freezing. (**B**) A grid square containing a cell with less pronounced structural changes was imaged in EM; a montage acquired at 9300x nominal magnification (left panel) was overlaid with the red channel of cryo-fluorescence data (fire) and the last frame of live-cell imaging (black shadow, right panel). There were a large number of long (longer than 5 µm) filopodia observed in RT that are all missing after vitrification. A surfing event was observed during live cell imaging on a very long retraction fibre visible on the top right corner of the right panel (cyan arrow), but neither it nor the surfing virus could be seen in cryo-FM or EM.

Implications of blotting-induced damage on EM of cellular specimens

The extent of structural changes observed even with a very short period (30 s) between removing cells from cell culture medium and vitrification is alarming, but probably not damning for EM of cellular specimens as a whole. The majority of studies in this field focuses on structures on the nanoscopic scale, which is unlikely to be affected by the microscopic structural changes induced by blotting. Furthermore, it is possible to find cells in EM that have (at least superficially) healthy-looking protrusions, when the choice for the region of observation is not restricted by correlation with a more limited FM data set. This suggests that blotting-induced cell damage differs from region to region and between individual cells.

Nevertheless, the data presented here show a clear example of the structural damage that can be induced by specimen preparation, and indicate a need for better, more gentle workflows for EM.

Plunge-freezing results in areas of local vitrification

Live-CLEM grids were pre-screened for vitrification in EM prior to cryo-FM imaging. Medium magnification images are generally sufficient to identify regions with crystalline ice due to the appearance of black and white Moiré patterns, but diffraction screening is a valid alternative. All of the screened grids had patches of crystalline ice covering ~ 10-60 % of the grid area (Figure 4.18). It is unlikely that this was a result of devitrification, which typically affects the whole grid. It is rather the effect of incomplete

vitrification resulting from the surface of liquid ethane-propane parting as the grid splashes into it (Kasas *et al.*, 2003). This creates a gas cavity around the grid resulting in a lower rate of heat transfer, as it is not directly in contact with the cryogen. It is worth nothing that the "local vitrification" phenomenon was not observed on EM grids containing purified protein or virus particles. Similar to cells damaged by blotting, local areas of crystalline ice are not a limiting factor where the choice for data acquisition is not restricted by the need for correlation. An obvious solution to this problem would be to use high-pressure freezing, but this requires the specimen to be thinned for EM imaging. An increase in cooling rate with higher speed of specimen submersion was reported previously (Ryan *et al.*, 1987). Considering that only parts of grids were not vitrified, this suggests that a small increase in the rate of vitrification could be sufficient to prevent this effect from occurring.

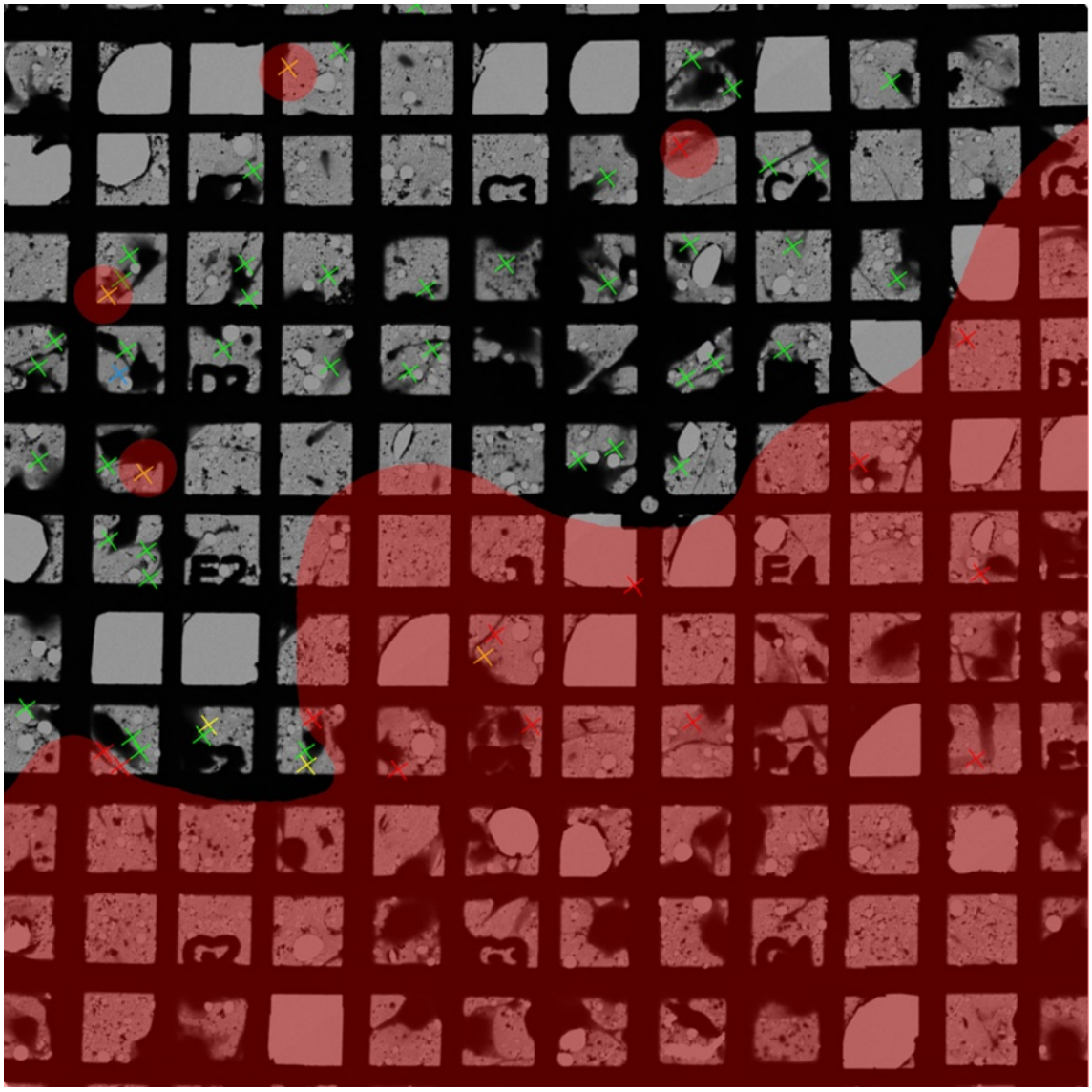


Figure 4.18 Grids with adherent eukaryotic cells were rarely fully vitreous. Shown is a low magnification montage of a live-CLEM grid that was screened for signs of crystalline ice by electron diffraction. Green crosses indicate vitreous areas, red and yellow crosses were crystalline. An approximate extent of non-vitreous areas was drawn in transparent red.

Future directions

Very little progress has been made towards understanding of virus surfing, or surfing in general. The most sensible course of action in this direction would be to invest resources in determining what proteins are involved in virus surfing. A detailed knowledge of the players involved would allow a more reductionist structural approach to be used, or to identify clues that might facilitate surfing to be identified in cET.

The use of live-CLEM did not result in observations of virus surfing events, but it highlighted the degree of structural changes that take place during blotting and specimen preparation in general. There is clearly a need for the development of much more sophisticated approaches to ensure cells are vitrified in a physiologically relevant environment. The absence of a blotting step and a more effective vitrification makes high-pressure freezing an attractive technique for this purpose, but its routine use would require an efficient and artefact-free sectioning technique that currently does not exist.

The expected advent of propane-jet based freezing might provide in the future an alternative worthwhile to explore.

4.3 Materials and methods

Cell culture, EM data acquisition and processing was performed as described in chapter 3, section 3.4, Materials and methods, unless otherwise specified.

Generation of XC cell lines stably expressing fluorescent mCAT-1 or CAR

The mApple synthetic clone (Shaner *et al.*, 2008) was synthesized and cloned by GENEWIZ at the 3' end (C-terminus) of mCAT-CFP (Sherer *et al.*, 2003) using 3' MluI and 5' SbfI sites, thus replacing the CFP sequence. Plasmid containing C-terminal fusion of CAR-mCherry and U2OS cells were a gift from Harald Wodrich (Bordeaux University, Bordeaux, France). XC cells were a gift from Walther Mothes (WM, Yale, New Haven, Connecticut, USA) or Quentin Sattentau (University of Oxford, Oxford, UK). XC cells were transfected with an mCAT-1-mApple, mCAT-1-mCherry or CAR-mCherry plasmid using

X-tremeGENE HP DNA Transfection Reagent (Sigma) as per manufacturer's instructions. Cells were split after 24 h to obtain well-separated single colonies and selection was performed using 600 $\mu g.ml^{-1}$ G-418 (Sigma) after additional 24 hours. Fluorescent colonies were observed after 8 days at 37°C; these were diluted into 24-well plates to obtain single colonies per well, which were then expanded and stored at -70°C.

Preparation of MLV virus stocks

Live MLV virus stocks were prepared by transfecting HEK293T cells with a pcDNA3 vector containing gagpol, gag, env-YFP sequences (Sherer *et al.*, 2003) (These plasmids were a gift from WM) using Fugene Xtreme Gene (Roche) as per manufacturer's instructions. The cell supernatant was harvested after 5 days, cleared by centrifugation at 3000 x g for 5 minutes and stored at -70°C. The live-virus stock was used to infect DFJ8 (DF-1 chicken cells expressing mCAT-1; DFJ8 cells were a gift from WM) in a T-25 flask (Cellstar) which was expanded to 6 T-175 flasks. Initial virus harvest was performed after 3 days, followed by 2 more harvests every 2 days. The virus-containing supernatant was precleared at 3000 x g for 30 minutes and centrifuged through a cushion of 15% sucrose in 20 mM HEPES pH 7.5, 150 mM NaCl and 3.6 mM $CaCl_2$ (1/6 of total centrifuge tube volume) at 100 000 x g for 1 h at 4°C. The supernatant was aspirated, and the virus pellet was allowed to dissolve overnight at 4°C in a small volume of 20 mM HEPES pH 7.5, 150 mM NaCl and 3.6 mM $CaCl_2$. The concentrated virus (0.5 ml) was then centrifuged at 15,000 x g for 1 minute to remove large clumps and passed through Capto^{TM} Core 700 1 ml pre-packed column (GE Healthcare) before snap-freezing in liquid N_2 and storage at -70°C, and directly before use.

Virus surfing experiments

FM virus surfing experiments were performed with Cell Observer Z1 inverted microscope (Zeiss) equipped with CSU-X1 Filter Wheel and Spinning Disk (Yokogawa), Evolve 512 Delta EM-CCD camera (Photometrics) and 405, 488 and 564 nm excitation laser lines with 63x C-Apochromat NA 1.2 UV-VIS-IR water-immersion objective (Zeiss) or 100x Plan Apochromat NA 1.4 oil-immersion objective (Zeiss). Data acquisition was performed with ZEN Blue (Zeiss); images were then processed with Fiji (Schneider *et al.*, 2012). Single virus tracking (Figure 4.5, C) was performed using TrackMate ImageJ plugin (Tinevez *et al.*, 2017); virus tracks were ploted using Matplotlib (Hunter, 2007). All live-cell microscopy was performed at 37°C. Cells were grown on 8-well microscope slides (ibidi) in FluoroBrite DMEM (Thermo) containing 200 mM GlutaMax and 10% FBS and were kept at 37°C with minimal temperature fluctuations at least 1 h before imaging. MLV YFPenv was diluted 1 in 5 in 50-µl of pre-warmed cell medium before it was added to cells; the cell medium was then mixed by pipetting to achieve even distribution of virus particles. Alexa488 labelled adenovirus was a gift from Harald Wodrich; it was shipped on dry ice and stored at -70°C. Adenovirus stock was diluted 1 in 100 before addition to cells.

Specimen preparation for optimisation of cell adhesion

Holey or lacey carbon gold grids overlaid with GO (Quantifoil, EM resolutions) were coated with 50 $\mu g.ml^{-1}$ solutions of collagen type I from rat tail, collagen type IV from human placenta, laminin or bovine fibronectin (Sigma) and washed with PBS before cell seeding. Covalent coating with carboxylic acid was performed as follows: Grids were

placed in a Hellma quartz SUPRASIL cell (Thermo) with 0.1 mm path and submerged in a thin layer of 9-decenoic or 4-pentenoic acid immediately after glow-discharging. They were then illuminated with a hand-held UV source overnight, followed by extensive washing with methanol, ethanol and ultrapure water. Colour change reaction for detection of carboxylic acids was adapted from Agarwal (2006) and Johar *et al.* (1971). A solution of 0.01% acriflavine (Sigma) was added to 10 $mg.ml^{-1}$ solution of sodium nitrite and incubated at 90°C for 5 min with either a grid that had been submerged in 9-decenoic acid and treated with UV, or a grid that was kept in the dark overnight as a control. The solution containing the UV-treated grid changed colour from yellow to orange, where the control sample stayed yellow. A light absorbance scan between 250 and 700 nm performed with NanoDrop (Thermo) indicated a substantial decrease in absorbance at ~ 440 nm of the treated grid solution compared to control. A brown residue could be observed on the UV treated grid in light microscopy. For comparison of covalent and fibronectin coating, glass slides were glow discharged extensively before coating with ~ 10 nm of amorphous carbon. These slides were then coated in the same manner as EM grids.

Specimen preparation for EM

EM grids (holey carbon, Quantifoil) used to collect tomograms of MLV and adenovirus binding events were prepared as described in chapter 3.4 materials and methods. For live-CLEM experiments, gold finder lacey carbon grids (EM resolutions or Agar) were overlaid with a thin layer of amorphous carbon that was deposited on silica using Emitech K950X (Quorum). These grids were glow-discharged and coated with

fibronectin or carboxylic acid. Cell seeding was performed on 2x9-well co-culture slides (ibidi). Parts for the live-CLEM stage prototype were designed to fit an I-3091 universal insert (ASI) in sketchup or AutoCAD (Trimble INC., Autodesk) and manufactured by the Department of Physics Mechanical Workshop, University of Oxford. For FM imaging, the wall on one end of a fresh slide was removed to allow plunging tweezer access from the side (Figure 4.14).

5 Discussion

The data presented in this thesis is a mixture of experiments and driven by them the exploration of possible ways to overcome the current challenges of studying complex biological systems by cET. The overall conclusion could be condensed into a single statement: cET, in combination with complementary methods, has the potential to become the primary technique for structural cell biology. However, there are many challenges that need to be addressed before that can happen. Chapter 3 described the application of cryo-SOFI, which represents an important step towards correlative super-resolution cryo-FM and EM. Nevertheless, for many applications it is not the resolution of the cryo-FM data that is the limiting factor. It is oftentimes enough to have a rough indication of the location of a rare event, such as adenovirus escaping an endosome. In these cases, it is sufficient to achieve ~ 500 nm resolution in order to direct tomogram acquisition. Instead, the main setbacks are usually due to the inability to reproduce biological phenomena on EM grids, poor vitrification, specimen breakage and ice contamination during transfer steps. It should be noted, that the extent of poor vitrification reported in this thesis is unprecedented in the scientific record (to the best of the author's knowledge). It is possible that this is the result of a bias towards positive results, which is a common phenomenon in scientific literature. Alternatively, it would highlight a high degree of incompetence on the author's part.

Specimen transfer and the associated ice contamination and specimen breakage are engineering problems whose solution depends chiefly on sufficient demand in order to create a financial incentive for cryo-EM and cryo-FM hardware manufacturers. It is unlikely that there is a single procedure that could solve all problems associated with

cell behaviour on grids, but it is possible to aim towards the most physiological conditions and the least perturbations possible. Cell adhesion is an important factor of cell physiology since focal adhesions are both points of attachment to the extracellular matrix and signalling hubs affecting gene expression. Presented within the Materials and methods sections throughout this thesis are ways of promoting cell adhesion through modifying the EM grid topography and chemistry. Unfortunately, these could be considered as no more than attempts to patch a broken system since the most amount of damage is performed at the very end of the specimen preparation process, during blotting of cell medium that precedes vitrification.

Vitrification of aqueous solutions is exceedingly difficult; it was even considered thermodynamically impossible (Dubochet, 2012) before it was achieved by Dubochet and McDowall (1981). The plunge-freezing approach became the primary way of preparing cryogenic specimens. Only very thin aqueous specimens can be vitrified by submersion into a cryogenic coolant due to the very low thermal conductivity of water, hence the need for blotting. Heat transfer during plunge-freezing is reduced even further due to a gas cavity forming around the EM grid as it splashes into the liquid surface (Kasas *et al.*, 2003) but this is arguably an engineering problem that could be solved. It will be much more difficult to ensure cells are kept intact during this procedure. High-pressure freezing was mentioned as a potential alternative to plunge-freezing, but its use is associated with a requirement for specimen thinning. An interesting route could be to grow cells in a microfluidics device in order to achieve the minimum possible volume of liquid around cells. It might be feasible to plunge-freeze this device, provided it is sufficiently small and made from a thermally conductive material. Of course, the main question is how one liberates the fragile specimen that is

fused to the microfluidics device to enable imaging. Clearly, there are possible solutions that could and might be explored with the increasing interest for cET in recent years.

Comparing HSV-1 gB data processing strategy to published SVA maps

Presented in chapter 1 of this thesis is a structure of HSV-1 gB in putative pre-fusion conformation at 9 Å resolution. Compared to current EMDB depositions, this represents the highest resolution SVA map that is not an HIV CA (capsid) lattice or other type of regular protein array (Figure 5.1). While there is an undeniable benefit to achieving maps with higher resolution, it does not necessarily correlate with the quality of science performed nor the amount of information that can be extracted from it. Nevertheless, there are certain scientific queries that can only be answered with sufficiently high-resolution data. In the case of HSV-1 gB, achieving sub-nanometre resolution was necessary for unambiguous domain assignment because of possible inter-domain rearrangements that occur in the pre- to post-fusion conformation transition. Notably, at 11 Å the fit of domains was not yet unambiguous and still allowed for domain I being fitted differently and the fusion loops pointing away from the membrane with similar confidence as a fit with domain I the other way around. The SVA map resolution was arguably insufficient to fully explain how the H516P mutation stabilises the gB short form. The question remains, whether the domain 3 helices break or bend at that region, or are there more subtle, unexpected effects of this substitution.

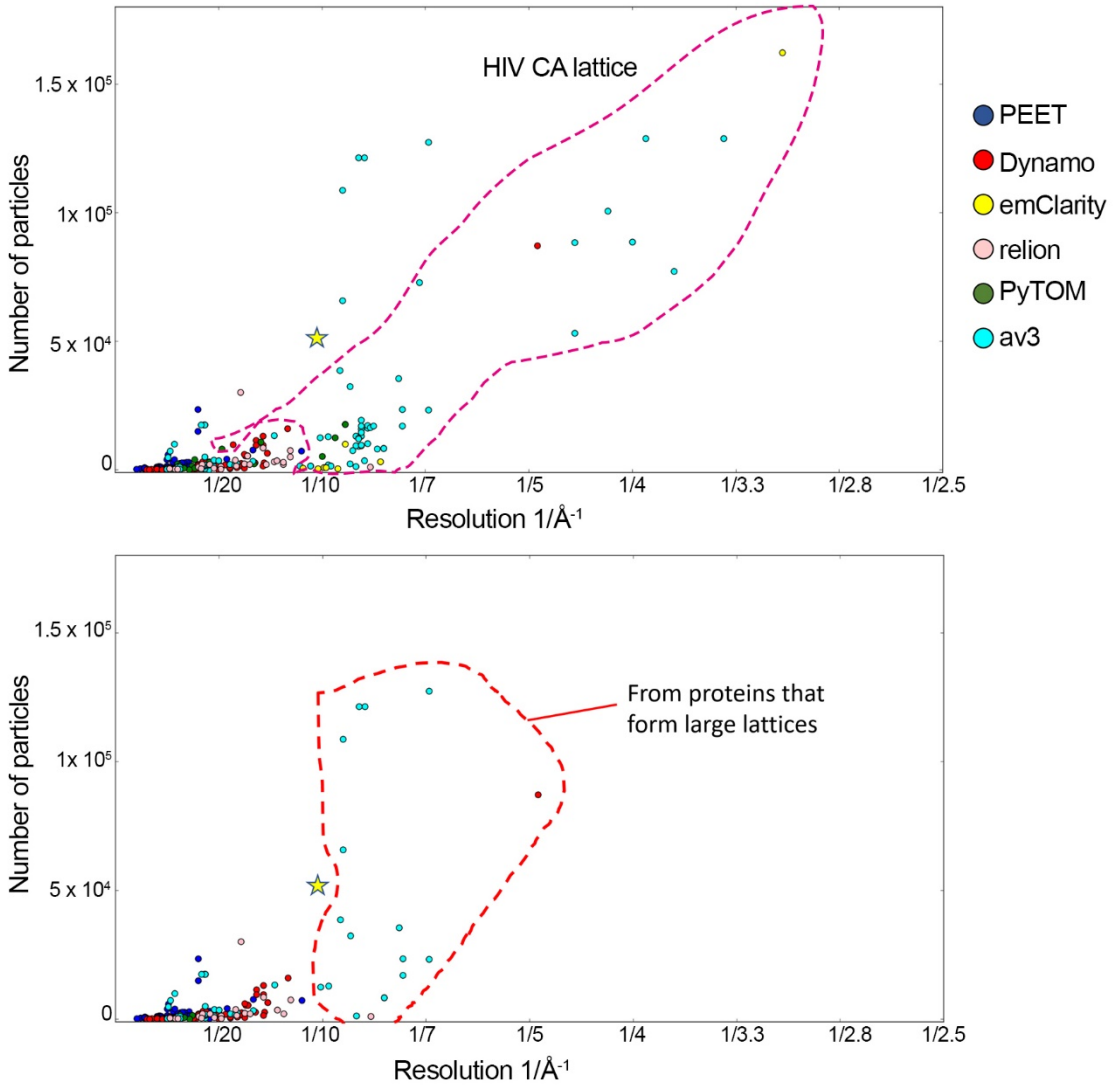


Figure 5.1 Exaggerating one's greatness. Shown are numbers of asymmetric units used for the final reconstruction of EMDB entries plotted as a factor of the reported resolution. The upper and lower plots are equivalent, but entries of HIV CA lattice were removed in the lower plot. Each point has been additionally colour-coded by the SVA program used. The (unpublished) SVA map of HSV-1 gB presented in Chapter 1 of this thesis is represented by a star. Source: EMDB, Daven Vasishtan.

It is worthwhile to evaluate possible factors that contributed to achieving higher resolution over previous studies. Firstly, the number of particles used for the final reconstruction is undeniably a significant factor. SVA is used to study complex specimens where more streamlined methods, such as X-ray crystallography or single-particle cryo-EM are not appropriate. This corresponds to more challenging specimen preparation and fewer number of particles that can be extracted. The

heterogeneous nature of complex specimens also contributes to an increased difficulty with particle alignment and classification. Thickness of specimens correlates strongly with the maximum resolution that can be obtained due to an increased number of inelastic scattering events or simply more density obscuring the particle of interest. Approximately 56,000 particles (presumed gB trimers) were manually picked in tomograms containing gB vesicles. A large proportion of these converged onto the same coordinates during initial iterations of SVA alignment and were filtered by proximity to other particles. Crude filtering by the cross-correlation coefficient was used to remove extreme outliers. These steps reduced the number of particles to ~ 30,000. In addition to systematic particle cleaning, manual removal of particles in subsequent steps resulted in ~ 15,000 particles, corresponding to ~46,000 asymmetric units in the final reconstruction and a 73% reduction from initial numbers. It is worth noting that the manual cleaning step was a stand-in for a lack of an adequate algorithm that could deal with the heterogeneous size, shape and density of gB vesicles in the tomograms used. Substantial reduction of particle numbers is common, but not always reported in publications involving SVA. For comparison, Zeev-Ben-Mordehai *et al.* (2016) removed only 20% of initial number of particles.

One of the initial aims was to explore the dependence of resolution on electron fluence per tilt. However, this type of analysis was not appropriate while trying to determine an unknown protein structure and was abandoned. This resulted in a final data-set consisting of tilt series collected with total fluence between ~ 90 and 225 $e^{-}A^{2}$. Turning to the EMDB for more data, there seems to be a positive correlation between the electron fluence per tilt and achieved resolution (Figure 5.2). In the author's opinion, there is a clear benefit of using up to 7 $e^{-}A^{2}$ per tilt, provided that there are no extreme

signs of radiation damage (bubble formation) in the majority of tilts. Averaging ~ 1000 particles from the highest-fluence tomograms resulted in a fast convergence towards a symmetrical density and features (subjectively) consistent with 10-20 Å resolution, indicating that the low-resolution of "damaged" tilts are beneficial for (initial) SVA alignment. The use of up to 7 $e^{-}A^{2}$ per tilt results in the first ~ 40 $e^{-}A^{2}$ being concentrated to ± 9 ° of stage tilt where the apparent increase in specimen thickness (~ 15 %) is negligible. The higher tilts with a higher accumulated radiation dose were removed at later stages of gB SVA. The expected (but unconfirmed) effect was that the relative weight of high-resolution frequencies was increased, and the effect of warping decreased. The rationale behind refining only translation and not rotation at this stage was two-fold. There was a clear tendency towards model bias when rotations were refined and the angular change of individual particles due to warping should be negligible relative to their translation. This means that after finding the initial rotation of particles using primarily low-resolution data, it should be sufficient to look for the less-damaged higher resolution positions.

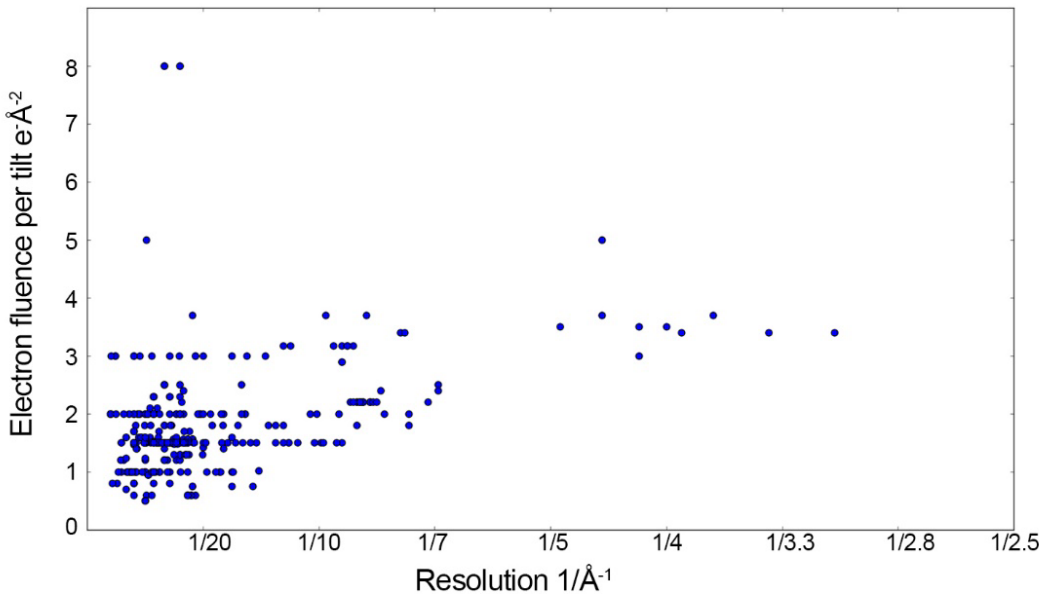


Figure 5.2 High-resolution data is best served fried. Show is the electron fluence per tilt of EMDB entries plotted as a factor of the reported resolution. There is a general positive relationship between resolution and higher fluence, but causality remains tentative due to the large diversity of specimens, particle numbers of final averages and methodologies.

There might even be a benefit to acquiring single high-fluence projection images (~ 40 $e^{-}A^{2}$) followed by a "conventional" tilt series at the same position. This would enable warping correction to be performed in 2D and allow more precise defocus estimation. This "hybrid approach" has been explored, for example, with Tabaco mosaic virus, where particle orientation (essential helical parameters) were determined by SVA followed by single-particle averaging (unpublished data from Misha Kudryashev's research group). It remains to be seen whether this can be done with non-symmetrical specimens. An ideal-case scenario for pleomorphic specimens would involve density subtraction of structures overlapping with the particles of interest. An implementation of this concept is being explored by Achilleas Frangakis's research group in a program called Artiatomi (Achilleas Frangakis, personal communication). This approach would have the added benefit of reducing the computational "cost" through the reduction in dimensionality. The approach in this study was much less sophisticated: The high tilts were simply replaced with blank images in order to ensure that the resulting tomograms matched the original, all-tilt data. A side-effect of this approach might be an increase in aliasing artefacts (Figure 5.3). This might explain the substantial increase in resolution achieved by switching 2x binned tomograms for 1x binning (Chapter 1, Figure 1.12) and partially why the final reconstruction resolution reached only ~ 1/3 of the Nyquist frequency.

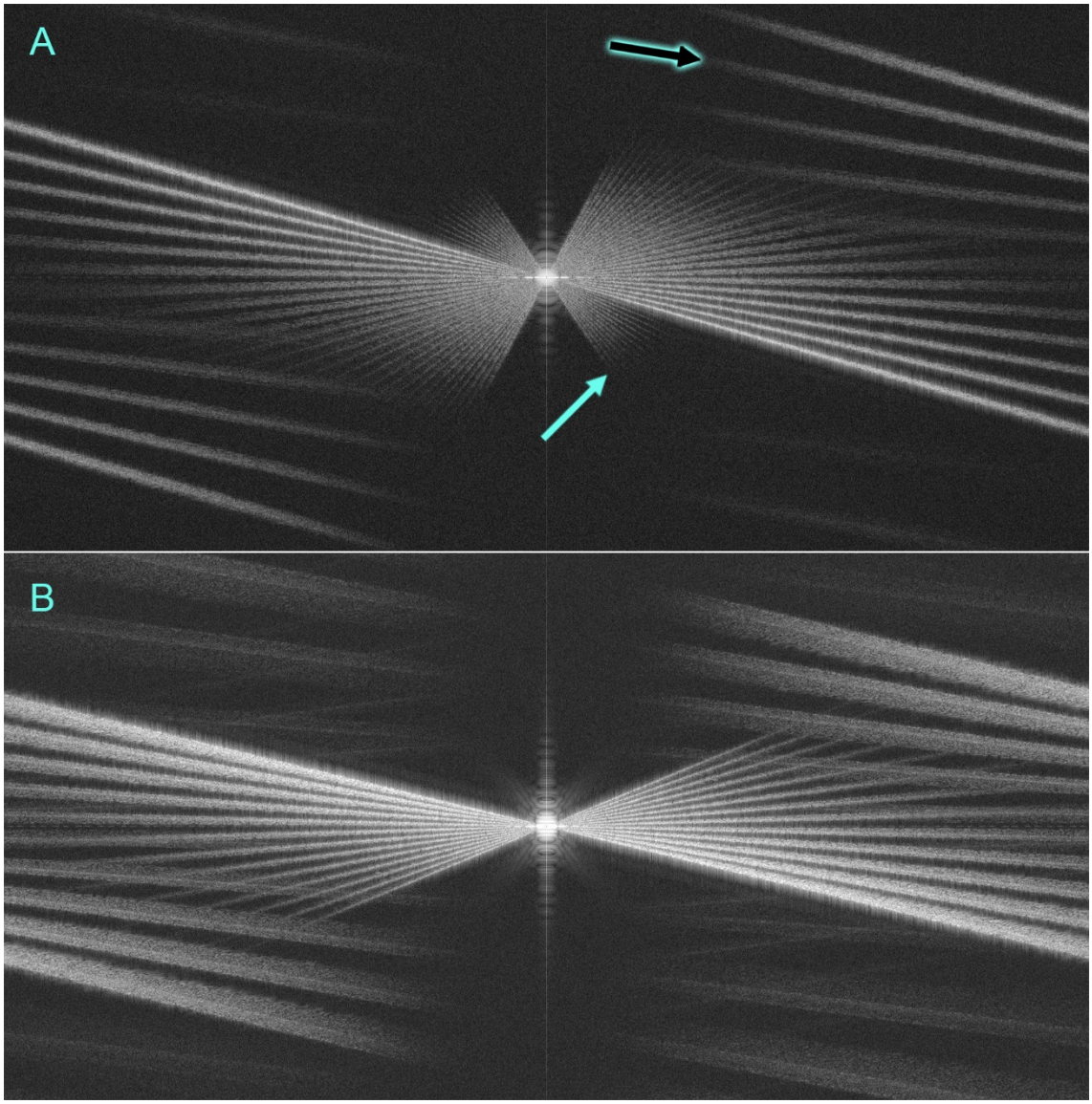


Figure 5.3 Everyone agrees that aliasing is bad. Shown is an orthogonal view of a gB vesicle tomogram power spectrum along tomogram tilt axis. (**A**) All-tilt tomograms, (**B**) low-tilt tomogams. The effect of dose-weighting is apparent on the reduced weight of higher tilts at high frequencies, indicated with cyan arrow. The effect of aliasing can be seen as rays (black arrow). The weights of these rays are attenuated at low frequencies due to R-weighting during tomogram reconstruction.

An alternative approach to compensating for specimen warping is to keep the whole tilt series and attempt to perform "motion correction" through gold or sub-volume fiducial markers (Fernandez *et al.*, 2018, Himes and Zhang, 2018), which is described in chapter 2. The motivation for writing Flexo initially came from a need to increase contrast in rare observations of virus-cell interaction events in order to allow the direct interpretation of the EM density. Preliminary data from Dimitry Tegunov in 2017

(Personal discussion) indicated that tomogram unwarping was possible, but there was no publicly available software that could do it. The development of Flexo then became intertwined with sub-volume averaging of gB, where it would be of clear benefit. However, the results of using early version of Flexo on gB vesicle tomograms were not encouraging. The suspected reason for this was the small size of gB and the pleomorphic shape of membrane vesicles. Membrane vesicles are not reliable densities for unwarping because there is no prior information about their shape. Different geometries used for reconstruction of tomograms resulted in different shapes of membrane vesicles, most looking equally plausible. Nevertheless, this direction remains worth exploring due to the large number of specimens (e.g. enveloped viruses) that would benefit from it.

There were two programs for tomogram unwarping published in 2018. The approach by Fernandez *et al.* (2018) was robustly implemented, but it was reliant on a large density of gold fiducial markers. emClarity, published as methods paper, (Himes and Zhang, 2018) showed incredible potential by achieving sub-nanometre SVA map of *S. cerevisiae* ribosomes with the same data set that was previously achieved ~ 15 Å resolution (Bharat and Scheres, 2016). A number of laboratories (including the author's) reported difficulties installing and running emClarity despite substantial investment of time (Kay Grünewald, Daven Vasishtan, personal communication). There are currently 6-8 different SVA programs but only 2, PEET and Dynamo, have been widely used in laboratories other than those supported by the respective software developers. It is the author's belief that there is a need for further integration, not fragmentation of software for sub-volume averaging. Existing well documented platforms such as IMOD and PEET have an excellent potential for supporting external development, of which Flexo is an

example. There are now multiple concepts shown to improve resolution of SVA maps, from considering the changes of defocus experienced by individual particles to compensating for specimen warping. A collaborative effort to integrate these features to a single package, or to ensure the interchangeability of inputs and outputs between different packages would be undeniably beneficial to the scientific community.

References

1. Abbe, E. (1873). "Beiträge zur Theorie des Mikroskops und der mikroskopischen Wahrnehmung." *Archiv f. mikrosk. Anatomie* **9**: 413.

2. Agarwal, O. P. (2006). Advanced practical organic chemistry. Delhi, Krishna Prakashan.

3. Al-Amoudi, A., J. J. Chang, A. Leforestier, A. McDowall, L. M. Salamin, L. P. Norlen, K. Richter, N. S. Blanc, D. Studer and J. Dubochet (2004). "Cryo-electron microscopy of vitreous sections." *EMBO J* **23**(18): 3583-3588.

4. Albrecht-Buehler, G. and R. M. Lancaster (1976). "A quantitative description of the extension and retraction of surface protrusions in spreading 3T3 mouse fibroblasts." *J Cell Biol* **71**(2): 370-382.

5. Anderson, P. W. (1972). "More Is Different." *Science* **177**(4047): 393.

6. Ando, T., S. P. Bhamidimarri, N. Brending, H. Colin-York, L. Collinson, N. De Jonge, P. J. de Pablo, E. Debroye, C. Eggeling, C. Franck, M. Fritzsche, H. Gerritsen, B. N. G. Giepmans, K. Grunewald, J. Hofkens, J. P. Hoogenboom, K. P. F. Janssen, R. Kaufman, J. Klumpermann, N. Kurniawan, J. Kusch, N. Liv, V. Parekh, D. B. Peckys, F. Rehfeldt, D. C. Reutens, M. B. J. Roeffaers, T. Salditt, I. A. T. Schaap, U. S. Schwarz, P. Verkade, M. W. Vogel, R. Wagner, M. Winterhalter, H. Yuan and G. Zifarelli (2018). "The 2018 correlative microscopy techniques roadmap." *J Phys D Appl Phys* **51**(44): 443001.

7. Backovic, M., R. Longnecker and T. S. Jardetzky (2009). "Structure of a trimeric variant of the Epstein-Barr virus glycoprotein B." *Proc Natl Acad Sci U S A* **106**(8): 2880-2885.

8. Baker, L. A. and J. L. Rubinstein (2010). Chapter Fifteen - Radiation Damage in Electron Cryomicroscopy. Methods in Enzymology. G. J. Jensen, Academic Press. **481:** 371-388.

9. Baker, L. A., E. A. Smith, S. A. Bueler and J. L. Rubinstein (2010). "The resolution dependence of optimal exposures in liquid nitrogen temperature electron cryomicroscopy of catalase crystals." *J Struct Biol* **169**(3): 431-437.

10. Bentz, J. (2000). "Membrane fusion mediated by coiled coils: a hypothesis." *Biophys J* **78**(2): 886-900.

11. Beveridge, T. J. (1999). "Structures of gram-negative cell walls and their derived membrane vesicles." *J Bacteriol* **181**(16): 4725-4733.

12. Bharat, T. A. and S. H. Scheres (2016). "Resolving macromolecular structures from electron cryo-tomography data using subtomogram averaging in RELION." *Nat Protoc* **11**(11): 2054-2065.

13. Bokori-Brown, M., T. G. Martin, C. E. Naylor, A. K. Basak, R. W. Titball and C. G. Savva (2016). "Cryo-EM structure of lysenin pore elucidates membrane insertion by an aerolysin family protein." *Nat Commun* **7**: 11293.

14. Brandley, B. K., O. A. Weisz and R. L. Schnaar (1987). "Cell attachment and long-term growth on derivatizable polyacrylamide surfaces." *J Biol Chem* **262**(13): 6431-6437.

15. Briggs, J. A. (2013). "Structural biology in situ--the potential of subtomogram averaging." *Curr Opin Struct Biol* **23**(2): 261-267.

16. Buchan, D. W. A. and D. T. Jones (2019). "The PSIPRED Protein Analysis Workbench: 20 years on." *Nucleic Acids Res* **47**(W1): W402-W407.

17. Burckhardt, C. J., M. Suomalainen, P. Schoenenberger, K. Boucke, S. Hemmi and U. F. Greber (2011). "Drifting motions of the adenovirus receptor CAR and immobile integrins initiate virus uncoating and membrane lytic protein exposure." *Cell Host Microbe* **10**(2): 105-117.

18. Burke, D., B. Patton, F. Huang, J. Bewersdorf and M. J. Booth (2015). "Adaptive optics correction of specimen-induced aberrations in single-molecule switching microscopy." *Optica* **2**(2): 177-185.

19. Burke, H. G. and E. E. Heldwein (2015). "Correction: Crystal Structure of the Human Cytomegalovirus Glycoprotein B." *PLoS Pathog* **11**(11): e1005300.

20. Bykov, Y. S., M. Cortese, J. A. Briggs and R. Bartenschlager (2016). "Correlative light and electron microscopy methods for the study of virus-cell interactions." *FEBS Lett* **590**(13): 1877-1895.

21. Bykov, Y. S., M. Schaffer, S. O. Dodonova, S. Albert, J. M. Plitzko, W. Baumeister, B. D. Engel and J. A. Briggs (2017). "The structure of the COPI coat determined within the cell." *Elife* **6**.

22. Chandramouli, S., C. Ciferri, P. A. Nikitin, S. Calo, R. Gerrein, K. Balabanis, J. Monroe, C. Hebner, A. E. Lilja, E. C. Settembre and A. Carfi (2015). "Structure of HCMV glycoprotein B in the postfusion conformation bound to a neutralizing human antibody." *Nat Commun* **6**: 8176.

23. Chang, Y. W., S. Chen, E. I. Tocheva, A. Treuner-Lange, S. Lobach, L. Sogaard-Andersen and G. J. Jensen (2014). "Correlated cryogenic photoactivated localization microscopy and cryo-electron tomography." *Nat Methods* **11**(7): 737-739.

24. Chernomordik, L. V. and M. M. Kozlov (2008). "Mechanics of membrane fusion." *Nat Struct Mol Biol* **15**(7): 675-683.

25. Chowdary, T. K., T. M. Cairns, D. Atanasiu, G. H. Cohen, R. J. Eisenberg and E. E. Heldwein (2010). "Crystal structure of the conserved herpesvirus fusion regulator complex gH-gL." *Nat Struct Mol Biol* **17**(7): 882-888.

26. Colavita, P. E., B. Sun, X. Wang and R. J. Hamers (2009). "Influence of Surface Termination and Electronic Structure on the Photochemical Grafting of Alkenes to Carbon Surfaces." *The Journal of Physical Chemistry C* **113**(4): 1526-1535.

27. Connolly, S. A., J. O. Jackson, T. S. Jardetzky and R. Longnecker (2011). "Fusing structure and function: a structural view of the herpesvirus entry machinery." *Nat Rev Microbiol* **9**(5): 369-381.

28. Cooper, R. S., E. R. Georgieva, P. P. Borbat, J. H. Freed and E. E. Heldwein (2018). "Structural basis for membrane anchoring and fusion regulation of the herpes simplex virus fusogen gB." *Nat Struct Mol Biol* **25**(5): 416-424.

29. Danilchik, M., M. Williams and E. Brown (2013). "Blastocoel-spanning filopodia in cleavage-stage Xenopus laevis: Potential roles in morphogen distribution and detection." *Dev Biol* **382**(1): 70-81.

30. Davis, H. E., M. Rosinski, J. R. Morgan and M. L. Yarmush (2004). "Charged polymers modulate retrovirus transduction via membrane charge neutralization and virus aggregation." *Biophys J* **86**(2): 1234-1242.

31. Dertinger, T., R. Colyer, G. Iyer, S. Weiss and J. Enderlein (2009). "Fast, background-free, 3D super-resolution optical fluctuation imaging (SOFI)." *Proc Natl Acad Sci U S A* **106**(52): 22287-22292.

32. Deschout, H., F. Cella Zanacchi, M. Mlodzianoski, A. Diaspro, J. Bewersdorf, S. T. Hess and K. Braeckmans (2014). "Precisely and accurately localizing single emitters in fluorescence microscopy." *Nat Methods* **11**(3): 253-266.

33. Dubochet, J. (2012). "Cryo-EM—the first thirty years." *Journal of Microscopy* **245**(3): 221-224.

34. Dubochet, J. and A. W. McDowall (1981). "VITRIFICATION OF PURE WATER FOR ELECTRON MICROSCOPY." *Journal of Microscopy* **124**(3): 3-4.

35. Dubochet, J. and J. Lepault (1984). "CRYO-ELECTRON MICROSCOPY OF VITRIFIED WATER." *J. Phys. Colloques* **45**(C7): C7-85-C87-94.

36. Duus, K. M., C. Hatfield and C. Grose (1995). "Cell surface expression and fusion by the varicella-zoster virus gH:gL glycoprotein complex: analysis by laser scanning confocal microscopy." *Virology* **210**(2): 429-440.

37. EMDB Statistics (2019, October 7). "Number of released maps achieving given resolution levels." from https://www.ebi.ac.uk/pdbe/emdb/statistics_num_res.html/.

38. Farabella, I., D. Vasishtan, A. P. Joseph, A. P. Pandurangan, H. Sahota and M. Topf (2015). "TEMPy: a Python library for assessment of three-dimensional electron microscopy density fits." *J Appl Crystallogr* **48**(Pt 4): 1314-1323.

39. Fernandez, J.-J., U. Laugks, M. Schaffer, F. J. B. Bäuerlein, M. Khoshouei, W. Baumeister and V. Lucic (2016). "Removing Contamination-Induced Reconstruction Artifacts from Cryo-electron Tomograms." *Biophysical journal* **110**(4): 850-859.

40. Fernandez, J. J., D. Luque, J. R. Caston and J. L. Carrascosa (2008). "Sharpening high resolution information in single particle electron cryomicroscopy." *J Struct Biol* **164**(1): 170-175.

41. Fernandez, J. J., S. Li, T. A. M. Bharat and D. A. Agard (2018). "Cryo-tomography tilt-series alignment with consideration of the beam-induced sample motion." *J Struct Biol* **202**(3): 200-209.

42. Förster, F., O. Medalia, N. Zauberman, W. Baumeister and D. Fass (2005). "Retrovirus envelope protein complex structure in situ studied by cryo-electron tomography." *Proceedings of the National Academy of Sciences of the United States of America* **102**(13): 4729.

43. Frank, J., A. Verschoor and M. Boublik (1981). "Computer averaging of electron micrographs of 40S ribosomal subunits." *Science* **214**(4527): 1353-1355.

44. Freimuth, P., K. Springer, C. Berard, J. Hainfeld, M. Bewley and J. Flanagan (1999). "Coxsackievirus and adenovirus receptor amino-terminal immunoglobulin V-related domain binds adenovirus type 2 and fiber knob from adenovirus type 12." *J Virol* **73**(2): 1392-1398.

45. Gallagher, J. R., D. Atanasiu, W. T. Saw, M. J. Paradisgarten, J. C. Whitbeck, R. J. Eisenberg and G. H. Cohen (2014). "Functional fluorescent protein insertions in herpes simplex virus gB report on gB conformation before and after execution of membrane fusion." *PLoS Pathog* **10**(9): e1004373.

46. Geissbuehler, S., A. Sharipov, A. Godinat, N. L. Bocchio, P. A. Sandoz, A. Huss, N. A. Jensen, S. Jakobs, J. Enderlein, F. Gisou van der Goot, E. A. Dubikovskaya, T. Lasser and M. Leutenegger (2014). "Live-cell multiplane three-dimensional super-resolution optical fluctuation imaging." *Nature Communications* **5**(1): 5830.

47. Giske, A. (2007). CryoSTED microscopyA new spectroscopic approach for improving the resolution ofSTED microscopy using low temperatureReferees: Prof. Dr. Stefan HellProf. Dr. Christoph Cremer. *Combined Faculties for the Natural Sciences and for Mathematics*. Heidelberg, Germany, University of Heidelberg. **Doctoral thesis** 71.

48. Glaeser, R. M. (2007). Electron crystallography of biological macromolecules. New York; Oxford, Oxford University Press.

49. Goddard, T. D., C. C. Huang, E. C. Meng, E. F. Pettersen, G. S. Couch, J. H. Morris and T. E. Ferrin (2018). "UCSF ChimeraX: Meeting modern challenges in visualization and analysis." *Protein Sci* **27**(1): 14-25.

50. Gould, T. J., M. S. Gunewardene, M. V. Gudheti, V. V. Verkhusha, S. R. Yin, J. A. Gosse and S. T. Hess (2008). "Nanoscale imaging of molecular positions and anisotropies." *Nat Methods* **5**(12): 1027-1030.

51. Grant, T. and N. Grigorieff (2015). "Automatic estimation and correction of anisotropic magnification distortion in electron microscopes." *J Struct Biol* **192**(2): 204-208.

52. Grant, T. and N. Grigorieff (2015). "Measuring the optimal exposure for single particle cryo-EM using a 2.6 A reconstruction of rotavirus VP6." *Elife* **4**: e06980.

53. Hagen, W. J. H., W. Wan and J. A. G. Briggs (2017). "Implementation of a cryo-electron tomography tilt-scheme optimized for high resolution subtomogram averaging." *J Struct Biol* **197**(2): 191-198.

54. Harrison, S. C. (2008). "Viral membrane fusion." *Nat Struct Mol Biol* **15**(7): 690-698.

55. Heldwein, E. E., H. Lou, F. C. Bender, G. H. Cohen, R. J. Eisenberg and S. C. Harrison (2006). "Crystal structure of glycoprotein B from herpes simplex virus 1." *Science* **313**(5784): 217-220.

56. Helenius, A., J. Kartenbeck, K. Simons and E. Fries (1980). "On the entry of semliki forest virus into BHK-21 cells." *The Journal of Cell Biology* **84**(2): 404-420.

57. Hell, S. W. (2009). "Microscopy and its focal switch." *Nat Methods* **6**(1): 24-32.

58. Heumann, J. M., A. Hoenger and D. N. Mastronarde (2011). "Clustering and variance maps for cryo-electron tomography using wedge-masked differences." *J Struct Biol* **175**(3): 288-299.

59. Heymann, J. B. (2019). "Single-particle reconstruction statistics: a diagnostic tool in solving biomolecular structures by cryo-EM." *Acta Crystallogr F Struct Biol Commun* **75**(Pt 1): 33-44.

60. Heymann, J. B. and D. M. Belnap (2007). "Bsoft: image processing and molecular modeling for electron microscopy." *J Struct Biol* **157**(1): 3-18.

61. Himes, B. A. and P. Zhang (2018). "emClarity: software for high-resolution cryo-electron tomography and subtomogram averaging." *Nat Methods* **15**(11): 955-961.

62. Hunter, J. D. (2007). "Matplotlib: A 2D Graphics Environment." *Computing in Science & Engineering* **9**(3): 90-95.

63. Hutchings, J., V. Stancheva, E. A. Miller and G. Zanetti (2018). "Subtomogram averaging of COPII assemblies reveals how coat organization dictates membrane shape." *Nature Communications* **9**(1): 4154.

64. Jeffrey, G. A. (1997). An introduction to hydrogen bonding. New York, Oxford University Press.

65. Joblib. "JobLib: running Python functions as pipeline jobs." from https://joblib.readthedocs.io/en/latest/.

66. Johar, G. S., U. Agarwala and H. S. Sodhi (1971). "New methods for the detection of carboxylic acid groups in organic compounds, with acriflavine." *Talanta* **18**(10): 1051-1055.

67. Johnson, E., E. Seiradake, E. Y. Jones, I. Davis, K. Grunewald and R. Kaufmann (2015). "Correlative in-resin super-resolution and electron microscopy using standard fluorescent proteins." *Sci Rep* **5**: 9583.

68. Jolly, C. and Q. J. Sattentau (2004). "Retroviral spread by induction of virological synapses." *Traffic* **5**(9): 643-650.

69. Jones, E. O., T. Peterson, P. (2001). " SciPy: Open Source Scientific Tools for Python." from http://www.scipy.org.

70. Jones, S., P. van Heyningen, H. M. Berman and J. M. Thornton (1999). "Protein-DNA interactions: A structural analysis." *J Mol Biol* **287**(5): 877-896.

71. Jun, S., H. J. Ro, A. Bharda, S. I. Kim, D. Jeoung and H. S. Jung (2019). "Advances in Cryo-Correlative Light and Electron Microscopy: Applications for Studying Molecular and Cellular Events." *Protein J*.

72. Kasas, S., G. Dumas, G. Dietler, S. Catsicas and M. Adrian (2003). "Vitrification of cryoelectron microscopy specimens revealed by high-speed photographic imaging." *J Microsc* **211**(Pt 1): 48-53.

73. Kaufmann, R., C. Hagen and K. Grunewald (2014). "Fluorescence cryo-microscopy: current challenges and prospects." *Curr Opin Chem Biol* **20**: 86-91.

74. Kaufmann, R., P. Schellenberger, E. Seiradake, I. M. Dobbie, E. Y. Jones, I. Davis, C. Hagen and K. Grunewald (2014). "Super-resolution microscopy using standard fluorescent proteins in intact cells under cryo-conditions." *Nano Lett* **14**(7): 4171-4175.

75. Khatter, H., A. G. Myasnikov, S. K. Natchiar and B. P. Klaholz (2015). "Structure of the human 80S ribosome." *Nature* **520**(7549): 640-645.

76. Kidmose, R. T., J. Juhl, P. Nissen, T. Boesen, J. L. Karlsen and B. P. Pedersen (2019). "Namdinator - automatic molecular dynamics flexible fitting of structural models into cryo-EM and crystallography experimental maps." *IUCrJ* **6**(Pt 4): 526-531.

77. Kohler, F. and A. Rohrbach (2015). "Surfing along Filopodia: A Particle Transport Revealed by Molecular-Scale Fluctuation Analyses." *Biophys J* **108**(9): 2114-2125.

78. Kremer, J. R., D. N. Mastronarde and J. R. McIntosh (1996). "Computer visualization of three-dimensional image data using IMOD." *J Struct Biol* **116**(1): 71-76.

79. Krummenacher, C., F. Baribaud, M. Ponce de Leon, I. Baribaud, J. C. Whitbeck, R. Xu, G. H. Cohen and R. J. Eisenberg (2004). "Comparative usage of herpesvirus entry mediator A and nectin-1 by laboratory strains and clinical isolates of herpes simplex virus." *Virology* **322**(2): 286-299.

80. Kudryashev, M., D. Castano-Diez, C. Deluz, G. Hassaine, L. Grasso, A. Graf-Meyer, H. Vogel and H. Stahlberg (2016). "The Structure of the Mouse Serotonin 5-HT3 Receptor in Lipid Vesicles." *Structure* **24**(1): 165-170.

81. Laquerre, S., R. Argnani, D. B. Anderson, S. Zucchini, R. Manservigi and J. C. Glorioso (1998). "Heparan sulfate proteoglycan binding by herpes simplex virus type 1 glycoproteins B and C, which differ in their contributions to virus attachment, penetration, and cell-to-cell spread." *J Virol* **72**(7): 6119-6130.

82. Leapman, R. D. and S. Sun (1995). "Cryo-electron energy loss spectroscopy: observations on vitrified hydrated specimens and radiation damage." *Ultramicroscopy* **59**(1): 71-79.

83. Lehmann, M. J., N. M. Sherer, C. B. Marks, M. Pypaert and W. Mothes (2005). "Actin- and myosin-driven movement of viruses along filopodia precedes their entry into cells." *J Cell Biol* **170**(2): 317-325.

84. Li, S., I. Rissanen, A. Zeltina, J. Hepojoki, J. Raghwani, K. Harlos, O. G. Pybus, J. T. Huiskonen and T. A. Bowden (2016). "A Molecular-Level Account of the Antigenic Hantaviral Surface." *Cell Rep* **15**(5): 959-967.

85. Lidke, D. S., K. A. Lidke, B. Rieger, T. M. Jovin and D. J. Arndt-Jovin (2005). "Reaching out for signals: filopodia sense EGF and respond by directed retrograde transport of activated receptors." *J Cell Biol* **170**(4): 619-626.

86. Lin, C. H., E. M. Espreafico, M. S. Mooseker and P. Forscher (1996). "Myosin drives retrograde F-actin flow in neuronal growth cones." *Neuron* **16**(4): 769-782.

87. Liu, B., Y. Xue, W. Zhao, Y. Chen, C. Fan, L. Gu, Y. Zhang, X. Zhang, L. Sun, X. Huang, W. Ding, F. Sun, W. Ji and T. Xu (2015). "Three-dimensional super-resolution protein localization correlated with vitrified cellular context." *Sci Rep* **5**: 13017.

88. Lockett, M. R., J. C. Carlisle, D. V. Le and L. M. Smith (2009). "Acyl chloride-modified amorphous carbon substrates for the attachment of alcohol-, thiol-, and amine-containing molecules." *Langmuir* **25**(9): 5120-5126.

89. Martin, P. and S. M. Parkhurst (2004). "Parallels between tissue repair and embryo morphogenesis." *Development* **131**(13): 3021-3034.

90. Mastronarde, D. N. (2003). "SerialEM: A Program for Automated Tilt Series Acquisition on Tecnai Microscopes Using Prediction of Specimen Position." *Microscopy and Microanalysis* **9**(S02): 1182-1183.

91. Matias, V. R., A. Al-Amoudi, J. Dubochet and T. J. Beveridge (2003). "Cryo-transmission electron microscopy of frozen-hydrated sections of Escherichia coli and Pseudomonas aeruginosa." *J Bacteriol* **185**(20): 6112-6118.

92. Matsuura, H., A. N. Kirschner, R. Longnecker and T. S. Jardetzky (2010). "Crystal structure of the Epstein-Barr virus (EBV) glycoprotein H/glycoprotein L (gH/gL) complex." *Proc Natl Acad Sci U S A* **107**(52): 22641-22646.

93. Maurer, U. E., T. Zeev-Ben-Mordehai, A. P. Pandurangan, T. M. Cairns, B. P. Hannah, J. C. Whitbeck, R. J. Eisenberg, G. H. Cohen, M. Topf, J. T. Huiskonen and K. Grunewald (2013). "The structure of herpesvirus fusion glycoprotein B-bilayer complex reveals the protein-membrane and lateral protein-protein interaction." *Structure* **21**(8): 1396-1405.

94. Meents, A., S. Gutmann, A. Wagner and C. Schulze-Briese (2010). "Origin and temperature dependence of radiation damage in biological samples at cryogenic temperatures." *Proceedings of the National Academy of Sciences* **107**(3): 1094.

95. Mercer, J. and A. Helenius (2008). "Vaccinia virus uses macropinocytosis and apoptotic mimicry to enter host cells." *Science* **320**(5875): 531-535.

96. Mindell, J. A. and N. Grigorieff (2003). "Accurate determination of local defocus and specimen tilt in electron microscopy." *J Struct Biol* **142**(3): 334-347.

97. Moser, F., V. Prazak, V. Mordhorst, D. M. Andrade, L. A. Baker, C. Hagen, K. Grunewald and R. Kaufmann (2019). "Cryo-SOFI enabling low-dose super-resolution correlative light and electron cryo-microscopy." *Proc Natl Acad Sci U S A* **116**(11): 4804-4809.

98. Nahmani, M., C. Lanahan, D. DeRosier and G. G. Turrigiano (2017). "High-numerical-aperture cryogenic light microscopy for increased precision of superresolution reconstructions." *Proceedings of the National Academy of Sciences* **114**(15): 3832.

99. Nicastro, D., C. Schwartz, J. Pierson, R. Gaudette, M. E. Porter and J. R. McIntosh (2006). "The molecular architecture of axonemes revealed by cryoelectron tomography." *Science* **313**(5789): 944-948.

100. Nunez, D., C. Antonescu, M. Mettlen, A. Liu, S. L. Schmid, D. Loerke and G. Danuser (2011). "Hotspots organize clathrin-mediated endocytosis by efficient recruitment and retention of nucleating resources." *Traffic* **12**(12): 1868-1878.

101. Oh, M. J., J. Akhtar, P. Desai and D. Shukla (2010). "A role for heparan sulfate in viral surfing." *Biochem Biophys Res Commun* **391**(1): 176-181.

102. Ortiz, J. O., F. Brandt, V. R. F. Matias, L. Sennels, J. Rappsilber, S. H. W. Scheres, M. Eibauer, F. U. Hartl and W. Baumeister (2010). "Structure of hibernating ribosomes studied by cryoelectron tomography in vitro and in situ." *The Journal of Cell Biology* **190**(4): 613.

103. Paladines, O. L., J. T. Reid, A. Bensadoun and B. D. H. Van Niekerk (1964). "Heat of Combustion Values of the Protein and Fat in the Body and Wool of Sheep." *The Journal of Nutrition* **82**(1): 145-149.

104. Patla, I., T. Volberg, N. Elad, V. Hirschfeld-Warneken, C. Grashoff, R. Fässler, J. P. Spatz, B. Geiger and O. Medalia (2010). "Dissecting the molecular architecture of integrin adhesion sites by cryo-electron tomography." *Nature Cell Biology* **12**(9): 909-915.

105. Penczek, P. A. (2010). "Image restoration in cryo-electron microscopy." *Methods Enzymol* **482**: 35-72.

106. Petrenko, V. F. and R. W. Whitworth (2006). "Physics of ice."

107. Pettersen, E. F., T. D. Goddard, C. C. Huang, G. S. Couch, D. M. Greenblatt, E. C. Meng and T. E. Ferrin (2004). "UCSF Chimera--a visualization system for exploratory research and analysis." *J Comput Chem* **25**(13): 1605-1612.

108. Rehman, Z., I. S. Zuhorn and D. Hoekstra (2013). "How cationic lipids transfer nucleic acids into cells and across cellular membranes: recent advances." *J Control Release* **166**(1): 46-56.

109. Riedel, C., D. Vasishtan, C. A. Siebert, C. Whittle, M. J. Lehmann, W. Mothes and K. Grunewald (2017). "Native structure of a retroviral envelope protein and its conformational change upon interaction with the target cell." *J Struct Biol* **197**(2): 172-180.

110. Ryan, K. P., D. H. Purse, S. G. Robinson and J. W. Wood (1987). "The relative efficiency of cryogens used for plunge-cooling biological specimens." *Journal of Microscopy* **145**(Pt 1): 89-96.

111. Sattentau, Q. J. (2010). "Cell-to-Cell Spread of Retroviruses." *Viruses* **2**(6): 1306-1321.

112. Schelhaas, M., H. Ewers, M. L. Rajamaki, P. M. Day, J. T. Schiller and A. Helenius (2008). "Human papillomavirus type 16 entry: retrograde cell surface transport along actin-rich protrusions." *PLoS Pathog* **4**(9): e1000148.

113. Schellenberger, P., R. Kaufmann, C. A. Siebert, C. Hagen, H. Wodrich and K. Grunewald (2014). "High-precision correlative fluorescence and electron cryo microscopy using two independent alignment markers." *Ultramicroscopy* **143**: 41-51.

114. Schneider, C. A., W. S. Rasband and K. W. Eliceiri (2012). "NIH Image to ImageJ: 25 years of image analysis." *Nat Methods* **9**(7): 671-675.

115. Schur, F. K., M. Obr, W. J. Hagen, W. Wan, A. J. Jakobi, J. M. Kirkpatrick, C. Sachse, H. G. Krausslich and J. A. Briggs (2016). "An atomic model of HIV-1 capsid-SP1 reveals structures regulating assembly and maturation." *Science* **353**(6298): 506-508.

116. Seiradake, E., K. Harlos, G. Sutton, A. R. Aricescu and E. Y. Jones (2010). "An extracellular steric seeding mechanism for Eph-ephrin signaling platform assembly." *Nat Struct Mol Biol* **17**(4): 398-402.

117. Shaner, N. C., M. Z. Lin, M. R. McKeown, P. A. Steinbach, K. L. Hazelwood, M. W. Davidson and R. Y. Tsien (2008). "Improving the photostability of bright monomeric orange and red fluorescent proteins." *Nat Methods* **5**(6): 545-551.

118. Sherer, N. M., M. J. Lehmann, L. F. Jimenez-Soto, C. Horensavitz, M. Pypaert and W. Mothes (2007). "Retroviruses can establish filopodial bridges for efficient cell-to-cell transmission." *Nat Cell Biol* **9**(3): 310-315.

119. Sherer, N. M., M. J. Lehmann, L. F. Jimenez-Soto, A. Ingmundson, S. M. Horner, G. Cicchetti, P. G. Allen, M. Pypaert, J. M. Cunningham and W. Mothes (2003). "Visualization of retroviral replication in living cells reveals budding into multivesicular bodies." *Traffic* **4**(11): 785-801.

120. Smith, A. E. and A. Helenius (2004). "How viruses enter animal cells." *Science* **304**(5668): 237-242.

121. Suenaga, T., T. Satoh, P. Somboonthum, Y. Kawaguchi, Y. Mori and H. Arase (2010). "Myelin-associated glycoprotein mediates membrane fusion and entry of neurotropic herpesviruses." *Proc Natl Acad Sci U S A* **107**(2): 866-871.

122. Symons, M. C. R. (1982). "Radiation processes in frozen aqueous systems." *Ultramicroscopy* **10**(1): 97-103.

123. Tinevez, J.-Y., N. Perry, J. Schindelin, G. M. Hoopes, G. D. Reynolds, E. Laplantine, S. Y. Bednarek, S. L. Shorte and K. W. Eliceiri (2017). "TrackMate: An open and extensible platform for single-particle tracking." *Methods* **115**: 80-90.

124. Tuijtel, M. W., A. J. Koster, S. Jakobs, F. G. A. Faas and T. H. Sharp (2019). "Correlative cryo super-resolution light and electron microscopy on mammalian cells using fluorescent proteins." *Sci Rep* **9**(1): 1369.

125. Turonova, B., F. K. M. Schur, W. Wan and J. A. G. Briggs (2017). "Efficient 3D-CTF correction for cryo-electron tomography using NovaCTF improves subtomogram averaging resolution to 3.4A." *J Struct Biol* **199**(3): 187-195.

126. Uchil, P. D., R. Pi, K. A. Haugh, M. S. Ladinsky, J. D. Ventura, B. S. Barrett, M. L. Santiago, P. J. Bjorkman, G. Kassiotis, X. Sewald and W. Mothes (2019). "A Protective Role for the Lectin CD169/Siglec-1 against a Pathogenic Murine Retrovirus." *Cell Host Microbe* **25**(1): 87-100 e110.

127. Vallbracht, M., D. Brun, M. Tassinari, M. C. Vaney, G. Pehau-Arnaudet, P. Guardado-Calvo, A. Haouz, B. G. Klupp, T. C. Mettenleiter, F. A. Rey and M. Backovic (2018). "Structure-Function Dissection of Pseudorabies Virus Glycoprotein B Fusion Loops." *J Virol* **92**(1).

128. Vangindertael, J., R. Camacho, W. Sempels, H. Mizuno, P. Dedecker and K. P. F. Janssen (2018). "An introduction to optical super-resolution microscopy for the adventurous biologist." *Methods Appl Fluoresc* **6**(2): 022003.

129. Vilas, J. L., J. Gómez-Blanco, P. Conesa, R. Melero, J. Miguel de la Rosa-Trevín, J. Otón, J. Cuenca, R. Marabini, J. M. Carazo, J. Vargas and C. O. S. Sorzano (2018). "MonoRes: Automatic and Accurate Estimation of Local Resolution for Electron Microscopy Maps." *Structure* **26**(2): 337-344.e334.

130. Walt, S. v. d., S. C. Colbert and G. Varoquaux (2011). "The NumPy Array: A Structure for Efficient Numerical Computation." *Computing in Science & Engineering* **13**(2): 22-30.

131. Watson, J. D. and F. H. C. Crick (1953). "Molecular Structure of Nucleic Acids: A Structure for Deoxyribose Nucleic Acid." *Nature* **171**(4356): 737-738.

132. Weisenburger, S., B. Jing, D. Hanni, L. Reymond, B. Schuler, A. Renn and V. Sandoghdar (2014). "Cryogenic colocalization microscopy for nanometer-distance measurements." *Chemphyschem* **15**(4): 763-770.

133. Weisenburger, S., D. Boening, B. Schomburg, K. Giller, S. Becker, C. Griesinger and V. Sandoghdar (2017). "Cryogenic optical localization provides 3D protein structure data with Angstrom resolution." *Nature Methods* **14**: 141.

134. Wickham, T. J., P. Mathias, D. A. Cheresh and G. R. Nemerow (1993). "Integrins alpha v beta 3 and alpha v beta 5 promote adenovirus internalization but not virus attachment." *Cell* **73**(2): 309-319.

135. Wittekindt, C., B. Fleckenstein, K. Wiesmuller, B. R. Eing and J. E. Kuhn (2000). "Detection of human serum antibodies against type-specifically reactive peptides from the N-terminus of

glycoprotein B of herpes simplex virus type 1 and type 2 by surface plasmon resonance." *J Virol Methods* **87**(1-2): 133-144.

136. Wolff, G., C. Hagen, K. Grunewald and R. Kaufmann (2016). "Towards correlative super-resolution fluorescence and electron cryo-microscopy." *Biol Cell* **108**(9): 245-258.

137. Xu, H., X. Hao, S. Wang, Z. Wang, M. Cai, J. Jiang, Q. Qin, M. Zhang and H. Wang (2015). "Real-time Imaging of Rabies Virus Entry into Living Vero cells." *Sci Rep* **5**: 11753.

138. Zanetti, G., J. A. G. Briggs, K. Grünewald, Q. J. Sattentau and S. D. Fuller (2006). "Cryo-Electron Tomographic Structure of an Immunodeficiency Virus Envelope Complex In Situ." *PLOS Pathogens* **2**(8): e83.

139. Zeev-Ben-Mordehai, T., D. Vasishtan, C. A. Siebert, C. Whittle and K. Grunewald (2014). "Extracellular vesicles: a platform for the structure determination of membrane proteins by Cryo-EM." *Structure* **22**(11): 1687-1692.

140. Zeev-Ben-Mordehai, T., D. Vasishtan, A. Hernandez Duran, B. Vollmer, P. White, A. Prasad Pandurangan, C. A. Siebert, M. Topf and K. Grunewald (2016). "Two distinct trimeric conformations of natively membrane-anchored full-length herpes simplex virus 1 glycoprotein B." *Proc Natl Acad Sci U S A* **113**(15): 4176-4181.

141. Zenz, R., H. Scheuch, P. Martin, C. Frank, R. Eferl, L. Kenner, M. Sibilia and E. F. Wagner (2003). "c-Jun Regulates Eyelid Closure and Skin Tumor Development through EGFR Signaling." *Developmental Cell* **4**(6): 879-889.

Appendix I

Materials and methods from (Moser *et al.*, 2019).

MATERIALS AND METHODS

Sample preparation.

XC cells (provided by Quentin Sattentau, University of Oxford, Oxford, United Kingdom) and COS7 cells were propagated in Gibco DMEM GlutaMAX (Thermo Fisher) with 10% FCS at 37 °C and 5% CO2. To generate stable cell lines expressing Dendra2-Lifeact, XC cells were transfected with pDendra2-Lifeact-7 [pDendra2-Lifeact-7 was a gift from Michael Davidson, Florida State University, Tallahassee, FL (Addgene plasmid 54694)] using X-tremeGENE HP DNA Transfection Reagent (Sigma) and selected with G-418 (Sigma). Cells used for this study tended to avoid growing over holes in the carbon support film of EM grids and instead, clustered to the metal bars; only a small number of cells could be imaged in cryo-EM as a result. To deal with this issue, graphene oxide (GO) sheets were deposited on EM grids to form a continuous surface and a better substrate for cell adhesion using a method based on the work by Bokori-Brown et al. (30). Multilayer GO sheets are fluorescent, but these can be removed by centrifugation, and we did not observe a substantial increase of background fluorescence on GO-coated grids compared with conventional grids. Glow-discharged gold finder grids (Quantifoil) were incubated with GO solution, washed with water, and allowed to dry. However, we found that GO detached from the carbon support during coating with cell adhesion material and subsequent cell culture. To prevent this, GO was cross-linked to the carbon support using 4% paraformaldehyde, washed with water, and coated with 50 mg/mL

fibronectin in PBS. Cells were grown on coated grids for 24 h before plunge freezing. XC cells were transfected with a plasmid containing mClover-TOM20 [Clover-TOMM20-N-10 was a gift from Michael Davidson (Addgene plasmid 56307) (31)] and grown on gold finder grids with single-layer GO on lacey carbon support (EM Resolutions) coated with fibronectin. To obtain COS7 cells with mVenus-marked ER, cells were transfected using Lipofectamine 2000 (Thermo Fisher) with a plasmid (provided by Elena Seiradake, University of Oxford, Oxford, United Kingdom), which consists of the transmembrane helix of the human RPTPmu fused to mVenus. Transfected cells were detached by trypsin and seeded onto carbon-coated grids (Quantifoil), and then, they were grown for 24 h before freezing.

Cryo-SOFI setup and data acquisition.

We modified a commercial cryo-FM system (Cryo CLEM; Leica) equipped with a 50× 0.9-NA objective lens (Cryo CLEM Objective HCX PL APO 50×/0.9; Leica) for cryo-SOFI imaging by coupling lasers (iChrome MLE; Toptica) into the microscope body for fluorophore excitation and photoswitching. Laser light after the single-mode fiber was collimated using an achromatic lens with 19-mm focal length to achieve an illuminated area of ∼40-μm diameter in the object plane. A schematic illustration of additionally required hardware is in SI Appendix, Fig. S1. For all biological examples presented here, data were acquired using 488-nm laser illumination and the standard GFP filter cube of the microscope system (excitation: 470/40; dichroic: 495 low pass; emission: 525/50). Overview images where recorded using a standard CCD camera (DFC365 FX; Leica). Cryo-SOFI data were recorded with an electron multiplying CCD (EMCCD) camera (iXon Ultra

897; Andor) and additional 2× magnification to reach an overall magnification of 100× for matching the larger pixel size of the EMCCD camera. Typical camera settings for cryo-SOFI data acquisition were 50-ms integration time per frame (at a rate of 20 frames per second) for a time series of 2,000 images at an EM gain of 20–200.

Cryo-SOFI drift correction and image reconstruction.

Drift and other mechanical instabilities were determined using an autocorrelation-based approach. Bright structures in the specimen or added fiducial markers were used as reference objects. Whichever signal is used for the drift correction; it is important to have a very high density of fluorescent molecules to prevent errors in the estimation of the drift due to intensity fluctuations. Every image in the data stack was compared with the first one using the findshift routine of the DIPimage toolbox (diplib.org) for MATLAB (Mathworks). Typically, (depending on the pixel size of the raw data) for the SOFI principle, it is important to determine the drift of the sample with subpixel accuracy. The obtained lateral shifts for each image in the raw data stack are then used to correct the drift during data acquisition.

Cryo-SOFI image reconstruction on the drift-corrected data has been performed as described previously for ambient temperature SOFI (17, 18). For cryo-SOFI, where aberrations in the PSF can be more severe, close attention had to be payed to the effects of asymmetries in the PSF on the cross-correlation SOFI images. In comparison with autocorrelation SOFI, which is based on (and restrained to) the actual physical pixels on

the camera, cross-correlation SOFI (XCn) makes use of virtual pixels in between the physical pixels in the raw images:

$$XC_n(\vec{r}_1, \dots, \vec{r}_n, \tau_1, \dots, \tau_n) = \prod_{j<l}^{n} U\left(\frac{\vec{r}_j - \vec{r}_l}{\sqrt{n}}\right) \cdot \sum_{i=1}^{N} U^n\left(\vec{r}_i - \frac{\sum_{k=1}^{n} \vec{r}_k}{\sqrt{n}}\right) \cdot \epsilon_i^n \cdot \omega_i(\tau_1, \dots, \tau_n)$$

[1]

with $\vec{r}$ being the position of the correlated pixels, U being the PSF of the original images, ω being the temporal weighting factor, and τ being the time delays between each pixel (17). The PSF function in Eq. 1 implies that calculated pixel position $\vec{r}$ is at the geometrical center of the correlated pixel. It also shows that each pixel in the SOFI image is dependent on a pixel distance correction factor $U\left(\frac{\vec{r}_j - \vec{r}_l}{\sqrt{n}}\right)$, which corrects for the difference in intensity due to the difference in distance from the correlated pixel (18). This pixel correction factor is very susceptible to optical aberrations in the system. Cross-correlation SOFI images can be calculated in two different ways (20). One uses only different pixels (cross-correlation without repetition). This results in a higher amount of information used to calculate the SOFI pixel value (20), in larger distances between the correlated pixels, and thus, in a higher probability of aberrations affecting the resulting super-resolution image. That happens, because a PSF formed in the presence of optical aberrations has an FWHM isosurface larger than that of an optimal PSF (28). By using different pixels but allowing some of them to be repeated, a cross-correlation with repetition is obtained (20). This minimizes the distance between correlated pixels to minimize the effects of aberrations in the PSF (details and an example are in SI Appendix, Fig. S8). The pixel distance corrections were calculated by comparing a second-order autocorrelation image with an image calculated with a second-order cross-correlation.

The difference between them is the pixel distance correction factor: $U\left(\frac{\vec{r}_1-\vec{r}_2}{2}\right)$, with the positions $\vec{r}$ 1 and $\vec{r}$ 2 of the pixels at either side of the autocorrelated pixel.

The PSF used for the deconvolution was obtained by dividing the SOFI image by one of the according images of one order lower (compare Eq. 1 for order n and n − 1). In this manner, the actual PSF was directly obtained from each experiment. This minimizes artifacts typical for deconvolution due to the application of an inaccurate PSF. For all biological examples shown here, cross-correlation SOFI up to the third or fourth order yielded good super-resolution images. Combined with deconvolution, this resulted in a resolution improvement of approximately two to three times. MATLAB code for cryo-SOFI image reconstruction can be downloaded via the following link: https://github.com/rainerkaufmann/cryoSOFI/releases.

Cryo-EM imaging.

Micrographs were collected on a Tecnai F30 “Polara” (FEI) operating at 300 keV with a postcolumn QUANTUM 964 energy filter (Gatan) operated in Zero-Loss mode using a 20-eV energy slit and K2 Summit direct electron detector (Gatan) operating in counting mode at 2.84-, 4.22-, or 23.1-Å pixel size. A 70-µm C2 aperture was used during all data acquisition. Where possible, tilt series were collected bidirectionally from −55° to 59° at 3° increments with 10 frames per image. Frames were aligned using Unblur (32), and tomograms were reconstructed using IMOD Etomo (33). Tomograms were binned two or eight times and bandpass filtered for visualization using Bsoft (34). Raw tomograms

of images shown in Fig. 1 D–F and J–L and SI Appendix, Figs. S2B and S3 B and C have been deposited as EMD-4471–4473 in the EMDB.

Overlay of cryo-FM and cryo-EM images.

Overlays of cryo-FM (conventional and cryo-SOFI) and cryo-EM images were performed by identifying distinct features visible in both imaging modalities and marking their positions using the Control Point Selection Tool of MATLAB (Mathworks). These positions allowed us to determine the transformation between the different coordinate systems. For the biological samples presented here, sufficient structural similarities between cryo-FM and cryo-EM images could be identified for the correlation. In other cases, fiducial markers visible in cryo-FM and cryo-EM can be used for the determination of the coordinate transformation and overlay of the images (35, 36).

Selected references from publication

17. Dertinger T, Colyer R, Iyer G, Weiss S, Enderlein J (2009) Fast, background-free, 3D super-resolution optical fluctuation imaging (SOFI). Proc Natl Acad Sci USA 106:22287–22292.

18. Dertinger T, Colyer R, Vogel R, Enderlein J, Weiss S (2010) Achieving increased resolution and more pixels with superresolution optical fluctuation imaging (SOFI). Opt Express 18:18875–18885.

20. Geissbuehler S, et al. (2012) Mapping molecular statistics with balanced super-resolution optical fluctuation imaging (bSOFI). Opt Nanoscopy 1:4.

28. Booth M, Andrade D, Burke D, Patton B, Zurauskas M (2015) Aberrations and adaptive optics in super-resolution microscopy. Microscopy (Oxf) 64:251–261.

30. Bokori-Brown M, et al. (2016) Cryo-EM structure of lysenin pore elucidates membrane insertion by an aerolysin family protein. Nat Commun 7:11293.

31. Lam AJ, et al. (2012) Improving FRET dynamic range with bright green and red fluorescent proteins. Nat Methods 9:1005–1012.

32. Grant T, Grigorieff N (2015) Measuring the optimal exposure for single particle cryo-EM using a 2.6 Å reconstruction of rotavirus VP6.

33. Kremer JR, Mastronarde DN, McIntosh JR (1996) Computer visualization of three-dimensional image data using IMOD. J Struct Biol 116:71–76.

34. Heymann JB (2001) Bsoft: Image and molecular processing in electron microscopy. J Struct Biol 133:156–169.

35. Schellenberger P, et al. (2014) High-precision correlative fluorescence and electron cryo microscopy using two independent alignment markers. Ultramicroscopy 143:41–51.

36. Schorb M, Briggs JA (2014) Correlated cryo-fluorescence and cryo-electron microscopy with high spatial precision and improved sensitivity. Ultramicroscopy 143:24–32.